ETH
Eidgenössische Technische Hochschule Zürich
Swiss Federal Institute of Technology Zurich

Lab of Applied Mechanobiology

Engineering nanoporous substrates to fine-tune T cell activation

Master's Thesis

Marius Wenk
Department of Physics

Advisors: Tamara Zünd, Sebastian Lickert, Sira Bielefeldt
Prof. Viola Vogel
Supervisor: Prof. Christopher Hierold

September 8, 2024

Abstract

CAR T cell therapies have revolutionized the treatment of blood cancers, but the conventional manufacturing process remains costly, complex, and time-consuming, often leading to suboptimal cell quality and hindering the therapy's success and accessibility. To address this issue, innovative T cell activation strategies are needed to simplify CAR T cell production while enhancing the quality and efficacy of this living drug. In collaboration with Prof. Dr. Enrico Klotzsch, Prof. Dr. Viola Vogel's laboratory has engineered a nanoporous substrate based on anodized aluminum oxide (AAO), which uniquely induces T cell activation and expansion through physical confinement of cell protrusions within nanopores. However, AAO technology has limitations, including a large and less reproducible pore size distribution, impeding clinical translation. We hypothesize that transitioning to silicon (Si) technology can address these issues and provide more flexibility for optimization. Thus, the first section of this thesis details the development of an optimized protocol for the precise production of silicon nanoholes. We produced 1.5 µm deep pores of diameters down to 150 nm and minimal pore distances of 40 nm. The structures were written with electron beam lithography (EBL) and then transferred into a silicon oxide (SiO_2) mask with reactive ion etching (RIE) before consecutive silicon etching with a Bosch process. This process was successfully established despite the high resolution requirements and aspect ratio of 10:1 (pore depth/diameter). Next, experiments are required to evaluate the effect of silicon nanoholes on T cell activation. Additionally, we explored whether mechanical T cell activation via nanoporous substrates enhances calcium influx potentially independent of the T cell receptor. A novel flow cytometry-based assay was established to assess calcium influx more efficiently than current low-throughput microscopy methods. Results demonstrated a significant increase in calcium influx in T cells seeded on nanoporous substrates compared to classical biochemical stimulation, likely mediated by mechanosensitive calcium channels such as Piezo1. Further research is needed to elucidate the exact role of Piezo1 in detail. Collectively, the established protocols are essential for improving the production and performance of nanoporous substrates and for advancing our understanding of nanopore-induced T cell stimulation, moving this discovery closer to clinical application.

Contents

List of Figures

List of Tables

List of Acronyms

AAO	anodic aluminium oxide
ACT	adoptive T cell transfer or therapy
ALD	atomic layer deposition
AP-1	activator-protein-1
BHF	buffered hydrogen fluoride
BRNC	Binnig and Rohrer Nanotechnology Center
BSA	bovine serum albumin
CAR	chimeric antigen receptor
CaMK	Ca^{2+}/calmodulin-dependent kinase
CCP	capacitively coupled plasma
CD	cluster of differentiation
CPC	contrast value proximity correction
CRS	cytokine release syndrome
DAPI	4',6-Diamidin-2-phenylindol
DMSO	dimethyl sulfoxide
DNase	Deoxyribonuclease
DPBS	Dulbecco's Phosphate Buffered Saline
DRIE	deep reactive ion etching
EB	electron beam
EBL	electron beam lithography
EDTA	Ethylenediaminetetraacetic acid
FACS	fluorescence activated cell sorting
FBS	fetal bovine serum
FDA	Food and Drug Administration
FIB-SEM	focused ion beam scanning electron microscope
GLE	graphics layout engine
HBSS	Hank's Balanced Salt Solution
ICP	inductively coupled plasma
IL-2	Interleukin-2
IPA	isopropyl alcohol
MACS	magnetic activated cell sorting
MacEtch	Metal assisted chemical etching
MEM NEAA	Minimum Essential Medium non-essential amino acids
MFI	median fluorescence intensity
MES	2-(N-morpholino)ethanesulfonic acid
MHC	major histocompatibility complex
NFAT	nuclear factor of activated T cells

NF-kappaB	Nuclear Factor kappaB
PBMCs	peripheral blood mononuclear cells
PBS	phosphate buffered saline
PECVD	plasma-enhanced chemical vapour deposition
Pen/Strep	Penicillin/Streptomycin
PMMA	Polymethylmethacrylat
RF	radio frequency
RIE	reactive ion etching
RPMI	Roswell Park Memorial Institute
ScopeM	Scientific Center for Optical and Electron Microscopy
SEM	scanning electron microscope
TCR	T cell receptor
TCM	T cell medium
TMA	Trimethylaluminium
UV	ultraviolet

1 Introduction

T cells or T lymphocytes are a strand of immune cells that mature in the thymus. They are an important part of the adaptive immune system that carries out antigen-specific immunological functions. By engineering T cells, new functionalities of targeted immune attacks can be unlocked. This has given rise to technologies in the field of adoptive immunotherapy and more specifically adoptive T cell transfer or therapy (ACT). One prominent example is the use of genetically modified T cells in chimeric antigen receptor (CAR) T cell therapy for the treatment of cancer. Since its first report in 1987 [1], several CAR T therapies have already been approved for clinical use by the Food and Drug Administration (FDA) [2].
However, challenges for CAR T therapies still exist. Due to long manufacturing times and adverse effects like cytokine release syndrome (CRS), the overall treatment costs can go above $500,000 [3, 4]. Yet, the drug costs can account for the bulk of overall costs [4] which makes reducing them very desirable. Additionally, CAR T therapies are still relatively ineffective against solid tumors [2].

For those therapies, the genetic modification of T cells takes place *ex vivo* with T cells isolated from the patients blood. Activation of those T cells plays an important role for both the expansion of T cell colonies [5] and the genetic modification itself [6]. Moreover, T cell differentiation also depends on the means of activation [7]. At the same time, the phenotype of T cells used in CAR T therapy might be relevant for the success of the intervention [8, 9]. Therefore, investigating and optimizing innovative approaches for T cell activation can have major clinical benefits for immune and cancer therapies.

One such approach is the activation of T cells on nanoporous substrates. It has recently been shown, that nanoconfinement of T cell microvilli can boost T cell activation in the absence of T cell receptor (TCR) agonists [11, 12]. The cells form membrane protrusions called microvilli that were found to enter into the pores [11]. Still, the exact mechanisms and pathways leading to this mechanically induced activation are poorly understood.
To obtain the above results, T cells were seeded on nanoporous anodic aluminium oxide (AAO) surfaces of varying pore sizes. The activation effectiveness with this method depends on the pore size [11]. However, for AAO pore sizes can deviate by more than 25% from the mean value [13]. This makes exact understanding of T cell activation pore size dependence difficult. Recent experiments within the lab have hinted to an optimal pore size around 260 nm.
Silicon technology has been optimized and used in many fields [14–17]. Writing

pores into silicon or silicon oxide (SiO_2) can therefore enable superior control of pore geometries with already well established technologies. As silicon oxidizes in contact with air, both materials have very similar surface properties.
For the ideal mechanical activation condition, microvilli reached an average length of 1.3 µm before decreasing again [11]. Pores should therefore exceed that length.
Electron beam lithography (EBL) allows to overcome wavelength limitations of optical lithography and to write and develop features of dimensions smaller than hundreds of nanometers into resists[18]. The well established Polymethylmethacrylat (PMMA) resists allow for resolutions below 10 nm [19]. However, they provide poor dry etch resistance compared to newer the more recently developed Chemical Semi-Amplified positive E-beam Resist (CSAR 62) or short CSAR, that also allows for sub 10 nm resolution [20].
Dry etching is the removal of surface layers with plasma, where surfaces are attacked by physical bombardment with plasma particles [21]. This allows for more directional or anisotropic etching compared to wet etching. Several variations for dry etching exist. For RIE, ions present in the plasma result in additional chemical etching that greatly enhance etching performance [22]. Inductively coupled plasma (ICP), where radio frequency (RF) power is inductively coupled to the plasma through an antenna [21], can result in plasma densities of one two orders of magnitude higher compared to capacitively coupled plasma (CCP) [22]. RIE and ICP are combined in deep reactive ion etching (DRIE) [22]. Additionally, etch steps can be executed in iteration with side-wall passivation steps to reach higher aspect ratios. In the Bosch process, side-wall passivation with C_4F_8 is iterated with SF_6 DRIE to enhance etch anisotropy [22, 23].

Seeding T cells on more precisely defined pores can not only enable maximisation of activation, but help fundamentally understand the underlying mechanism itself.
Some hints on the activation mechanism exist and recent discoveries hint to a potential role of Piezo1 in the activation process, as treatment with Piezo1 inhibitor GsMTx4 showed reduced activation for T cells seeded on porous substrates (Fig. S1). Piezo1 is a mechanosensitive ion channel that opens and closes in response to mechanical stimuli on the cell membrane [24]. It has been shown to be involved in the regulation of human T cell activation [25]. Conformational changes of Piezo1 mediate extracellular Ca^{2+} ion influx into the cell [26]. Calcium on the other hand influences T cell metabolism, proliferation, differentiation, antibody and cytokine secretion and cytotoxicity [27]. It regulates cytoskeletal remodeling and vice versa [28] and plays a role in dephosphorylation of nuclear factor of activated T cells (NFAT) and activation of Ca^{2+}/calmodulin-dependent kinase (CaMK), that mediates T cell activation [29]. Dephosphorylated NFAT transloctes to the nucleaus and can form transcriptional complexes there [29]. NFAT however can also activate genes responsible for T cell anergy [29, 30]. It therefore has to be balanced with other activation factors, like activator-protein-1 (AP-1) and Nuclear Factor kappaB (NF-kappaB) [29]. The co-existence of all three of those activation factors then leads to the secretion of the cytokine Interleukin-2 (IL-2), that promotes T cell proliferation and differentiation into effector cells [31]. Another marker of T cell activation is the surface-bound cluster of

differentiation (CD)69 that regulates T cell differentiation and cytokine secretion [32]. The standard pathway down to this activation is via TCR signaling. The antigen-recognizing molecules of T cells are TCRs [31], that interact with major histocompatibility complex (MHC)-antigenic peptide complexes on antigen presenting cells (APCs) [29]. Most human T cells are $\alpha\beta$ T cells with α and *beta* TCR chains [33]. These TCR chains together with CD3 form TCR/CD3 complexes. Thereby, binding to CD3 of anti-CD3 can induce TCR downstream signaling [34]. However, co-stimulation of surface-bound CD28 is needed to promote full T cell activation [29, 35]. This is due to the tight regulation of the essential NF-kappaB, via co-stimulatory pathways [29, 36, 37]. Therefore, treatment with anti-CD3 and anti-CD28 can be used as a path to T cell activation, where anti-CD3 is the TCR agonist. Going back to calcium signaling, it was shown, that combined TCR and CD28 stimulation delayed calcium signal decay [35].
Given the role of calcium in T cell signaling, investigating and comparing the change in calcium levels for mechanically and chemically activated T cells could yield valuable insights into signaling pathways and sensor mechanisms involved in pore-stimulated T cell activation.

Beyond three dimensional surface structure, cell binding to the substrate surface is governed by the hydrophilic nature of the cell exterior. Plasma treatment of surfaces can make substrates more hydrophilic. Hence, surface fictionalization prior to cell seeding becomes relevant.

Aims and Own Approach

The aim of this thesis is to investigate and optimize T cell activation through pore-induced mechanical stimuli. To achieve this overarching goal, three specific aims are defined:

1. Fabrication of Nanopore Arrays in Silicon or Silicon Oxide

The first objective was to produce nanopore arrays in either silicon or silicon oxide (SiO_2). EBL is employed for the precise writing and design of the initial pore structures. These structures were then transferred into silicon or silicon oxide via dry etching, utilizing additional hard mask layers. Based on prior studies showing optimal T cell activation on AAO substrates with pore diameters of several hundreds of nanometers [11], pore diameters of 150 nm, 300 nm, and 450 nm were selected for fabrication. The smallest pore distance tested was 25 nm, to explore the lower limits of pore spacing that can induce T cell activation. Higher distance pores, up to 500 nm, were to be produced to test the boundaries of T cell activation through pore-induced mechanical stimuli. To enable full microvilli penetration into the pores, a minimum pore depth of 1.5 µm was targeted, corresponding to an aspect ratio of 1:10 for the smallest pore diameters.

2. Optimization of Surface Conditions to improve T Cell Activation and Substrate Storage

Beyond pore production, the second aim was to optimize chemical surface conditions to enhance T cell activation and produce a modification for long-term storage. This involves investigating different plasma treatment conditions on AAO surfaces, which are already established for T cell activation. A key aspect of this objective is to test the stability of physical plasma modification over several weeks and to optimize the plasma pressure conditions for better T cell activation outcomes. Achieving a stable activation after plasma treatment could significantly aid in the implementation of the process in future applications.

3. Investigation of Calcium Signaling in Pore-Induced T Cell Activation

The third aim was to investigate the role of calcium signaling in pore-induced T cell activation and compare it to T cell activation induced by T cell receptor (TCR) agonists. For this purpose, a high-throughput T cell calcium assay was to be developed. There, T cells are stained with calcium-binding fluorochromes prior to seeding them on substrates for activation. Unlike traditional methods that rely on microscopy to observe intracellular calcium, this approach involves using flow cytometry to analyze cells after they are washed off the substrates. This method is thought to significantly increase the number of cells analyzed, from tens of cells using microscopy to tens of thousands per measurement, providing more robust data for understanding the mechanisms of pore-induced T cell activation.

These three aims collectively seek to advance our understanding of how mechanical stimuli through engineered pores can be optimized to activate T cells and provide valuable insights into the underlying cellular mechanisms.

2 State of the Art

We start by looking into how similar goals have been achieved in the recent past. This provides a good starting point and an overview of what remains to be investigated.

2.1 Microfabrication of Porous Substrates in Silicon and SiO_2

Aspect ratios (horizontal feature size/vertical feature size) are defining for etch processes. For dry etching, gas exchange t relatively deep spaces is reduced and for wet etching complete drying limited by surface tension effects. Aspect ratios achieved for structures in silicon range to 200:1 (pillar height/width) for nano-pillars with 200 nm diameter [38] and 160:1 for 130 nm lines and 120 nm spaces [39]. Those values however were achieved for Metal assisted chemical etching (MacEtch), where structures are transferred into silicon by wet etching.
For dry etching, aspect ratios of 67:1 for 600 nm wide slits and 77:1 for 1 µm wide slits have been achieved with DRIE [40]. Depths of more than 500 µm for holes of 25 µm width have been achieved with the DRIE process [41]. These designs share etch patterns of higher surface area per individual hole, compared to the 150 nm holes aimed to be produced in this thesis. The RIE lag leads to height differences between structures of different surface areas and therefore different aspect ratios. It could be reduced to 1.5% difference between aspect ratios of 2.5:1 and 10:1 [42]. These results were obtained for pillars of 50 µm depth, implying again a comparably big surface area.
Etching of down to 280 nm diameter pores, 7 µm deep into silicon with an optimized 2-step Bosch process has recently been realized [43]. Although, the pore pitch was no lower than 1.9 times the diameter and the pore distribution angle optimized for drilling into silicon crystal [43, 44], this shows general feasibility of etching pores for the work on T cells with DRIE. Alternative to DRIE, small structures of 34 nm width have also been produced with HBr based ICP etching [45].
Etches into SiO_2 are less prominent in literature. However, high aspect ratio optical structures have been produced before at the Binnig and Rohrer Nanotechnology Center (BRNC) where this thesis has been conducted and promising protocols were readily available. Nonetheless, for higher pore diameters of 2 µm, aspect ratios of 100:1 have been achieved with electrochemical wet etching in HF [46].

2.2 Calcium Staining of T Cells

Calcium staining of cells is well established. Calcium stains have been used to study T cell calcium levels with fluorescence microscopy [47]. Plate reader-based and flow

cytometry readouts of cellular calcium levels have also been performed [48, 49]. Yet, challenges for the readout of pore activated T cell calcium levels remain. The T cells for different conditions need to be treated within reduced times, as calcium levels for T cells seeded on pores have been observed to change quickly by our collaborators (Enrico Klotzsch, Humbold-University Berlin).

3 Methods

In this chapter, we continue by explaining the process parameters and protocols used for the experiments. In order to achieve the goals of this thesis, methods from both microfabrication and cell biology were used. We start by describing microfabrication process parameters, as this also reflects the first aim that will be discussed in Chapter 4. The methods used to achieve the aims of this thesis overlap for several aims and are therefore not sorted by aim.

3.1 Wafers and Clean Room Laboratory

Silicon wafers of four inch diameter from Silicon Materials (Kaufering, Germany) doped with 2 Ω to 10 Ω and 525 nm thickness were used as substrates.
Oxide layers were deposited onto those four inch silicon wafers. All but one wafer, that is mentioned explicitly in Section 3.5, were provided together with oxide layers of specified thickness by Ute Drechsler at the BRNC. The BRNC is a clean room research facility operated jointly by IBM and ETH Zürich.
After deposition, the wafers were diced into 20 mm x 20 mm chips.
The lithography and etching steps were executed at the BRNC.

3.2 Pore Images and Image Analysis

In the following, the dimension of the wafer perpendicular to the four inch plane is referred to as z-dimension, while the plane is referred to as x-y plane.
Images of the x-y plane were taken with a SU-8230 (Nano Shield) scanning electron microscope (SEM) by Hitachi, Tokyo, Japan at BRNC. Some additional images were taken with a Zeiss (Oberkochen, Germany) ULTRA 55 plus SEM at FIRST and will be marked in the figure caption. If not mentioned otherwise, images were taken in the center of each patterned field. z profile measurements with focused ion beam scanning electron microscope (FIB-SEM) were taken with Helios 5 and Helios NanoLab 600i DualBeam by Thermo Fisher Scientific, Waltham, USA.

Image analysis was conducted in Fiji (ImageJ). A Fiji macro was programmed to detect the interior of the pores by converting to a binary mask after inverting the image and executing a Gaussian blur with $\sigma = 2$ pixels. The pore diameter d was determined from the recognized pores as $d = 2 \cdot \sqrt{\frac{A}{\pi}}$, where A is the area of the pore. The circularity C was calculated via $C = \frac{4\pi A}{P^2}$ with the perimeter P. Values for the minimal pore distance Δ were determined via subtraction of the pore diameter from

Table 3.1: Methods for the measurement of layer thickness (1-2) and loss of thickness during etching (3)

Index	Measurement method
1	Only for resist: Scratch with tweezer and measure scratch depth.
2	Partially cover remaining layer with Resist (AZ1512, baked at 110 °C for 1 min or CSAR if already applied), then remove uncovered layer part with wet etch, consequently strip resist and measure step height. Wet etch for Al_2O_3: H_3PO_4.
3a	Above layer is resist. Before etching: Remove part of above layer by scratching it. After etching: Measure thickness of above layer with method 1 and step height at scratch and take difference of measured heights as thickness loss.
3b	Above layer is not resist. Before etching: Remove part of above layer analogously to method 2. After etching: Strip above layer and measure step height.

the pattern repetition length l: $\Delta = l - d$. Measurements deviating by more than 60% from the mean area A per image were excluded with Python.

3.3 Layer Thickness Measurements

The layer thicknesses and etch depths after various etch steps were measured with different methods listed in Table 3.1. The measurements were taken with a DektakXT profilometer by Bruker, Billerica, USA. For control measurements of the total depth of the structures written with lithography, markers of 50 µm width were used.

3.4 Resist Patterning and Development

For EBL, a positive CSAR resist was applied as top layer for every test chip via spin coating. Here, AR-P 6200.09 by Allresist (Strausberg, Germany) was used as CSAR resist. Other resists mentioned later in Section 3.5 were tested or used for other purposes, but never exposed to EBL.

Before application of CSAR resist, the chip was cleaned with O_2 plasma at 600 W for 3 min. After that, it was dehydrated for 5 min on the hot plate at 180 °C. The CSAR was spun at either 4000 rpm to achieve an approximate thickness of 200 nm or 2000 rpm for 300 nm. Spin acceleration was 2500 rpm/s for 200 nm CSAR or 2500 rpm/s for 300 nm. Spin duration was 40 s or longer. The resist was baked for 60 s at 150 °C immediately after application. The values for resist thickness will in this chapter be

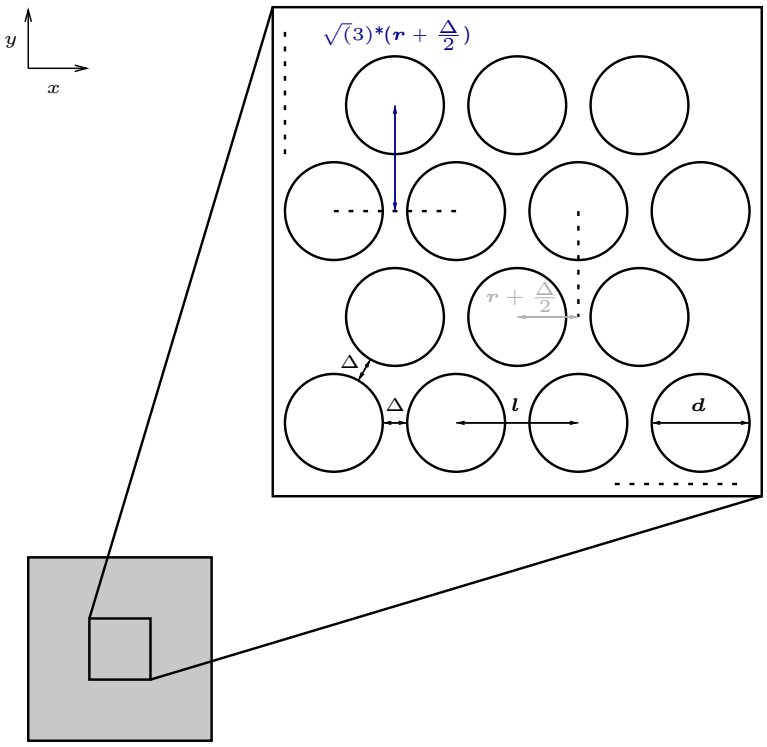

Figure 3.1: Sketch of mask design including relevant lengths

used as an approximation and thickness measurements can be found in Chapter 4.

The masks for EBL were designed with KLayout as GDS files. A hexagonal pore distribution was used. Fig. 3.1 shows the geometry of the mask and the distances used to design the masks. Chip sizes used for the samples to be used for cell seeding are listed in Section 3.7. For the remaining test patterns investigated in this section, pore arrays were patterned onto 200 µm x 200 µm fields spaced apart by 100 µm. If not mentioned differently, mask pore diameters d_M of 150 nm, 300 nm and 450 nm were used in all combinations with mask minimal pore distances of 25 nm, 50 nm and 100 nm.

The electron beam (EB) dosage D for a given developer and the development method were optimized for low levels of resist residues and high mask transfer accuracy. The developers and dosages listed in Table 3.2 were tested. Additionally, for sample C (Table 3.2) different levels of contrast value proximity correction (CPC) were tested. The levels were provided relative to a standard defined by Antonis Olziersky at the BRNC who operated the EBL device. AR 600-546 by Allresist was used.

Table 3.2: Parameters for CSAR development

Sample	Chemical developer	Development time in min	Electron beam (EB) dosage in $\mu C\,cm^{-2}$
A	AR 600-546	1	225 - 265, steps of 5
B	AR 600-546	3	225 - 265, steps of 5
C	Ethyl L-lactate	1	280 - 320, steps of 10

3.5 Etching Pores into SiO_2

A layer stack consisting of SiO_2, Al_2O_3 and CSAR from bottom to top as depicted in Fig. 3.2 was tested as process stack. Different layer thicknesses were used. The Al_2O_3 layer served as a hard mask for pattern transfer. The final structures were written into SiO_2. Therefore, the stacks are referred to as SiO_2 stacks.
For the test of the SiO_2 stack, three diced wafers were used. Table 3.3 shows the layer thicknesses and the SiO_2 deposition methods for those wafers.
Here, wafer 01 was produced by myself at FIRST - Center for Micro- and Nanoscience of ETH Zürich. For the depositions, a Picosun Sunale R-150B atomic layer deposition (ALD) by Applied Materials (Santa Clara, USA) and an Oxford Instruments

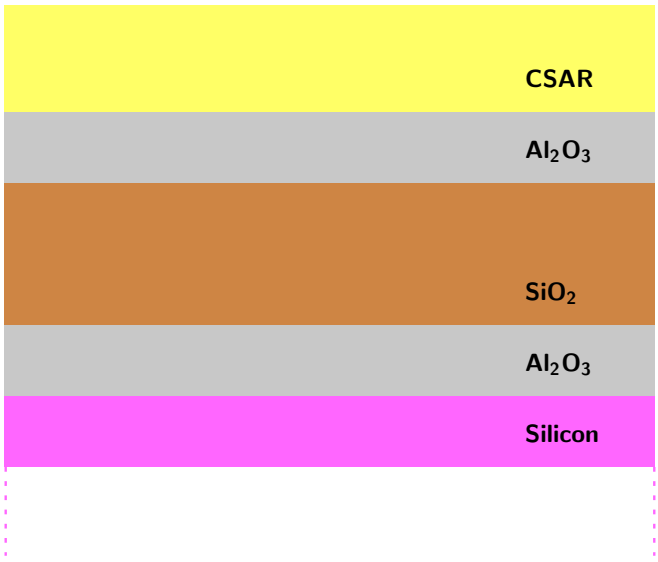

Figure 3.2: Sketch of SiO_2 stack layering

Table 3.3: Layer thicknesses where left to right is from top to bottom for SiO_2 stacks, together with SiO_2 deposition method

Wafer	Al_2O_3 thickness in nm	SiO_2 thickness in nm	Al_2O_3 thickness in nm	CSAR thickness in nm	SiO_2 deposition method
01	30	2000	30	200	PECVD
02	100	2000	45	300	PECVD
03	0	2000	45	300	thermal

PECVD 80+ plasma-enhanced chemical vapour deposition (PECVD) were used. The layer thicknesses were determined via deposition times or number of deposition cycles based on elipsometry measurements of previous users. 30 nm of Al_2O_3 correspond to 250 cycles of Trimethylaluminium (TMA) and H_2O at 180 °C. 2 µm of SiO_2 correspond to 36 min of deposition with SiH_4 and N_2O.
The remaining wafers were provided by Ute Drechsler, as mentioned at the beginning of this section. The Al_2O_3 layers for wafer 02 and 03 (Table 3.3) were deposited at 300 °C. For PECVD deposited layers, a protective ALD layer was used in between silicon and SiO_2, while thermal oxide was produced directly by oxidizing the wafer exterior.

The layers were etched with an ICP in a PlasmaPro System 100 by Oxford Instruments (Abingdon, UK).
The Al_2O_3 layer was etched with a BCl_3/Cl_2 gas mixture of 40 sccm BCl_3 and 8 sccm Cl_2 together with 2 sccm Ar at 120 W RF power, 700 W ICP power and 20 °C. Gas pressure was 6 mTorr.
The SiO_2 was etched with C_4F_8 gas at 40 sccm together with 3 sccm Ar at 85 W RF power, 2400 W ICP power and 10 °C. Gas pressure was 10 mTorr.

The etch rates of these gases for different test layers were measured according to the parameters in Table 3.4. The 219 nm PMMA 600k (AR-P 669.04; Allresist) layer was applied by spinning with 5000 rpm for 60 s with an acceleration of 2500 rpm/s. The resist was baked for 5 min at 180 °C. The Al_2O_3 layers were deposited at 300 °C.

Four versions of etch time patterns were tested. Table 3.5 shows the etch times applied on various wafers from Table 3.3 for different CSAR development methods from Table 3.2.

Table 3.4: Etch times and gases for the etch rate measurements

Process gas	Layer	Etch time in s	Measurement method (Table 3.1)
BCl_3/Cl_2	200-300 nm CSAR	60	1
BCl_3/Cl_2	219 nm PMMA 600k	60	1
BCl_3/Cl_2	45 nm Al_2O_3	60	3a
C_4F_8	100 nm Al_2O_3	420	2
C_4F_8	2000 nm SiO_2	420	3b

Table 3.5: RIE etch times for SiO_2 stacks, together with resist development method and wafer design

Sample	BCl_3/Cl_2 etch time in s	C_4F_8 etch time in s	CSAR development (Table 3.2)	Wafer (Table 3.3)
v1	150	420	A	01
v2	195	420	A	02
v3	195	360	B	02
v4	195	180	B	02, 03

3.6 Etching Pores into Silicon

Another layer stack as sketched in Fig. 3.3 was tested with different process parameters. For this stack, the final structures were etched into Silicon. On top of the 525 µm silicon wafer, a SiO_2 hard mask of variable thickness was used. On top of that a CSAR resist layer of 300 nm thickness was applied.

The SiO_2 layer was etched with a PlasmaPro 80 RIE by Oxford Instruments, with a 12 sccm CHF_3, 38 sccm Ar gas mixture at 75 W RF power and 20 °C. The etch rates for CSAR and SiO_2 were measured after 15 min, 28 min and 36 min.

For the consecutive etching into silicon, two methods were tested. In the first method, silicon was etched with a Oxford Instruments PlasmaPro System 100 ICP process with a HBr, O_2 gas mixture of different mixing ratios, as listed in Table 3.6. Plasma RF power was 80 W, ICP power 800 W and temperature 50 °C. Gas pressure was 2 mTorr for gas

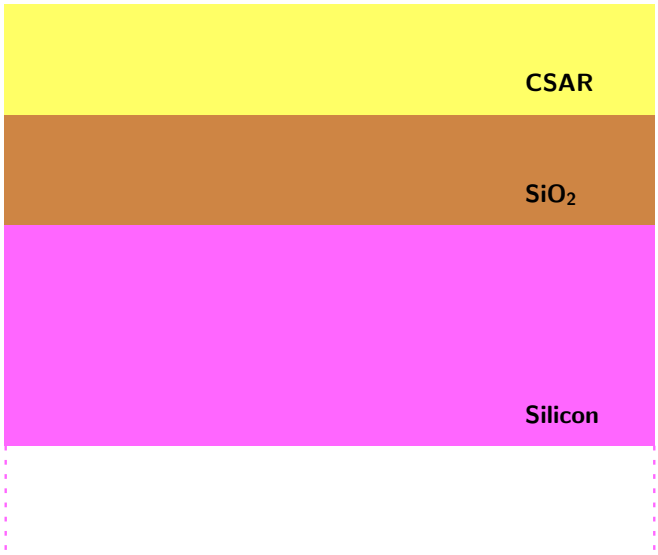

Figure 3.3: Sketch of Silicon stack layering

Table 3.6: Gas pressures for HBr, O_2 gas mixture in ICP etch process

Sample	HBr gas pressure in sccm	O_2 gas pressure in sccm
01	40	0
02	38.5	1.5
03	37	3

mixture 01 and 4 mTorr for gas mixtures 02 and 03. This process will be referred to as ICP etch. For ICP etch processes with gas mixtures 02 and 03, the etch selectivities were determined in a separate experiment with 7 min etch time. Therefore wafers with optical lithography structures in thermal SiO_2 on top were used. The SiO_2 layer was produced and the wafer kindly provided by Ute Drechsler. The etch selectivity for gas mixture 01 was assumed to be 1:3 for SiO_2 to silicon etch, based on measurements of previous tool users. Analogously, the etch rate was estimated as 165 nm min^{-1}.

For the second method, the silicon was etched with a SPTS (Newport, UK) Omega® LPX DRIE Bosch process. The first step was a 200 sccm C_4F_8 passivation including 1 sccm SF_6, followed by a 5 sccm C_4F_8, 200 sccm SF_6, 1 sccm O_2 etch and then a 5 sccm C_4F_8, 200 sccm SF_6, 40 sccm O_2 etch. This process will be referred to as DRIE etch. Both 20 and 25 DRIE cycles were tested. The remaining CSAR resist was removed by bathing the chips in dimethyl sulfoxide (DMSO) at 125 °C for 2 min. After

Table 3.7: Etch times and layer thicknesses for SiO_2 layers of silicon stacks on different chips. Different resist development techniques were also used for the different chips.

Sample	SiO_2 thickness in nm	RIE etch time in min	resist development (methods from Table 3.2)
s1	500	48.5	B, $D = 230\,\mu C/cm^2$
s2	300	28 (ICP); 30 (DRIE)	B, $D = 230\,\mu C/cm^2$
s3	300	30	C, entire dosage range
s4	300	30	C, $D = 280\,\mu C/cm^2$, 80% CPC

this, the chips were cleaned with a 50 sccm O_2 plasma at 100 W RF power and 20 °C for 2 min in the PlasmaPro 80 RIE.

The etch times for processing of chips carrying the wafer stacks were determined based on the thickness of the SiO_2 layer. The corresponding thicknesses and etch times are listed in Table 3.7. For sample s2, an additional 2 min RIE etch was applied before etching with DRIE, compared to etching with HBr based ICP. For sample s4 a special mask with mask pore diameters d_M of 150 nm, 300 nm and 450 nm in all combinations with mask minimal pore distances of 30 nm to 110 nm in steps of 10 nm was used.

3.7 Substrate Production

Porous silicon chips were produced with the tools and processes described in Section 3.6 with 300 nm of thermal SiO_2 and 300 nm of CSAR resist. The resist was written at an EB dosage D of 280 µC/cm^2 and with 80% CPC. The resist was developed for 1 min with Ethyl L-lactate, as described in Section 3.4. The SiO_2 RIE etch time was 30 min and the silicon was etched for 25 cycles with the DRIE process. The chips were diced in between SiO_2 and silicon etch steps, where the pattern was already transferred into the hard mask, but not yet at its final depth. AZ® 1512HS Photoresist (Merck Performance Materials, Southampton, UK; cat. no. 1A001512) was applied as protection by spin coating at 4000 rpm for 40 s with 2000 rpm/s acceleration. The resist was baked at 110 °C for 60 s. After that, the chip was diced by Ute Drechsler. Dicing markers were 50 µm wide and spaced 5200 µm x 5600 µm apart. Additional 20 µm at the borders of every 5200 µm x 5600 µm chip were not structured. After dicing, the AZ® 1512HS resist was removed by bathing every individual chip for 40 s in acetone in ultrasound bath and then in isopropyl alcohol (IPA) for 20 s. Afterwards, the chips were cleaned in an RIE O_2 plasma at 100 W for 2 min.

Mask specifications were selected for a variation of pore diameters over $d_M = 150\,\text{nm}$, $d_M = 300\,\text{nm}$ and $d_M = 450\,\text{nm}$ at constant pore distance $\Delta_M = 50\,\text{nm}$ and for a variation of pore distances over $\Delta_M = 50\,\text{nm}$, $\Delta_M = 200\,\text{nm}$ and $\Delta_M = 500\,\text{nm}$ at constant pore diameter $d_M = 300\,\text{nm}$
The chips were placed into a μ-Slide 18 well plate (ibidi, Gräfelfing, Germany; cat. no. 80826). Two silicon chips that were treated and diced identically to those with pores, but without any structure written into it through EBL, were also placed into the plate as flat reference. Additionally, four porous AAO FlexiPors (SmartMembranes, Halle, Germany; cat. no. F1224004) and four flat Aluminum 99.98% pure (SmartMembranes) samples of 5.2 mm x 5.6 mm size were also cut out and placed into unused wells. Due to time restraints for this thesis, the plate was handed over to Tamara Zünd for future CD69 readouts.

3.8 Pan T Cell Isolation

Human naive pan T cells or human pan T cells from healthy donors were used. The use of peripheral blood mononuclear cells (PBMCs) was approved by Kantonale Ethikkommission Zurich (KEKZH-Nr.2012-0111) and the Buffy Coats were obtained from Blutspende SRK Zurich.
The PBMCs were isolated from 50 mL buffy coat, diluted in 160 mL phosphate buffered saline (PBS). The dilution was distributed onto six SepMate™-50 columns (cat. no. 85450) pre-filled with 15 mL density gradient solution Lymphoprep™ (cat. no. 07851) both by STEMCELLS Technologies (Vancouver, Canada). The columns were centrifuged at 1200 g for 10 min. The top layer containing the PBMCs was poured into a 50 mL tube (Sarstedt, Nümbrecht, Germany; cat. no. 62.547.254). The PBMCs were obtained as a pellet after centrifuging at 120 g for 15 min without break and consequently removing the supernatant. The PBMCs were washed by re-suspending in 50 mL PBS and centrifuging again with the same settings. After counting, the cells were centrifuged and washed again with 300 g for 8 min. The pellet was re-suspended in fetal bovine serum (FBS) at 100×10^6 cells/mL concentration.
The PBMCs were frozen after adding freezing medium at equal volume. The freezing medium was prepared as a mixture of 20% DMSO (cat. no D5879) by Sigma-Aldrich and 80% FBS. The cells were frozen at $-80\,^\circ\text{C}$, while placed inside Mr. Frosty™ Freezing Container (Thermo Fisher Scientific, cat. no. 5100-0001).

At the day of the experiment or up to two days in advance, the PBMCs were thawed, added to 250 µL of $1\,\text{mg}\,\text{mL}^{-1}$ Deoxyribonuclease (DNase) (Sigma-Aldrich; cat. no. DN25) in Dulbecco's Phosphate Buffered Saline (DPBS) (Gibco™; cat. no. 14190144) and quickly centrifuged at 500 g for 5 min in order to wash of the freezing medium. The cells were re-suspended in pre-warmed T cell medium (TCM) (Section 3.8.1) at 37 °C. Another 200 µL DNase were added to the suspension, the cells were counted and then centrifuged at 350 g for 10 min.
For the pan T cell isolation, slightly different protocols were used for naive pan T

cells and pan T cells. Per 10×10^6 cells, the PBMCs were re-suspended in 30 µL magnetic activated cell sorting (MACS) buffer (Section 3.8.2) for N cells or 40 µL for P cells respectively. For N cells, 10 µL of Biotin-Antibody Cocktail and 10 µL of anti-TCRγ/δ-Biotin-Antibody Cocktail both from the human Naive Pan T Cell Isolation Kit (Miltenyi Biotec, Bergisch Gladbach, Germany; cat. no. 130-097-095) were added per 10×10^6 cells. For P cells, 10 µL of Biotin-Antibody Cocktail from the human Pan T Cell Isolation Kit (Miltenyi Biotec; cat. no. 130-096-535) were added per 10×10^6 cells. The respective cell suspensions were mixed and incubated at 4 °C for 5 min. Another 30 µL of MACS buffer and 20 µL of (Naive) Pan T Cell MicroBead Cocktail of the respective isolation kit were added per 10×10^6 cells. After mixing everything was incubated for 10 min at 4 °C.
The suspension was separated with LS Columns (cat. no. 130- 042-401) placed in MACS® MultiStand (cat. no. 130-042-303) both by Miltenyi Biotec. The colums were rinsed three times with 1 mL of MACS buffer. The cell suspension was inserted into the LS columns and the flow-through containing the unlabeled (naive) pan T cells was collected. The tube was washed and the columns rinsed with another 3 mL of MACS buffer. The collected cells were counted and centrifuged at 350 g for 10 min. The cells were re-suspended in TCM and cultured at 10^6 cells/mL in the incubator at 5% CO_2 and 37 °C.

3.8.1 T Cell Culture Medium

For the culturing of primary T cells, Roswell Park Memorial Institute (RPMI) 1640 medium + GlutaMAX™ (Gibco™ by Thermo Fisher Scientific, Waltham, USA; cat no. 61870036) was used. The medium was supplemented with 10% FBS (Biowest, Nuaillé, France; cat. no. S1480). Additional Gibco™ supplements were added: 20 mM HEPES Buffer Solution (cat. no. 15630-056), 1% Penicillin/Streptomycin (Pen/Strep) (cat. no. 15140-122), Minimum Essential Medium non-essential amino acids (MEM NEAA) (cat. no. 11140-035), 1 mM Sodium Pyruvate (cat. no. 11360-039), 50 µM 2-Mercaptoethanol (cat. no. 31350-010) and 2 mM L-glutamine (cat. no. 11539876). This medium is in the following referred to as TCM.

3.8.2 MACS/FACS Buffer

The same buffer was used for MACS and fluorescence activated cell sorting (FACS). It was obtained by supplementing Gibco™ PBS, pH 7.4 (cat. no. 10010-015), with 0.5% bovine serum albumin (BSA) (cat. no. A4503-50G) and 2 mM Ethylenediaminetetraacetic acid (EDTA) (cat. no. EDS-100G) both by Sigma-Aldrich.

3.9 Substrate Preparation and Coating

Coating and calcium experiments were conducted with AAO FlexiPors (SmartMembranes; cat. no. F1224004) as porous (P) substrates and Aluminum 99.98% pure (SmartMembranes) as flat (F) substrates. Pore diameter provided by

the manufacturer was 0.26 µm and pore length 5-10 µm. For some experiments pores of 0.13 µm diameter labelled as small and 0.35 µm diameter labelled as big were used. Surface SEM images of AAO are shown in Fig. S2.
Substrates were placed into 48 well cell culture plates (Sigma-Aldrich; cat. no. 677 180).
For experiments with 24 h incubation time or more, the substrates were washed one day in advance. Therefore, de-ionized H_2O containing 0.1% TWEEN® 20 (cat. no. P1379) was added onto the substrates. The plate was shaken at roughly 100 rpm for 15 min. After removal of the H_2O, 70% Ethanol (cat. no. 1.00983) was added onto the substrates and shaken for 15 min. The substrates were then washed with 100% IPA (cat. no. 67-63-0) and incubated on the shaker for another 15 min after applying 100% IPA. After this final washing step, the IPA was removed and the plate dried overnight. The items listed above were produced by Sigma-Aldrich.

In the following, the default parameters for the substrate coating are described.
Before coating, the entire plate was cleaned in a HPT-200 plasma treatment system by Henniker Plasma (Runcorn, UK) with an air plasma at plasma settings of 4 sccm flow, 100% power and 5 min plasma treatment time. For the uncoated substrates, which here specifies those without antibody coating, PBS was added into the wells to reduce air exposure after the plasma cleaning. For coating, 2-(N-morpholino)ethanesulfonic acid (MES) buffer was added to the wells, to cool down the substrates after the plasma cleaning. A MES buffer consisting of 25 mM MES and 0.05% TWEEN® 20 in H_2O at pH 5 was used. After removal of the MES buffer, 10 µg mL^{-1} NeutrAvidin™ Biotin-binding Protein (Thermo Fisher Scientific; cat. no. 31000) in MES buffer was added. The plate was shaken at 100 rpm for 30 min and then the substrates for coating were washed twice with PBS. Antibodies were added in solution with PBS at 5 µg mL^{-1} and the plate again shaken at 100 rpm for 30 min. The antibodies used were Biotin anti-human CD28 (CD28.2) (cat. no. 302904) and Biotin anti-human CD3 (OKT3) (cat. no. 317320) both by BioLegend (San Diego, USA). The coating with these antibodies will be abbreviated as aCD28 and aCD3 or antiCD28 and antiCD3 respectively. After antibody application, the substrates were again washed twice with PBS.
A naive treatment condition referring to cells seeded in an empty well without substrate was used as negative control. Flat+aCD3+aCD28 was used as positive control for T cell activation. For the experiments with 24 h incubation time or more, the plate was sterilized with ultraviolet (UV) light for 20 min immediately before seeding cells onto it. For experiments with cells in Hank's Balanced Salt Solution (HBSS), the substrates and the wells for naive conditions were washed once with TCM and then with HBSS before seeding.

For the substrate coating optimization some of the parameters described in the above paragraph were varied and the resulting IL-2 secretions after 24 h measured. The parameters for Optimization 01 and 02 are listed in Table 3.8 and Table 3.9 respectively. Duplicates were measured for every condition. For the vacuum conditions, the plates were vacuumed with Allpax (Papenburg, Germany) Vakuummaschine P355 immediately

Table 3.8: Substrate coating parameters varied for measurements of IL-2 secretion, as Optimization 01

Substrate	Coating	Derivation from default
Flat	aCD3+aCD28	None
Porous	aCD28	None
Porous, big	aCD28	None
Porous, small	aCD28	None
Porous	Uncoated (-)	None
Naive	Uncoated (-)	None
Porous	aCD28	Vacuum for 21 days
Porous	Uncoated (-)	Vacuum for 21 days
Porous	aCD28	Plasma at 2 sccm
Porous	aCD28	Plasma at 10 sccm

after plasma treatment. The respective number of days later, the vacuumed bags were cut open immediately before coating.

3.10 IL-2 Secretion Assay

For the IL-2 readout, the cells were washed off the substrates by pipetting up and down multiple times. They were transferred into white Nunc™ MicroWell™ 96-Well Microplates (Thermo Fisher Scientific; cat. no. 136101). A Lumit® IL-2 (Human)

Table 3.9: Substrate coating parameters varied for measurements of IL-2 secretion, as Optimization 02

Substrate	Coating	Derivation from default
Flat	aCD3	None
Flat	aCD28	None
Flat	aCD3+aCD28	None
Porous	aCD28	None
Porous, big	aCD28	None
Porous, small	aCD28	None
Porous	Uncoated (-)	None
Naive	Uncoated (-)	None
Porous	aCD28	Vacuum for 44 days
Porous	Uncoated (-)	Vacuum for 44 days

Immunoassay (Promega, Madison, USA; cat. no. W6020) was used for the fluorescent readout. The cell suspensions were diluted with four units of TCM at one unit of cell suspension, creating a 1:5 dilution. A standard series was prepared by serially diluting the Human IL-2 Standard supplied with the Immunoassay at $10\,\mu g\,mL^{-1}$ in TCM. Eight concentrations of IL-2 Standard were used: $50\,000\,pg\,mL^{-1}$, $25\,000\,pg\,mL^{-1}$, $8065\,pg\,mL^{-1}$, $2601\,pg\,mL^{-1}$, $839\,pg\,mL^{-1}$, $271\,pg\,mL^{-1}$, $87.3\,pg\,mL^{-1}$ and $0\,pg\,mL^{-1}$. Standard solutions were added to the plate at volumes equal to those of the samples and in the following treated identical to the samples. An antibody solution with 1:75 dilution of Anti hIL-2 mAB SmBiT and Anti hIL-2 mAB LgBiT supplied with the Immunoassay kit was prepared and added to the samples. The antibodies were diluted in TCM and for 60 µL sample volumes, 15 µL antibody solution was used per well. After adding the antibodies, the plate was shaken at 100 rpm for 1 min and then incubated at 37 °C for 45 min. After that, the samples were incubated at room temperature for another 15 min. A detection solution of 18.75 µL per well was prepared by diluting Lumit® Detection Buffer B supplied with the Immunoassay kit at ratio 1:25 in TCM. The detection solution was added to the wells and the luminescence was measured with a Spark® Multimode Microplate Reader by Tecan (Männedorf, Switzerland).

3.11 Calcium Staining

In order to read calcium levels inside (naive) pan T cells with flow cytometry, a protocol was established. In the following, a default protocol is described. In the process of protocol establishment, several of its steps were varied and executed differently throughout multiple experiments. The modifications are listed one paragraph later.

For the calcium readout at different cell activation conditions, pre-thawed cells were washed after centrifuging at 350 g for 5 min and re-suspended in HBSS at a concentration of 2×10^6 cells/mL. At this concentration, cells were loaded with 4 µM Fluo-8 (AM) (Focus Biomolecules, Plymouth, USA; cat. no. 10-1322) and incubated at 37 °C for 60 min. After centrifuging at 350 g for 5 min and washing again, the loaded cells were re-suspended in HBSS, calcium, magnesium, no phenol red (Gibco™; cat. no. 14025050)and let rest for another 30 min at 37 °C. GsMTx4 (20 µM; MedChemExpress, Monmouth Junction, USA; cat. no. HY-P1410-5MG) for Piezo1 inhibition and EDTA (1 mM; Sigma-Aldrich; cat. no. EDS-100G) for calcium capture, were added at the beginning of this resting period immediately after splitting the cell suspension. Yoda1 (20 µM; MedChemExpress; cat. no. HY-18723) as Piezo1 agonist and the Calcium Ionophore A23187 (10 µM; Sigma-Aldrich; cat. no. C7522), that generically produces ion transport through the cellular membrane, were added at the end of the resting period. Yoda1 aliquots in Ethanol at 10 mM were used. After resting, the cells were seeded onto the substrates or otherwise also added into empty wells of the 48 well plates (Sigma-Aldrich; cat. no. 677 180). The plate was centrifuged at 50 g for 1 min to that cells land onto the substrates and then incubated at 37 °C for the specified activation time. A default activation time of 10 min was used. After that, the cells

were washed off of the samples by pipetting up and down several times and then added into Falcon® 5 mL Round Bottom Polystyrene Test Tubes (Corning, Glendale, USA; cat. no. 352054) , referred to as FACS tubes. The FACS tubes were pre-filled with 3 µM 4',6-Diamidin-2-phenylindol (DAPI) (Sigma-Aldrich; cat. no. D9564) in FACS buffer, such that the final ratio of cell suspension to buffer was 2:1. The tubes were measured one by one with a FACSymphony™ A1 Cell Analyzer (BD Biosciences, San Jose, USA). In some cases the same tubes were measured again after resting at room temperature for a certain time.

For the establishment of the protocol, the following variations were tested: (1) A time curve of the loading time (corresponding to 60 min in the default protocol) was measured with times 0 min, 15 min, 30 min, 45 min, 60 min and 160 min. (2) Throughout the 60 min loading and 30 min resting steps, all combinations of HBSS and TCM were tested as buffer. This is HBSS-HBSS as in the default protocol, but also HBSS-TCM and TCM-HBSS. (3) Fluo-4, AM (Thermo Fisher Scientific; cat. no. F14201) was used instead of Fluo-8. (4) In the resting step, part of the cell suspension was let rest on ice for the duration of experiments with the other part and only then rested in the incubator for 10 min or 30 min. (5) An additional fixation step was tested, where the cells suspension was centrifuged at 500 g for 5 min and washed after the resting step and then re-suspended at 10^6 cells/mL in ROTI® Histofix 4% (Carl Roth, Karlsruhe, Germany; cat. no. P087.6). The cells were left in ROTI Histofix for 10 min at room temperature and then washed out after centrifuging for 5 min at 500 g and re-suspended at 10^6 cells/mL in TCM. (6) The dilution of the cell suspension in FACS buffer was varied and also tested for a 1:3, 2:5 and 2:3 ratio of cell suspension to buffer.

Both Fluo-8 and Fluo-4 were measured with the BD Horizon Brilliant™ Blue 515 (BB515) channel and DAPI was measured with the BD Horizon Brilliant™ Violet 421 (BV421) channel of the flow cytometer. Cell populations were gated into single, live lymphocytes as shown for one exemplary naive cell sample in Fig. S3 and for an Ionophore treated sample in Fig. S4 for the same donor and experiment. The calcium positive cell gate in Fig. S3 and Fig. S4 was set at the 1% highest intensity population threshold for naive cells of every experiment. Fig. S5 shows the resulting gating for two exemplary porous samples for the same donor and experiment. The median fluorescence intensity (MFI) was normalized over the MFI of the corresponding naive condition and Calcium positive gated population percentage was taken relative to live gated single lymphocytes.

3.12 Plotting and Graphics

Plots were created with R or Python, Matplotlib. If not mentioned otherwise, the default was plotting with R. Graphics were generated with graphics layout engine (GLE). Compilations of several images, including scale bars were also created with GLE. Tables were created and this work formatted in LaTeX .

4 Results and Discussion

After establishing methods to realize the experimental on the various aims, we now look into the results. We will look into the results for the three aims separately over the following sections and at the end of each section discuss what the results mean.

4.1 Production of Porous Substrates

Perhaps the main goal of this thesis was to establish a process for writing pores in the regime of several hundred nanometers of diameter into silicon or silicon oxide by dry etching. Silicon and silicon oxide etch quite differently, so different layer stacks have been designed (Figs. 3.2 and 3.3). The etch results for these stacks will be shown in Section 4.1.2 and Section 4.1.3, but in order to etch small structures, one first has to pattern a mask.

4.1.1 CSAR Resist Development

To develop a mask with high resolution and appropriate thickness, several resist development methods were compared. CSAR resist was chosen because of its comparably high resolution and dry etch resistance. Resist thicknesses were found to be on average 224 nm for spinning at 4000 rpm and 288 nm at 2000 rpm.

In the first approach, the development was done according to sample A from Table 3.2 with the official developer AR 600-546 of the manufacturer and 1 min development time. Profilometer measurements showed irregularities in the z-profile of the 50 µm wide markers. Further investigations of AR 600-546 development were therefore made with a higher development time of 3 min as specified in sample B (Table 3.2), where these irregularities were less present.

To get a more detailed picture of resist development, SEM images were taken. In Fig. 4.1 a direct comparison of an image at the default imaging position close to the pattern center with an image at the pattern edge is presented. Due to EB dispersion, the patterns in between other writing surfaces can receive more indirect dosage. Indeed, the patterns looked different at the two different positions over the sample. One can see less dark spots within the pores and irregularities at their boundaries towards the pattern edge compared to the pattern center. Those irregularities are resist residues and are a sign of imperfect resist development and exposure conditions.
In order to optimize for few resist residues at developed sites, the EB dosage was varied, as energy deposition plays a major role in the modification of resist chemistry. The

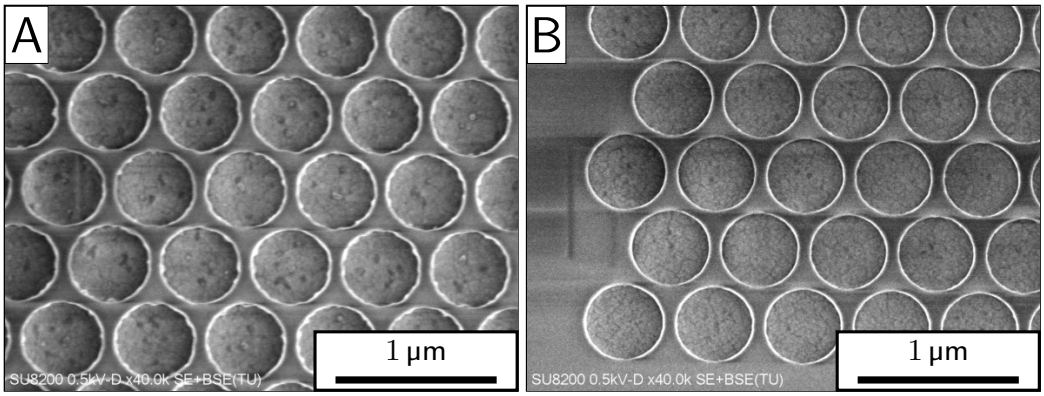

Figure 4.1: SEM images of CSAR resist on sample v3 (Table 3.5) after exposure to 255 µC/cm^2 EB dosage and development with AR-600 546 for 3 min. All sub-figures show images of fields with pore diameter $d_M = 450$ nm and minimal pore distance $\Delta_M = 100$ nm according to the mask. Images are taken in the pattern center (**A**) or at the pattern edge (**B**) respectively.

exposed parts then became extractable for the developer. Fig. 4.2 shows the resist for sample B (Table 3.2) after development for different mask parameters and EB dosages. The dosage scan revealed no major differences in development quality in terms of resist residues. However, for $D = 250\,\mu C/cm^2$ and $D = 265\,\mu C/cm^2$ some pore walls are broken or incomplete, leading to the fusion of several pores into one. Therefore, a dosage of $D = 230\,\mu C/cm^2$ is chosen for further investigations, where those defects are not present.
After optimizing for dosage and development time, it was checked whether the development worked equally well for different pore diameters and distances. Fig. 4.3 and Fig. 4.4 show different pore diameters at constant $\Delta_M = 25$ nm and different minimal pore distances at constant $d_M = 450$ nm respectively. Although not residue free, the development showed no major development errors across the spectrum.

To check, if development was matching the mask designs, more detailed analysis of pore sizes and circularities as introduced in Section 3.2 was conducted. The results are presented in Table 4.1. The mask pattern length l_M was used for the calculations. The pores for $D = 265\,\mu C/cm^2$, $d_M = 150$ nm and $\Delta_M = 25$ nm were to irregular to be analyzed with the given image analysis method. The two entries for $D = 255\,\mu C/cm^2$, $d_M = 450$ nm and $\Delta_M = 100$ nm represent according to their order in the table, the values at the center of the pattern and the pattern edge (Fig. 4.1). For $D = 230\,\mu C/cm^2$ an average difference $d_M - d$ of 31.2 nm results from this analysis.
To understand, why this difference might be as big as 20% for some samples, we look at some images showing the detected pores. Fig. 4.5 shows SEM images for mask

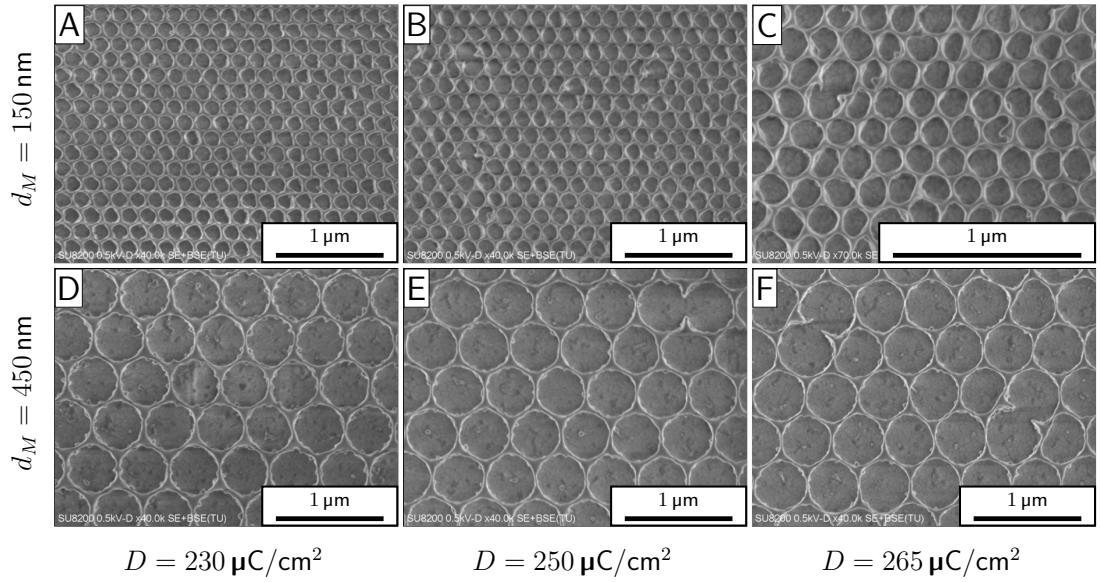

Figure 4.2: SEM images of CSAR resist on sample v3 (Table 3.5) after development with AR-600 546 for 3 min. All sub-figures show images of fields with minimal pore distance $\Delta_M = 25\,\mathrm{nm}$ according to the mask. Sub-figures show different EB dosages D and mask pore diameters d_M. **A**: $d_M = 150\,\mathrm{nm}$, $D = 230\,\mu\mathrm{C/cm^2}$; **B**: $d_M = 150\,\mathrm{nm}$, $D = 250\,\mu\mathrm{C/cm^2}$; **C**: $d_M = 150\,\mathrm{nm}$, $D = 265\,\mu\mathrm{C/cm^2}$; **D**: $d_M = 450\,\mathrm{nm}$, $D = 230\,\mu\mathrm{C/cm^2}$; **E**: $d_M = 450\,\mathrm{nm}$, $D = 250\,\mu\mathrm{C/cm^2}$; **F**: $d_M = 450\,\mathrm{nm}$, $D = 265\,\mu\mathrm{C/cm^2}$

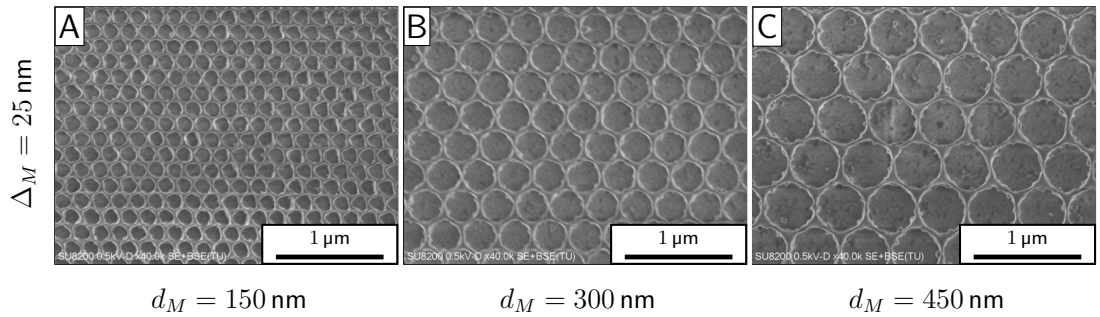

Figure 4.3: SEM images of CSAR resist on sample v3 (Table 3.5) after exposure to $230\,\mu\mathrm{C/cm^2}$ EB dosage and development with AR-600 546 for 3 min. All sub-figures show images of fields with minimal pore distance $\Delta_M = 25\,\mathrm{nm}$ according to the mask. Sub-figures show different mask pore diameters d_M. **A**: $d_M = 150\,\mathrm{nm}$; **B**: $d_M = 300\,\mathrm{nm}$; **C**: $d_M = 450\,\mathrm{nm}$

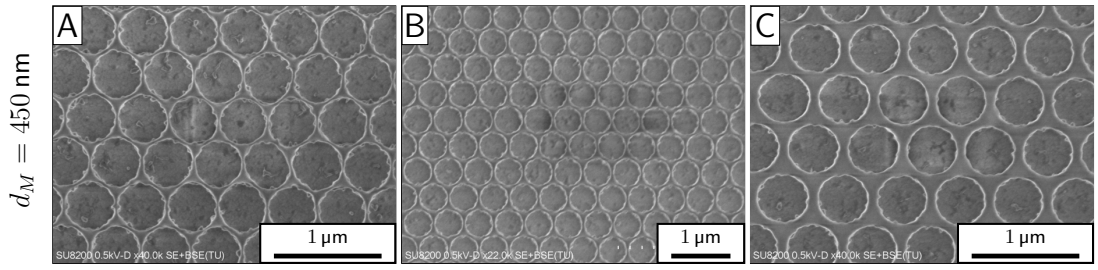

Figure 4.4: SEM images of CSAR resist on sample v3 (Table 3.5) after exposure to 230 µC/cm^2 EB dosage and development with AR-600 546 for 3 min. All sub-figures show images of fields with pore diameter $d_M = 450\,\mathrm{nm}$ according to the mask. Sub-figures show different mask pore distances Δ_M. **A**: $\Delta_M = 25\,\mathrm{nm}$; **B**: $\Delta_M = 50\,\mathrm{nm}$; **C**: $\Delta_M = 100\,\mathrm{nm}$

Table 4.1: Pore diameters (PD) and minimal pore distances (MD) for different mask layouts and EB dosages for development B (Table 3.2). Differences from the ideal value $d_M - d$ and circularities of the pores are also listed. The values are obtained from SEM images in Figs. 4.1 to 4.4 and S6.

Mask PD d_M in nm	Mask MD Δ_M in nm	EB dosage D in µC/cm^2	PD d in nm	MD Δ in nm	Difference $d_M - d$ in nm	Circularity C
150	25	230	112.8	62.2	37.2	0.68
150	25	250	127.9	47.1	22.1	0.71
300	25	230	268.7	56.3	31.3	0.54
450	25	230	413.0	62.0	37.0	0.66
450	25	250	426.2	48.8	23.8	0.69
450	25	265	421.6	53.4	28.4	0.70
450	50	230	425.1	74.9	24.9	0.88
450	100	225	427.7	122.3	22.3	0.73
450	100	230	424.3	125.7	25.8	0.76
450	100	240	442.0	108.0	8.0	0.83
450	100	245	441.3	108.7	8.7	0.81
450	100	250	430.9	119.1	19.1	0.79
450	100	255	441.4	108.6	8.6	0.81
450	100	255	446.0	104.0	4.0	0.73
450	100	260	442.7	107.3	7.3	0.77
450	100	265	438.4	111.6	11.6	0.69

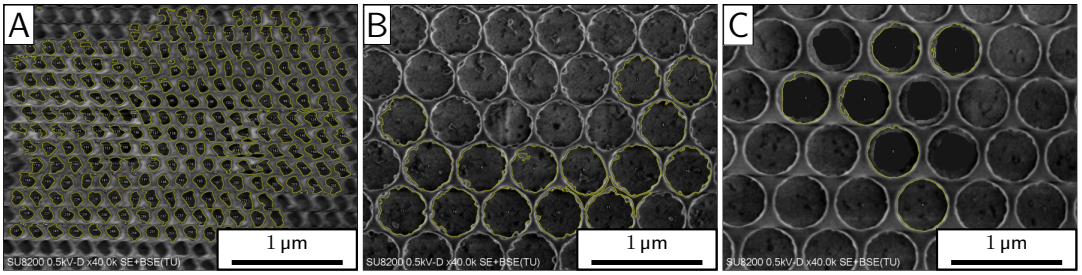

Figure 4.5: SEM images with applied pore detection mask of CSAR resist on sample v3 (Table 3.5) after development with AR-600 546 for 3 min. Sub-figures show different EB dosages D, mask pore diameters d_M and pore distances Δ_M. **A**: $D = 230\,\mu C/cm^2$, $d_M = 150\,nm$, $\Delta_M = 25\,nm$; **B**: $D = 230\,\mu C/cm^2$, $d_M = 450\,nm$, $\Delta_M = 25\,nm$; **C**: $D = 260\,\mu C/cm^2$, $d_M = 450\,nm$, $\Delta_M = 100\,nm$

conditions where detection errors can be observed, with the Fiji detection in yellow on top. In Fig. 4.5A one can see, that pore shapes change due to distortions in the SEM image. In Fig. 4.5B, false negative detection of some light spots towards the pore edges occurs. In Fig. 4.5C, pre-analysis editing of the original SEM image by coloring the pore centers was necessary to enhance contrast and thereby enable pore detection in the first place.

Having observed some unwanted resist residues for development with AR 600-546,

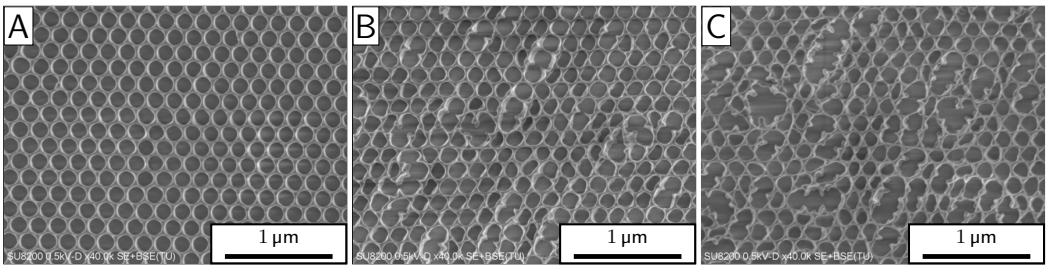

$D = 280\,\mu C/cm^2$ $D = 300\,\mu C/cm^2$ $D = 320\,\mu C/cm^2$

Figure 4.6: SEM images of CSAR resist on sample s3 (Table 3.7) after development with Ethyl L-lactate for 1 min. All sub-figures show images of fields with minimal pore distance $\Delta_M = 25\,nm$ and pore diameter $d_M = 150\,nm$ according to the mask. Contrast value proximity correction (CPC) level is 80%. Sub-figures show different EB dosages D. **A**: $D = 280\,\mu C/cm^2$; **B**: $D = 300\,\mu C/cm^2$; **C**: $D = 320\,\mu C/cm^2$

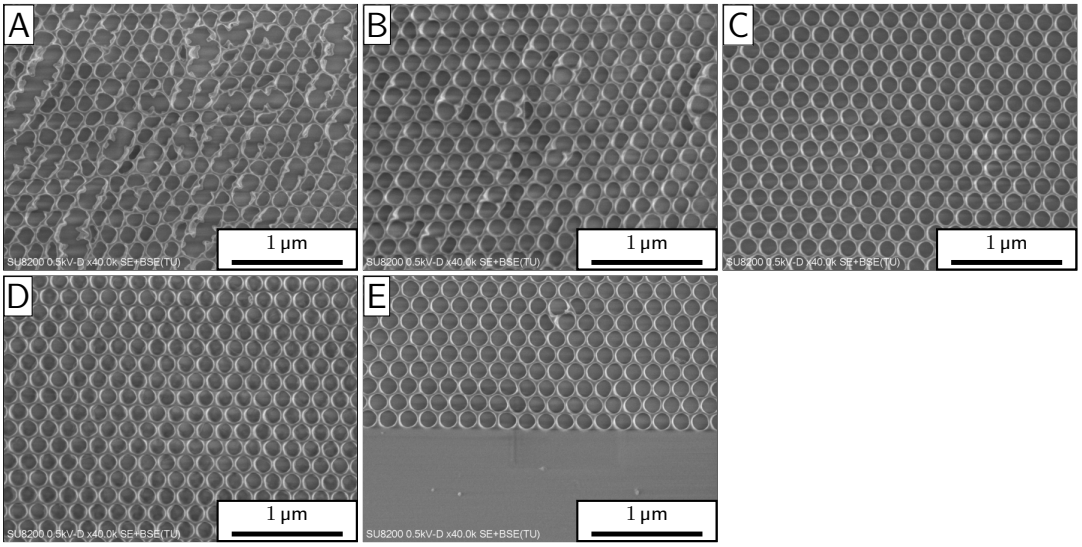

Figure 4.7: SEM images of CSAR resist on sample s3 (Table 3.7) after development with Ethyl L-lactate for 1 min. All sub-figures show images of fields with minimal pore distance $\Delta_M = 25\,\text{nm}$ and pore diameter $d_M = 150\,\text{nm}$ according to the mask. EB dosage is $D = 280\,\mu\text{C/cm}^2$. Sub-figures show different levels of contrast value proximity correction (CPC). **A**: 40% CPC; **B**: 60% CPC; **C**: 80% CPC; **D**: 100% CPC; **E**: 80% CPC, image taken at pattern edge

another developer, namely Ethyl L-lactate was tested. Parameters specified for sample C (Table 3.2) were used. For this developer a different EB dosage was also needed. Therefore, dosage scan and was repeated, resulting in structures shown in Fig. 4.6. Additionally, CPC was optimized, to reduce differences between pattern edge and center. The results are shown in Fig. 4.7. The figures show development at different dosages and CPC levels respectively. One observes, that for dosages of $D = 300\,\mu\text{C/cm}^2$ and $D = 320\,\mu\text{C/cm}^2$ in Fig. 4.6, many individual pores collapsed into bigger pores. The same was true for CPC levels 40% and 60% in Fig. 4.7. Image analysis revealed a pore diameter difference to the expected value of $d_M - d = 9.4\,\text{nm}$ for 80% CPC and $d_M - d = 25.2\,\text{nm}$ for 100% CPC (Table S1). Furthermore, circularity for 80% CPC was closer to the circularity one of the ideal circle, than for 100% CPC (Table S1). Comparison of Fig. 4.7C and Fig. 4.7E showed that pattern quality was rather constant from center to edge (Table S1). Overall, difference $d_M - d$ was reduced and circularity enhanced for development with Ethyl L-lactate after EBL at 80% CPC and $D = 280\,\mu\text{C/cm}^2$ compared to development with AR-600 546 (Tables 4.1 and S1). Here, these conditions chosen for Ethyl L-lactate were selected as ideal development conditions among those tested.
Resist development with Ethyl L-Lactate also worked for sample s4 (Table 3.7; Fig. S7).

Table 4.2: Etch times and gases for the etch rate measurements

Process gas	Layer material	Etch time in s	Etch depth				Etch rate in $nm\,min^{-1}$
			1.	2.	3.	Average	
BCl_3/Cl_2	CSAR	60	109 nm	111 nm		110 nm	110
BCl_3/Cl_2	PMMA 600k	60	201 nm			201 nm	201
BCl_3/Cl_2	Al_2O_3	60	15 nm	16 nm	14 nm	15 nm	15
C_4F_8	Al_2O_3	420	24 nm			24 nm	3.4
C_4F_8	SiO_2	420	1.85 µm	1.87 µm	1.82 µm	1.85 µm	264

Table 4.3: Etch selectivities for SiO_2 pore production process

Process gas	Layer order	Etch selectivity
BCl_3/Cl_2	CSAR : Al_2O_3	7.3 : 1
BCl_3/Cl_2	PMMA 600k : Al_2O_3	13.4 : 1
C_4F_8	Al_2O_3 : SiO_2	1 : 77.6

All together, although unwanted resist residues existed for AR 600-546 development, development with Ethyl L-lactate at 80% CPC and an EB dosage of 280 $\mu C/cm^2$ showed good development resolution and distribution. The image analysis method showed deviations between designed and measured pore sizes.

4.1.2 SiO_2 Etching with ICP

After establishing resist development conditions and possible defects, we can look at how those structures were transferred into SiO_2. It has to be noted however, that resist optimization was executed at the same samples used for etch experiments. For the patterning of SiO_2, exclusively resists developed with AR 600-546 were used. To analyze the etch results, the depth of the etches were first investigated, as it directly correlates to etch times and process parameters. Therefore, sample described in Table 3.4 were used.
The measured etch depths, corresponding to the loss of layer thickness in the z-direction, together with etch rates are shown in Table 4.2. One notices, that CSAR is etched rather fast compared to the lower Al_2O_3 layer.
Those ratios or etch rates are given in Table 4.3 as etch selectivities per process gas, based on the averaged etch rates per gas and material.

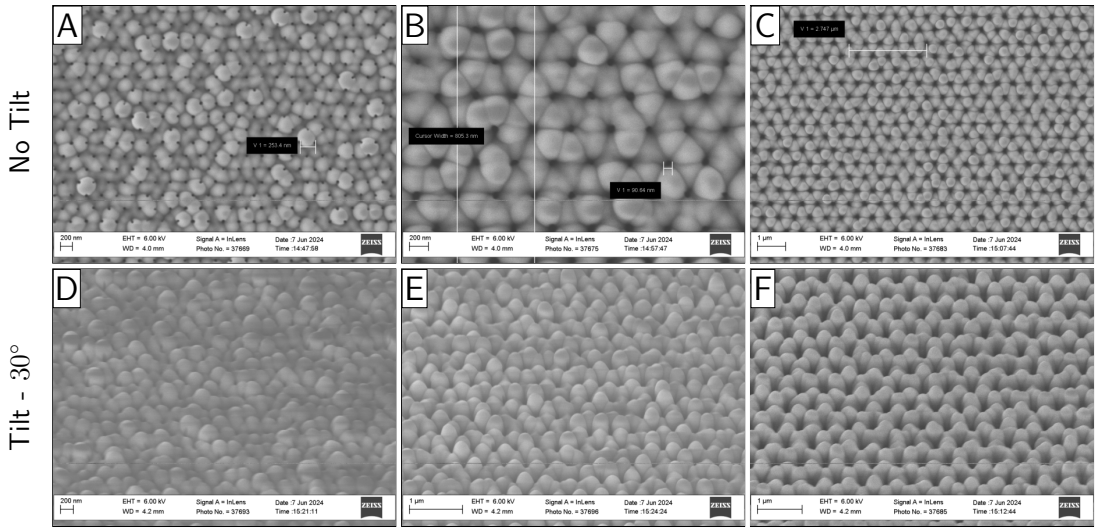

$d_M = 150\,\text{nm}$ $d_M = 300\,\text{nm}$ $d_M = 450\,\text{nm}$

Figure 4.8: SEM images of sample v2 (Table 3.5) after BCl_3/Cl_2 and C_4F_8 etch. Images were taken at FIRST with Zeiss ULTRA 55 plus. EB dosage used for resist patterning was $225\,\mu C/cm^2$. All sub-figures show images of fields with minimal pore distance $\Delta_M = 100\,\text{nm}$ according to the mask. Sub-figures show different mask pore diameters d_M and tilt angles. **A**: $d_M = 150\,\text{nm}$, no tilt; **B**: $d_M = 300\,\text{nm}$, no tilt; **C**: $d_M = 450\,\text{nm}$, no tilt; **D**: $d_M = 150\,\text{nm}$, 30° tilt; **E**: $d_M = 300\,\text{nm}$, 30° tilt; **F**: $d_M = 450\,\text{nm}$, 30° tilt

The first stack design, which was produced at FIRST, was measured for its Al_2O_3 thickness. It is described as wafer 01 in Table 3.3. An alumina layer thickness of 17 nm was measured. This was well below the intended thickness of 30 nm.
For sample v1 (Table 3.5) where wafer 01 was used, the CSAR resist and the Al_2O_3 hard mask were entirely removed after both etching steps and part of the SiO_2 layer was lost based on the color of the remaining layer. The markers after etching were 31 nm deep.

In contrast, for sample v2 of Table 3.5 with wafer 02 (Table 3.3) structures could be etched without general SiO_2 loss. The sample was equipped with a thicker Al_2O_3 mask explaining this protection. Depth measurements after both etch steps revealed a height difference between pattern and surroundings of 1276 nm, averaged over different marker sites. The average marker depth after the BCl_3/Cl_2 etch was found to be 43 nm. After the BCl_3/Cl_2 etch, the remaining resist was measured to be gone, as scratching the surface did not leave a mark. Note, that marker depth after BCl_3/Cl_2 etch could include SiO_2 etch and does not imply a remaining Al_2O_3 thickness of this value.
SEM images in Fig. 4.8 revealed, that the holes were transferred into SiO_2, where the pattern length l matches that of the mask l_M. Yet, the pore geometry is different from

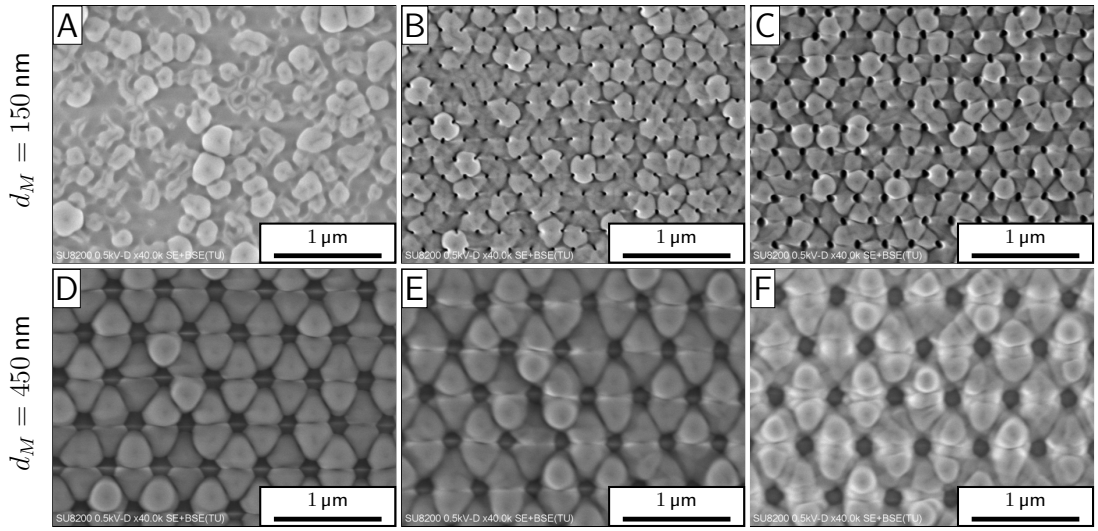

Figure 4.9: SEM images of sample v3 (Table 3.5) after BCl_3/Cl_2 and C_4F_8 etch. EB dosage used for resist patterning was $230\,\mu C/cm^2$. Sub-figures show different mask specifications for pore diameters d_M and pore distances Δ_M. **A**: $d_M = 150\,nm$, $\Delta_M = 25\,nm$; **B**: $d_M = 150\,nm$, $\Delta_M = 50\,nm$; **C**: $d_M = 150\,nm$, $\Delta_M = 100\,nm$; **D**: $d_M = 450\,nm$, $\Delta_M = 25\,nm$; **E**: $d_M = 450\,nm$, $\Delta_M = 50\,nm$; **F**: $d_M = 450\,nm$, $\Delta_M = 100\,nm$

that of the mask presented in Section 4.1.1 and images at 30° tilt revealed that the pore walls spike into the z-direction at the sites where pore distance is maximal. For $d_M = 150\,nm$ and $\Delta_M \leq 50\,nm$, identification of pores was not possible (Fig. S8).

For sample v3 (Table 3.5) with C_4F_8 etch time reduced by 60 s to 360 s, pores still exist at $d_M = 150\,nm$ and $\Delta_M = 50\,nm$, but not for $d_M = 150\,nm$ and $\Delta_M = 25\,nm$. The corresponding SEM images are shown in Fig. 4.9 over various pore distances Δ_M and in Fig. 4.10 for different pore diameters d_M at constant $\Delta_M = 25\,nm$. Pattern repetition lengths l were found to match the specified values within the accuracy of readout, with $\pm 10\,nm$ measurement inaccuracy. Therefore, the values l_M specified in the mask were used for further calculations. Pore diameter and minimal pore distance are listed in Table 4.4.
Difference from the mask specifications of up to 285.5 nm were observed. For $d_M = 450\,nm$, the differences $d_M - d$ were constant within the accuracy of measurement. Apart from that no trend was observed, except that the differences were generally larger for larger pore diameters d_M. These changes in the x-y pattern appeared only after the C_4F_8 etch, while the structures in Al_2O_3 after the BCl_3/Cl_2 etch closely resembled the resist structures (Figs. S10 to S12). The development residues at higher

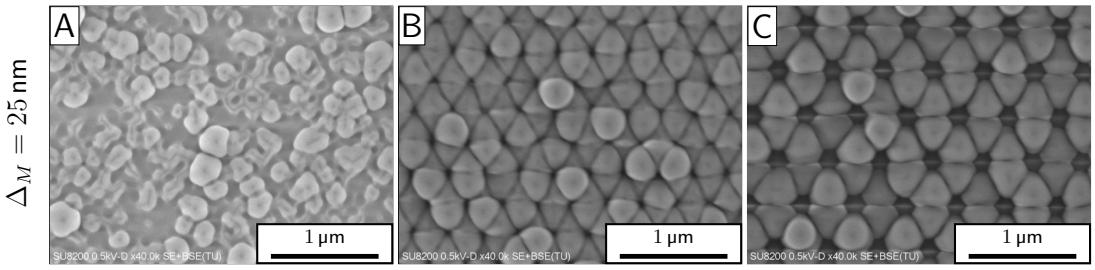

Figure 4.10: SEM images of sample v3 (Table 3.5) after BCl_3/Cl_2 and C_4F_8 etch. EB dosage used for resist patterning was $230\,\mu C/cm^2$. All sub-figures show images of fields with minimal pore distance $\Delta_M = 25\,\mathrm{nm}$ according to the mask. Sub-figures show different mask pore diameters d_M. **A**: $d_M = 150\,\mathrm{nm}$; **B**: $d_M = 300\,\mathrm{nm}$; **C**: $d_M = 450\,\mathrm{nm}$

Table 4.4: Pore diameters (PD) and minimal pore distances (MD) for different mask layouts and EB dosages in sample v3 (Table 3.5) after BCl_3/Cl_2 and C_4F_8 etch. Differences from the ideal value $d_M - d$ and circularities of the pores are also listed. The values are obtained from SEM images in Figs. 4.9, 4.10 and S9.

Mask PD d_M in nm	Mask MD Δ_M in nm	EB dosage D in $\mu C/cm^2$	PD d in nm	MD Δ in nm	Difference $d_M - d$ in nm	Circularity C
150	50	230	28.6	171.4	121.4	0.79
150	100	230	51.3	198.7	98.7	0.80
300	25	230	65.0	260.0	235.0	0.66
300	100	230	104.5	295.5	195.5	0.79
450	25	230	176.7	298.3	273.3	0.63
450	50	230	171.9	328.1	278.1	0.70
450	100	230	164.5	385.5	285.5	0.81

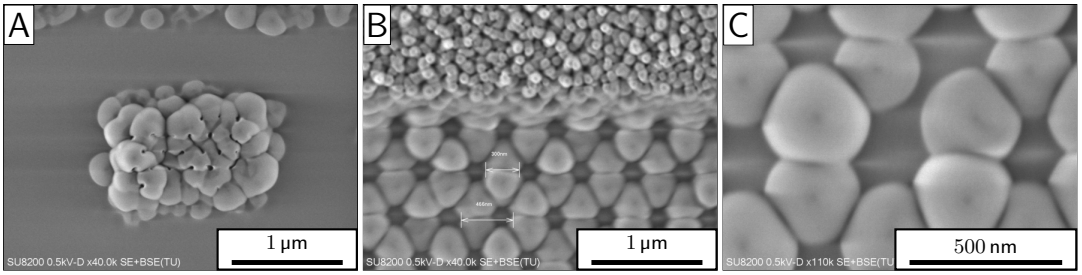

Figure 4.11: SEM images of sample v3 (Table 3.5) after BCl_3/Cl_2 and C_4F_8 etch. Sub-figures show special image sites for different EB dosages D, pore diameters d_M and minimal pore distances Δ_M as specified by the mask. **A**: $d_M = 150\,\text{nm}$, $\Delta_M = 25\,\text{nm}$, $D = 250\,\mu\text{C/cm}^2$, isolated pattern island in otherwise ablated area; **B**: $d_M = 450\,\text{nm}$, $\Delta_M = 25\,\text{nm}$, $D = 230\,\mu\text{C/cm}^2$, image taken at pattern edge; **C**: $d_M = 450\,\text{nm}$, $\Delta_M = 25\,\text{nm}$, $D = 265\,\mu\text{C/cm}^2$, close-up of wall break-through

dosages ($250\,\mu\text{C/cm}^2$, $265\,\mu\text{C/cm}^2$) were transferred into SiO_2 and for $d_M = 150\,\text{nm}$ and $\Delta_M = 25\,\text{nm}$ the walls are ablated almost entirely (Fig. S13). Yet, effects observed at different dosages D provided some additional insights and are presented in Fig. 4.11.

There, special image sites of the patterns after the final etch for sample v3 (Table 3.5) are shown. In Fig. 4.11A an isolated non-ablated island with pore arrays according to the pattern length was observed. Fig. 4.11B shows the pattern edge at $d_M = 450\,\text{nm}$, $\Delta_M = 25\,\text{nm}$ and $D = 230\,\mu\text{C/cm}^2$, where a lowering of the structured parts compared to the surroundings was observed. Fig. 4.11 shows the formation of globular structures next to a wall break.
Finally, looking also at the z structure of sample v3 (Table 3.5), average marker depths were found to be 43 nm after BCl_3/Cl_2 etch and 1347 nm after the additional C_4F_8 etch.

In sample v4 (Table 3.5) the patterning of PECVD oxide and thermal oxide was compared. This was based on the initial assumption, that PECVD SiO_2 structure might have been responsible for the inaccurate pattern transfer. However, the same wall widening was observed for thermal oxide (Fig. 4.12). The direct comparison for samples with $\Delta_M = 100\,\text{nm}$ is shown in Fig. 4.12. Different sub-structures were observed on top of the walls and the differences to ideal pore size $d_M - d$ were slightly smaller for the thermal oxide (Table S3).
The lowering observed in Fig. 4.11B was checked in sample v4 with the profilometer, by scanning over the pattern edges for various pore specifications and comparing PECVD and thermal oxide. The measurements are listed in Table S2. Measurements with this technique over flat resist structures and observation under the microscope (Keyence, Urdorf, Belgium; VHX 6000) revealed, that the profilometer itself damages the thin

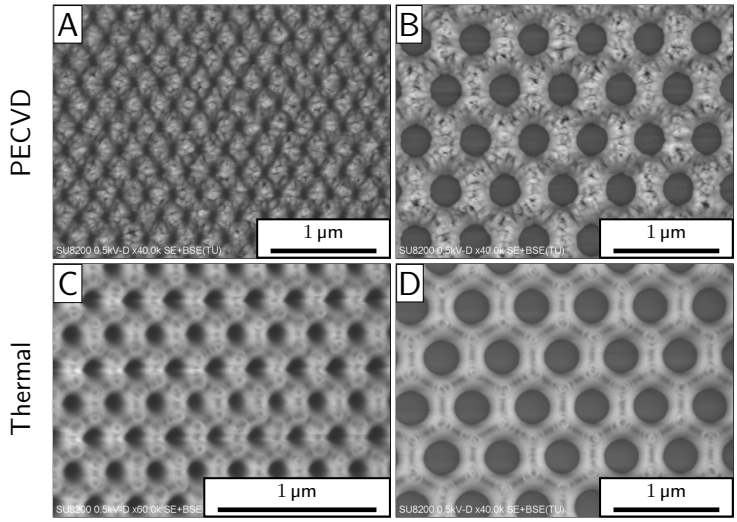

Figure 4.12: SEM images of sample v4 (Table 3.5) after BCl_3/Cl_2 and C_4F_8 etch. EB dosage used for resist patterning was $230\,\mu C/cm^2$. All sub-figures show images of fields with minimal pore distance $\Delta_M = 100\,\mathrm{nm}$ according to the mask. Sub-figures show mask pore diameters d_M in comparison of SiO_2 deposited with PECVD and SiO_2 applied by thermal oxidation of the wafer. **A**: $d_M = 150\,\mathrm{nm}$, PECVD oxide; **B**: $d_M = 450\,\mathrm{nm}$, PECVD oxide; **C**: $d_M = 150\,\mathrm{nm}$, thermal oxide; **D**: $d_M = 450\,\mathrm{nm}$, thermal oxide

walls and might therefore measure a bigger height difference, than the actual value before analysis. For the data in Table S2, a generally higher height difference for thermal oxide is observed and the gaps are bigger for thinner walls and in the case of PECVD oxide also for bigger pores.
The average marker depth after BCl_3/Cl_2 and C_4F_8 etch for sample v4 (Table 3.5) was 810 nm for PECVD oxide and 815 nm for thermal oxide.

Summarizing the observations at the SiO_2 stack, pores widened even for reduced etch times and lost their structure. Patterns were not correctly reproduced into SiO_2.

4.1.3 Silicon Etching with Bosch vs HBr-based ICP Process

After not being able to achieve desired pore functionalities in the SiO_2 stack design, etches into silicon with a HBr-based ICP process and a Bosch DRIE process was investigated. For the first sample (sample s1, Table 3.7), the ICP process was investigated and a 500 nm thick SiO_2 mask was used. An ICP etch of 8 min with gas mixture 01 (only HBr) from Table 3.6 was tested as second etch step after the RIE. Fig. 4.13 and Fig. 4.14 show SEM images after each of the two steps over different

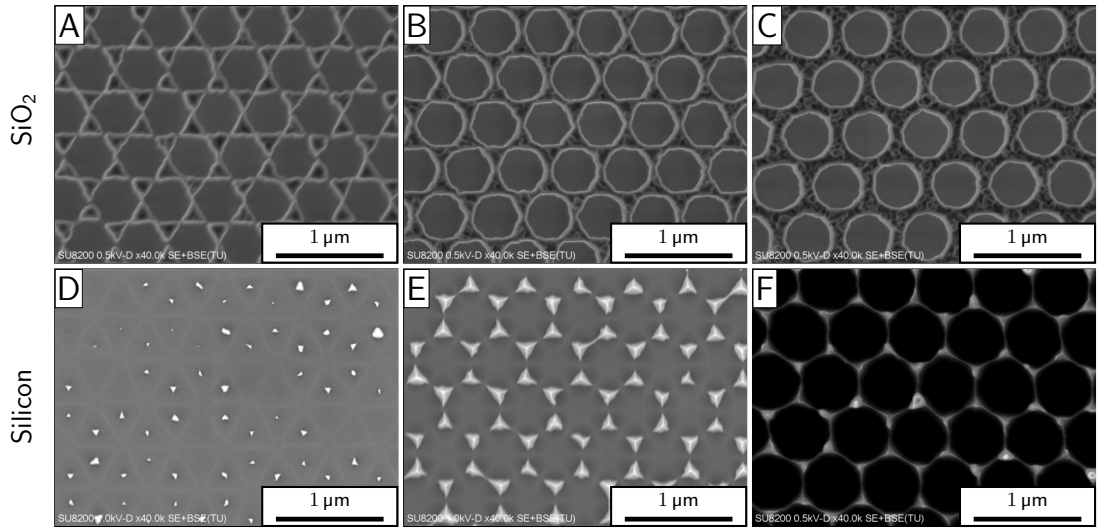

Figure 4.13: SEM images of sample s1 (Table 3.7) after either only RIE or RIE and ICP etch. The ICP etch was executed with the gas mixture 01 from Table 3.6 for 8 min. All sub-figures show images of fields with pore diameter $d_M = 450\,\mathrm{nm}$ according to the mask. Sub-figures show different mask pore distances Δ_M. **A**: $\Delta_M = 25\,\mathrm{nm}$, only RIE; **B**: $\Delta_M = 50\,\mathrm{nm}$, only RIE; **C**: $\Delta_M = 100\,\mathrm{nm}$, only RIE; **D**: $\Delta_M = 25\,\mathrm{nm}$, both etch steps; **E**: $\Delta_M = 50\,\mathrm{nm}$, both etch steps; **F**: $\Delta_M = 100\,\mathrm{nm}$, both etch steps

pore distances Δ_M and pore diameters Δ_M. While the patterns are transferred cleanly into SiO_2 with the RIE, wall thickness is lost during the ICP etch up to complete wall ablation for the thinnest walls of $\Delta_M = 25\,\mathrm{nm}$ in Fig. 4.13.
For the following experiments, HBr ICP etch was optimized by adding small amounts of O_2 to increase selectivity, but slow down overall etching. The etch selectivities determined for the ICP gas mixtures 02 and 03 introduced in Table 3.6 with

Table 4.5: Etch selectivities of thermal SiO_2 to silicon for HBr, O_2 gas mixtures in ICP etch process

Gas mixture (Table 3.6)	Mode of acquisition	Selectivity (SiO_2:Si)
01	Data by previous tool users	1:3
02	Experiment	1:7.2
03	Experiment	1:9

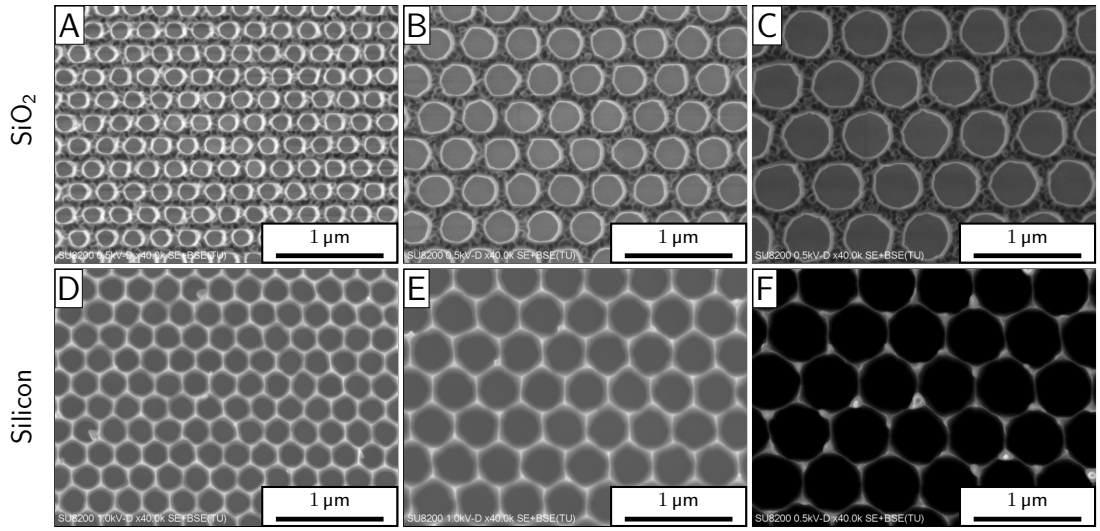

Figure 4.14: SEM images of sample s1 (Table 3.7) after either only RIE or RIE and ICP etch. The ICP etch was executed with the gas mixture 01 from Table 3.6 for 8 min. All sub-figures show images of fields with minimal pore distance $\Delta_M = 100\,\mathrm{nm}$ according to the mask. Sub-figures show different mask pore diameters d_M. **A**: $d_M = 150\,\mathrm{nm}$, only RIE; **B**: $d_M = 300\,\mathrm{nm}$, only RIE; **C**: $d_M = 450\,\mathrm{nm}$, only RIE; **D**: $d_M = 150\,\mathrm{nm}$, both etch steps; **E**: $d_M = 300\,\mathrm{nm}$, both etch steps; **F**: $d_M = 450\,\mathrm{nm}$, both etch steps

respectively 3.7% and 7.5% O_2 are listed in Table 4.5. Although gas mixture 03 had the highest selectivity, the surface at the bottom of the structures was also found to be very rough with spikes of more than 200 nm height.
Looking at sample s1 (Table 3.7), where gas mixture 01 (Table 3.6) was used, etch selectivity was not measured but data from previous users taken as reference. The marker depth before the ICP and after the RIE was found to be 521 nm. The average total depth after both etches was measured to be 1423 nm. The average marker depth change during the 8 min ICP etch step hence was 902 nm. Here, no CSAR was measured to remain after 48.5 min of previous RIE and SiO_2 was still present after the ICP etch. The etch step therefore corresponded to the difference in SiO_2 and silicon etch depth. This etch step change of 902 nm was within range for an estimated silicon etch depth of 1320 nm and SiO_2 etch depth of 440 nm corresponding to a theoretical difference of 880 nm. This estimation again was based on user data. Gas mixture 02 was chosen as optimal, as it had the highest selectivity while not yet inducing irregularities. Particularly for small pores these irregularities could potentially have resulted in pore blocking.
For sample s2 (Table 3.7), a new wafer with thinner SiO_2 layer of 300 nm thickness

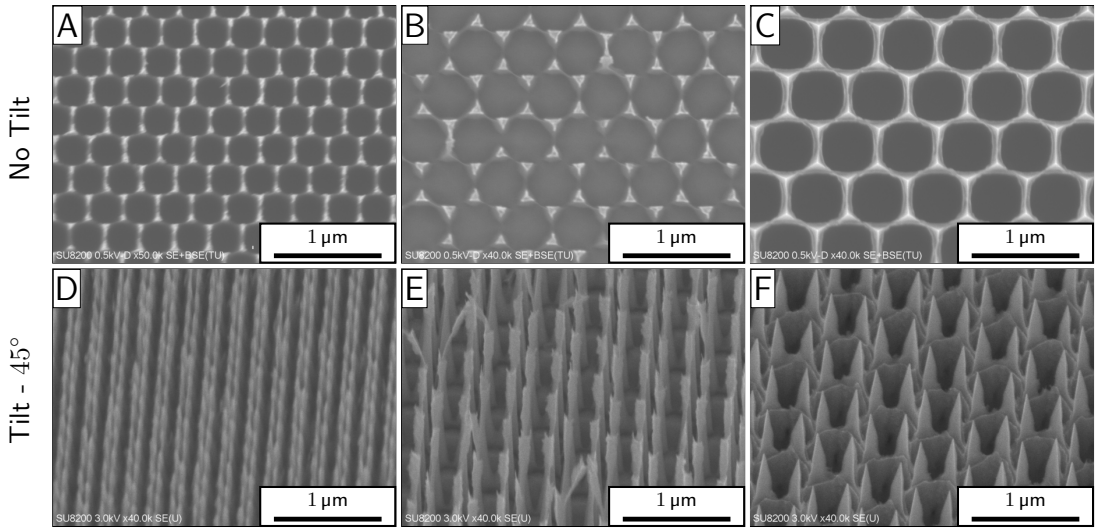

$d_M = 150\,\text{nm}$, $\Delta_M = 100\,\text{nm}$ | $d_M = 450\,\text{nm}$, $\Delta_M = 25\,\text{nm}$ | $d_M = 450\,\text{nm}$, $\Delta_M = 100\,\text{nm}$

Figure 4.15: SEM images of sample s2 (Table 3.7) after RIE and ICP etch. SiO_2 was removed with buffered hydrogen fluoride (BHF) before image acquisition. Sub-figures show different mask specifications for pore diameters d_M and pore distances Δ_M for different tilt angles. **A**: $d_M = 150\,\text{nm}$, $\Delta_M = 100\,\text{nm}$, no tilt; **B**: $d_M = 450\,\text{nm}$, $\Delta_M = 25\,\text{nm}$, no tilt; **C**: $d_M = 450\,\text{nm}$, $\Delta_M = 100\,\text{nm}$, no tilt; **D**: $d_M = 150\,\text{nm}$, $\Delta_M = 100\,\text{nm}$, 45° tilt; **E**: $d_M = 450\,\text{nm}$, $\Delta_M = 25\,\text{nm}$, 45° tilt; **F**: $d_M = 450\,\text{nm}$, $\Delta_M = 100\,\text{nm}$, 45° tilt

was used. The ICP etch with optimized gas mixture (gas mixture 02, Table 3.6) was put to practice and executed for 9 min after etching 28 min with RIE. Fig. 4.15 shows the produced structures after removal of remaining SiO_2 with BHF by Ute Drechsler. The structures without the tilt resembled those of sample s1, but images at 45° tilt revealed, that the pore walls had very irregular heights resulting in pillars around the sites of maximal pore distance. Despite the thinner SiO_2 layer compared to sample s1, a higher total etch depth at the marker of 2247 nm was achieved, as suggested by the higher selectivity.

Going back one step, RIE etch was also optimized for sample s2. Images of the patterns after 15 min and 28 min RIE times in Fig. 4.16 revealed, that the structures were transferred with little shape changes into SiO_2, constant over different etch times.
The roughness on the wall surfaces seemed to be part of the remaining CSAR resist, as comparison of images before and after removal of CSAR resist with DMSO in Fig. 4.17 for 28 min etch time showed.
The total etch depths measured for the RIE are listed in Table 4.6. An average etch

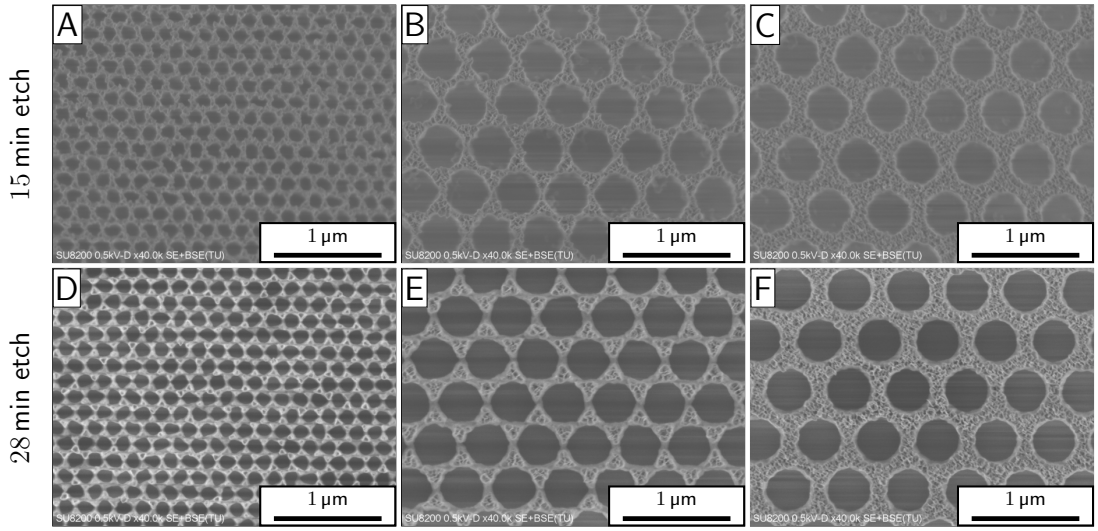

Figure 4.16: SEM images of sample s2 (Table 3.7) after RIE of different durations. Sub-figures show different mask specifications for pore diameters d_M and pore distances Δ_M. **A**: $d_M = 150\,\text{nm}$, $\Delta_M = 25\,\text{nm}$, 15 min etch time; **B**: $d_M = 450\,\text{nm}$, $\Delta_M = 25\,\text{nm}$, 15 min etch time; **C**: $d_M = 450\,\text{nm}$, $\Delta_M = 100\,\text{nm}$, 15 min etch time; **D**: $d_M = 150\,\text{nm}$, $\Delta_M = 25\,\text{nm}$, 28 min etch time; **E**: $d_M = 450\,\text{nm}$, $\Delta_M = 25\,\text{nm}$, 28 min etch time; **F**: $d_M = 450\,\text{nm}$, $\Delta_M = 100\,\text{nm}$, 28 min etch time

Table 4.6: Etch depths and rates of CSAR and SiO_2 with 75 W RIE with 38 sccm Ar and 12 sccm CHF_3 gases. Values are taken for different etch times.

Etch time in min	Material	Etch depth in nm	Etch rate in $\text{nm}\,\text{min}^{-1}$
15	CSAR	77	5.1
15	SiO_2	168	11.2
28	CSAR	159	5.7
28	SiO_2	300	10.7
36	CSAR	202	5.6
36	SiO_2	496	13.8

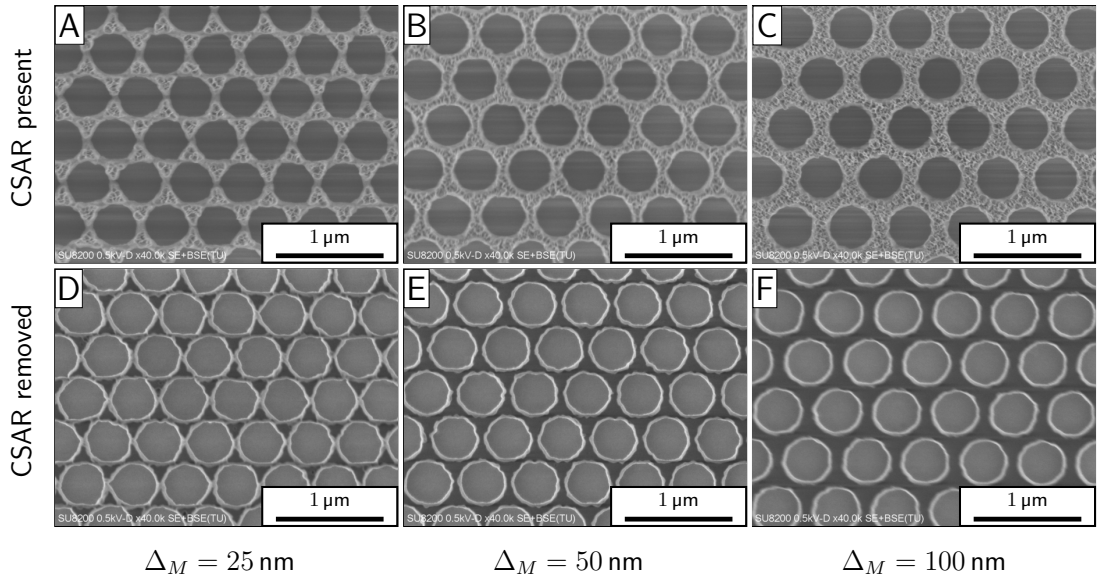

Figure 4.17: SEM images of sample s2 (Table 3.7) after RIE of 28 min. All sub-figures show images of fields with pore diameter $d_M = 450\,\text{nm}$ according to the mask. Sub-figures show different mask pore distances Δ_M compared before and after CSAR removal with DMSO. **A**: $\Delta_M = 25\,\text{nm}$, CSAR present; **B**: $\Delta_M = 50\,\text{nm}$, CSAR present; **C**: $\Delta_M = 100\,\text{nm}$, CSAR present; **D**: $\Delta_M = 25\,\text{nm}$, CSAR removed; **E**: $\Delta_M = 50\,\text{nm}$, CSAR removed; **F**: $\Delta_M = 100\,\text{nm}$, CSAR removed

rate for CSAR of $5.5\,\text{nm}\,\text{min}^{-1}$ and $11.9\,\text{nm}\,\text{min}^{-1}$ for thermal SiO_2 resulted for those measurements.
The surface was investigated with SEM tilt images of the SiO_2 mask that showed a slight surface roughness of the walls up to almost having an array of little spikes for $d_M = 150\,\text{nm}$ and $\Delta_M = 25\,\text{nm}$ (Fig. S14A-D). The pore walls at the pattern edges however appeared to continue flat into the surroundings (Fig. S14E,F).

Next, the Bosch DRIE process was tested on patterns structured properly with RIE. Fig. 4.18 shows SEM images of sample s2 (Table 3.7) after 30 min RIE and consecutive 20 cycles DRIE. The tilt images revealed that for the samples of pore distance $\Delta_M \leq 50\,\text{nm}$ in Fig. 4.18A and Fig. 4.18B, the walls were partially broken at the DRIE scallops. Comparison of Fig. 4.18D and Fig. 4.18E showed enhanced wall break-through towards the pattern edges.
Different mask pore distances and pore diameters correctly reproduced different patterns after DRIE (Figs. S15 and S16).
Next, after this first success, the sample s2 was submitted to Scientific Center for Optical and Electron Microscopy (ScopeM) of ETH Zürich for the collection of FIB-SEM

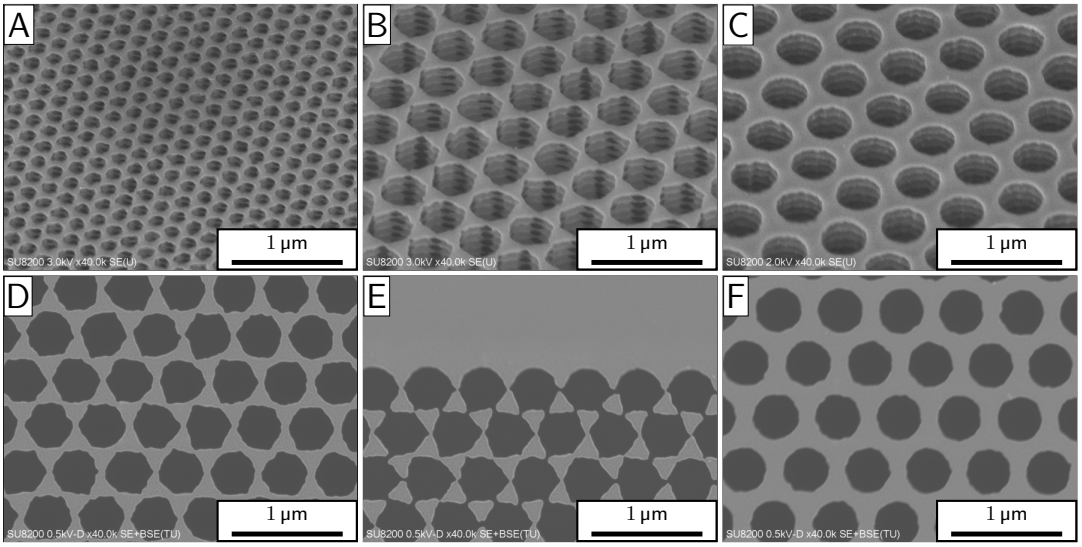

Figure 4.18: SEM images of sample s2 (Table 3.7) after RIE and DRIE. Sub-figures show different mask specifications for pore diameters d_M and pore distances Δ_M for different tilt angles. **A**: $d_M = 150\,\text{nm}$, $\Delta_M = 50\,\text{nm}$, 45° tilt; **B**: $d_M = 450\,\text{nm}$, $\Delta_M = 25\,\text{nm}$, 45° tilt; **C**: $d_M = 450\,\text{nm}$, $\Delta_M = 100\,\text{nm}$, 45° tilt; **D**: $d_M = 450\,\text{nm}$, $\Delta_M = 25\,\text{nm}$, no tilt; **E**: $d_M = 450\,\text{nm}$, $\Delta_M = 25\,\text{nm}$, no tilt, image taken at pattern edge; **F**: $d_M = 450\,\text{nm}$, $\Delta_M = 100\,\text{nm}$, no tilt

images. By drilling into the pattern and tilting the view, images of the z-profile can be collected with this tool. FIB-SEM images of the DRIE etched sample s2 (Table 3.7) were taken after SiO_2 removal at ScopeM by Anne Greet Bittermann. The results are shown in Fig. 4.19 and Fig. 4.20. Fig. 4.19A shows a top view of the holes that were drilled. Fig. 4.19B-D show the corresponding z images. The average depth according to the two measurement methods inside holes (yellow) and hole walls (black) are shown in Table 4.7.
Etch depths were smaller for smaller pores and also for biggest pores well below average marker depth of 2.233 µm. Wall thickness and position in the pattern did not have a critical influence on pore depth. Etching with DRIE hence provided a good process draft to realize the desired parameters.

After this initial success, the DRIE process was further optimized at samples s3 and s4 (Table 3.7). Sample s3 was mainly used to optimize resist development as described in Section 4.1.1 for Ethyl L-lactate. We therefore looked into transfer of different resist developments into silicon. Structures of $\Delta_M = 50\,\text{nm}$ transferred with $d_M - d \leq 40\,\text{nm}$ for EB dosages $280\,\mu\text{C/cm}^2$, $300\,\mu\text{C/cm}^2$ and $320\,\mu\text{C/cm}^2$ and with differences of less than 10 nm in between dosages (Table S4 and Fig. S17).

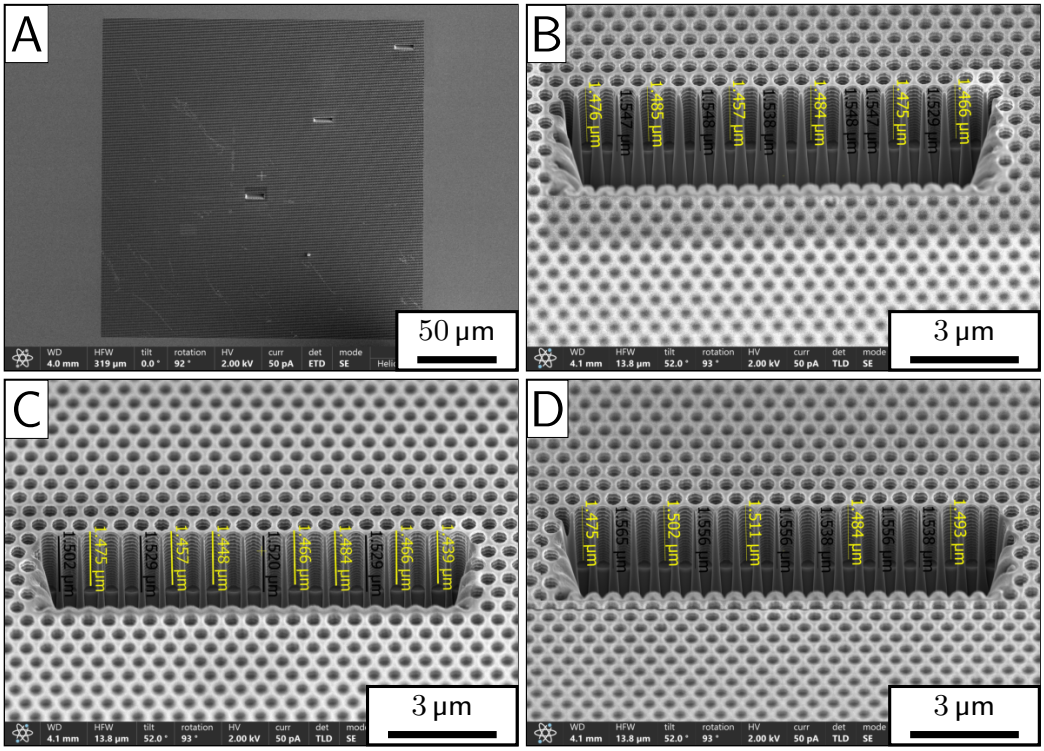

Figure 4.19: FIB-SEM images of sample s2 (Table 3.7) after RIE and DRIE at 52° stage tilt with length corrected measurements. All sub-figures show $d_M = 450\,\text{nm}$ and $\Delta_M = 100\,\text{nm}$ for different pattern positions and stage tilts. Images were taken by Anne Greet Bittermann. **A**: no stage tilt, top view; **B**: 52° stage tilt, center; **C**: 52° stage tilt, between edge and center; **D**: 52° stage tilt, edge

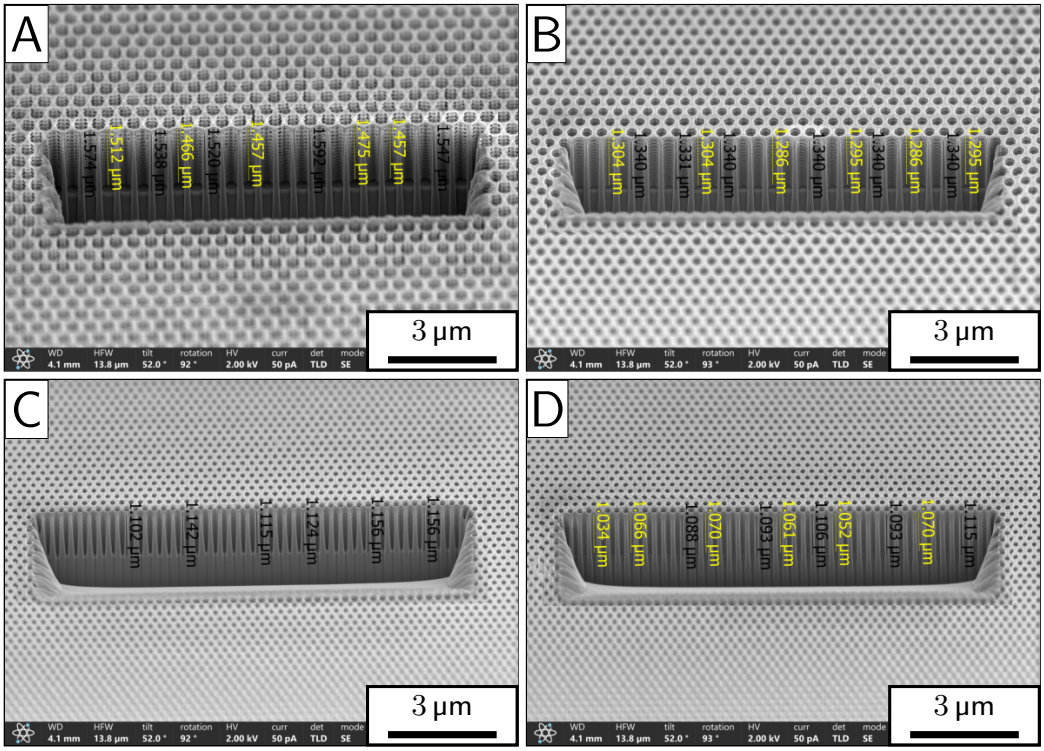

Figure 4.20: FIB-SEM images of sample s2 (Table 3.7) after RIE and DRIE at 52° stage tilt with length corrected measurements. Sub-figures show different pattern positions. Images were taken by Anne Greet Bittermann. **A**: $d_M = 450\,\text{nm}$, $\Delta_M = 25\,\text{nm}$, center; **B**: $d_M = 300\,\text{nm}$, $\Delta_M = 100\,\text{nm}$, center; **C**: $d_M = 150\,\text{nm}$, $\Delta_M = 100\,\text{nm}$, center; **D**: $d_M = 450\,\text{nm}$, $\Delta_M = 100\,\text{nm}$, edge

Table 4.7: Average hole depths per measurement method for various mask pore diameter (PD) and minimal distances (MD) of sample s2 (Table 3.7). Measurements are averaged over values inside pores (yellow) and at pore walls (black) with Figs. 4.19 and 4.20.

Mask PD d_M in nm	Mask MD Δ_M in nm	Position in pattern	Pore depth inside pores in µm	Pore depth at walls in µm
150	100	center		1.133
150	100	edge	1.059	1.099
300	100	center	1.295	1.339
450	25	center	1.473	1.554
450	100	center	1.474	1.543
450	100	between	1.462	1.520
450	100	edge	1.493	1.552

The treatment with 100 W O_2 plasma in the RIE tool smoothed the wall z surface and removed irregularities at the wall edges (Fig. S18).
Tilt images in Fig. 4.21A, B and pattern edge images in Fig. 4.21C showed that a SiO_2 layer remains on top of the silicon structures identified by the scallops produced by DRIE and that the pattern transition to the surroundings is flat. Measurements of scratches to the CSAR resist in between etching and cleaning steps revealed an etch depth of 26.5 nm into SiO_2 throughout the 20 DRIE cycles. This corresponds to 1.3 nm per cycle. 28.5 nm of CSAR were measured to remain after DRIE. This corresponded

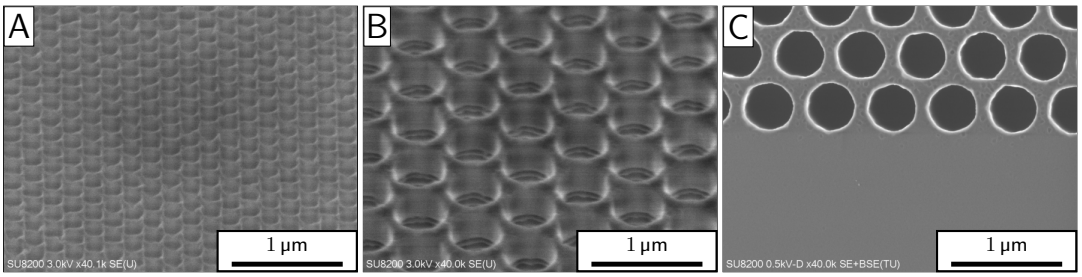

Figure 4.21: SEM images of sample s3 (Table 3.7) after RIE and DRIE and a consequent O_2 plasma cleaning step. EB dosage used for resist patterning was 280 µC/cm^2. -figures show different mask specifications for pore diameters d_M and pore distances Δ_M. **A**: $d_M = 150$ nm, $\Delta_M = 50$ nm, 45° tilt; **B**: $d_M = 450$ nm, $\Delta_M = 100$ nm, 45° tilt; **C**: $d_M = 450$ nm, $\Delta_M = 100$ nm, image taken at pattern edge, no tilt

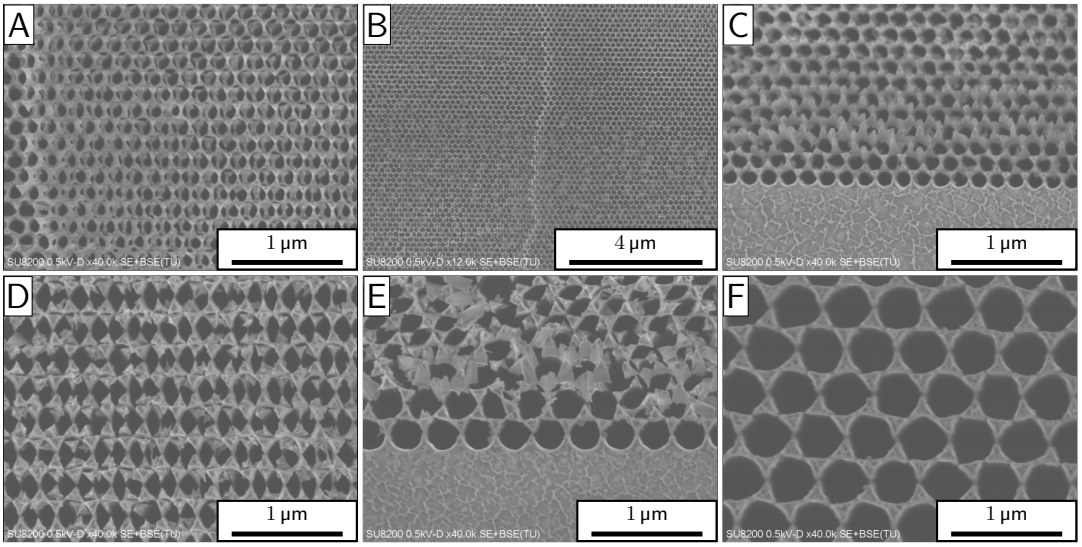

Figure 4.22: SEM images of sample s3 (Table 3.7) after RIE and DRIE. EB dosage used for resist patterning was 280 µC/cm^2. All sub-figures show images of fields with minimal pore distance $\Delta_M = 25$ nm according to the mask. Sub-figures show different mask specifications for pore diameters d_M at different positions in the pattern. **A**: $d_M = 150$ nm; **B**: $d_M = 150$ nm; **C**: $d_M = 150$ nm, image taken at pattern edge; **D**: $d_M = 300$ nm; **E**: $d_M = 300$ nm, image taken at pattern edge; **F**: $d_M = 450$ nm

to a loss of 96 nm compared to before DRIE or removal of 4.8 nm per cycle.
For sample s3 (Table 3.7) with the described etch parameters, structuring of walls at minimal pore distances $\Delta_M \leq 50$ nm resulted in shifts of structured silicon or SiO_2 layers relative to each other in x, y directions, as observed in Fig. 4.22. Fig. 4.22B shows a edge, where the layers were fractured and Fig. 4.22C, E show pillar residues.

Looking at sample s4 (Table 3.7) the limitations for achievable pore distances were precisely investigated. Fig. 4.23 shows the different pore distances of down to 30 nm for $d_M = 300$ nm. This is the pore diameter that is closest to AAO activation optimum. Measured differences between mask design and structure $d_M - d$ in Table 4.8 were smaller than 40 nm, but bigger than 25 nm.
Additionally, pore depth limitations for 150 nm pores were tested by increasing the DRIE cycle number to 25 cycles. This did not result in any differences regarding the x, y patterning (Fig. S20).
The FIB-SEM image in Fig. 4.24 taken by Michael Stiefel at the BRNC shows an average etch depth into Silicon of 1.184 µm and that 272 nm of SiO_2 hard mask remained after DRIE. This image was obtained for sample s4 (Table 3.7) after 25 DRIE cycles. This corresponds to a total pore depth of 1.456 µm. Hence, an aspect ratio of 9.7:1 was

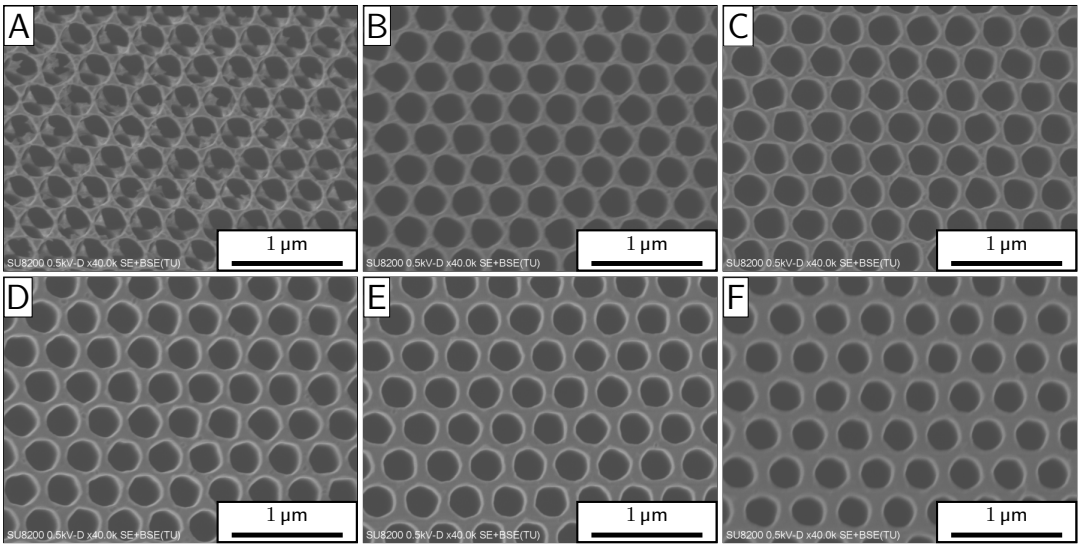

Figure 4.23: SEM images of sample s4 (Table 3.7) after RIE and DRIE. All sub-figures show images of fields with pore diameter $d_M = 300\,\text{nm}$ according to the mask. Sub-figures show different mask specifications for minimal pore distances Δ_M. **A**: $\Delta_M = 30\,\text{nm}$; **B**: $\Delta_M = 40\,\text{nm}$; **C**: $\Delta_M = 50\,\text{nm}$; **D**: $\Delta_M = 70\,\text{nm}$; **E**: $\Delta_M = 90\,\text{nm}$; **F**: $\Delta_M = 110\,\text{nm}$

Table 4.8: Pore diameters (PD) and minimal pore distances (MD) for different mask layouts and EB dosages for sample s4 (Table 3.7) after DRIE etch. Differences from the ideal value $d_M - d$ and circularities of the pores are also listed. The values are obtained from SEM images in Fig. 4.23.

Mask PD d_M in nm	Mask MD Δ_M in nm	PD d in nm	MD Δ in nm	Difference $d_M - d$ in nm	Circularity C
300	40	270.5	69.5	29.5	0.89
300	50	272.2	77.8	27.8	0.89
300	70	260.6	109.4	39.4	0.89
300	90	266.2	123.8	33.8	0.89
300	110	268.1	141.9	31.9	0.89

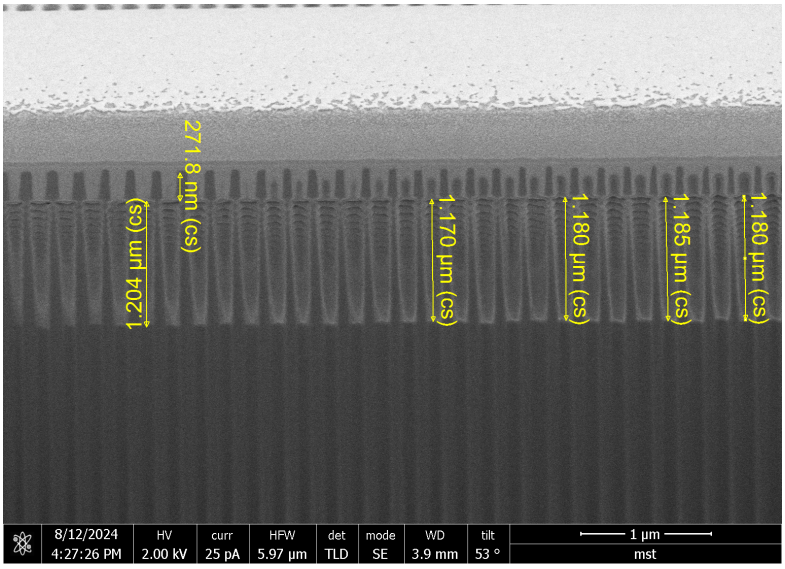

Figure 4.24: FIB-SEM image of sample s4 (Table 3.7) after RIE and 25 DRIE cycles at 52° stage tilt with length corrected measurements. The image was taken at the center of the $d_M = 150\,\text{nm}$ and $\Delta_M = 50\,\text{nm}$ pattern. An additional platinum layer was applied with the FIB-SEM that is visible in the image top. Images were taken by Michael Stiefel.

achieved for the smallest tested pore diameter of 150 nm and 50 nm thin walls.

Therefore, etching with DRIE showed improved features in terms of x-y resolution and z height distribution compared to HBr ICP etching. However, increased etch selectivities were found for HBr etched SiO_2 to silicon for an added 3.7% of O_2.

4.1.4 Production of Porous Substrates for T Cell Experiments

With the established process for DRIE, structures were successfully written into silicon, as specified in Section 3.7. Fig. 4.25 shows the five final geometries with pore diameters ranging from 150 nm to 450 nm and pore distances between 50 nm and 500 nm. Those values have been chosen around pore diameters ideal for AAO based activation and distances providing a huge range of pore densities. Despite proper geometry development, some irregularities remain even after O_2 plasma clean (Fig. 4.25).
Looking at the chip sizes of 5.6 mm by 5.2 mm, the diced silicon chips did not fit into the wells, even though the aluminum samples of same size did. The reason for that was the comparably high stiffness and thickness. After breaking off approximately 0.2 mm per chip with tweezers after scratching with a diamond pen, the chips fitted into the wells. The edge was broken off such, that the chip resulted to measure 5.2 mm by 5.4 mm. A cell culture plate with the produced substrates together with aluminum and AAO cutouts for reference measurements was successfully prepared and handed over to Tamara Zünd.

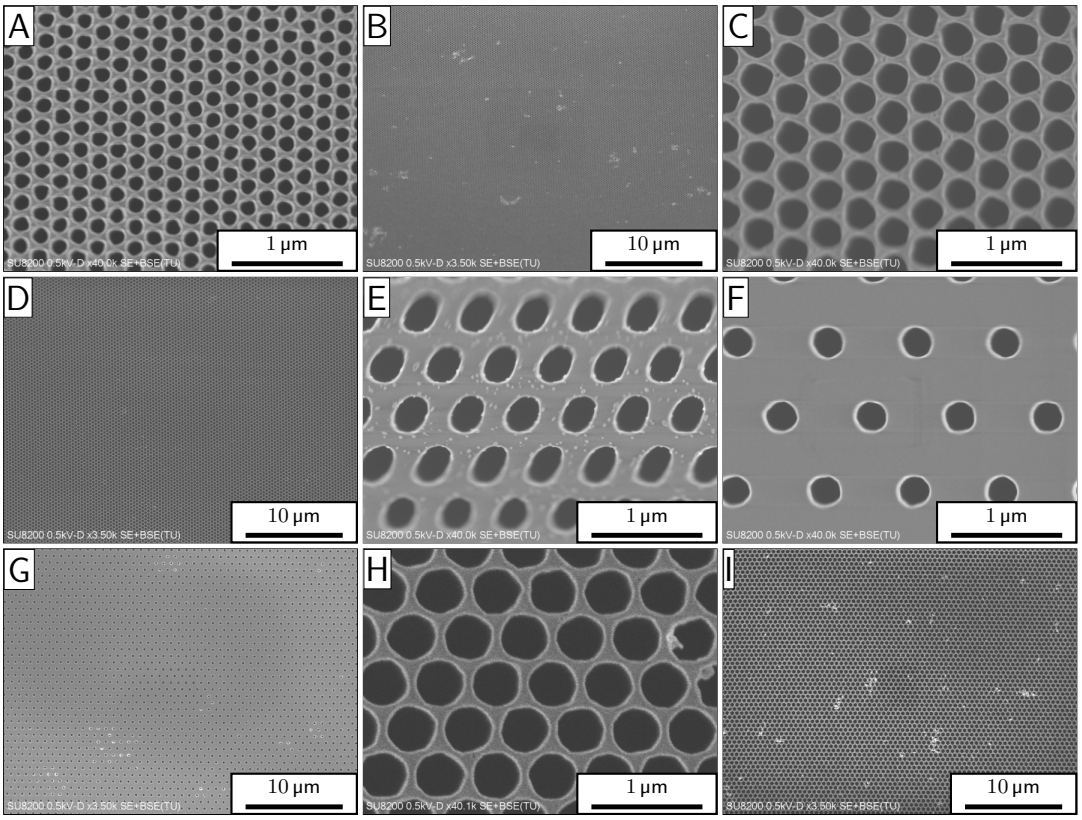

Figure 4.25: SEM images of final chips for cell seeding after 30 min RIE and consecutive 25 DRIE cycles. Sub-figures show different mask specifications for pore diameters d_M and minimal pore distance Δ_M. **A**: $d_M = 150\,\text{nm}$, $\Delta_M = 50\,\text{nm}$; **B**: $d_M = 150\,\text{nm}$, $\Delta_M = 50\,\text{nm}$; **C**: $d_M = 300\,\text{nm}$, $\Delta_M = 50\,\text{nm}$; **D**: $d_M = 300\,\text{nm}$, $\Delta_M = 50\,\text{nm}$; **E**: $d_M = 300\,\text{nm}$, $\Delta_M = 200\,\text{nm}$; **F**: $d_M = 300\,\text{nm}$, $\Delta_M = 500\,\text{nm}$; **G**: $d_M = 300\,\text{nm}$, $\Delta_M = 500\,\text{nm}$; **H**: $d_M = 450\,\text{nm}$, $\Delta_M = 50\,\text{nm}$; **I**: $d_M = 450\,\text{nm}$, $\Delta_M = 50\,\text{nm}$

4.1.5 Discussion

The development of CSAR resist was optimized for minimal irregularities and a close match to the theoretical mask specifications, achieving ideal results with a 1-minute development in Ethyl L-Lactate after exposure with an electron beam dosage of $280\,\mu C/cm^2$ and 80% CPC. Under these conditions, the required resolution for 288 nm CSAR layers was successfully achieved. Comparatively, development with AR 600-546 was more effective with a longer development time of 3 minutes rather than 1 minute, suggesting that a slower development rate may enhance resolution by allowing more controlled development of finer features.

However, the image analysis method used for evaluating pore structures demonstrated limitations in accurately detecting pores in images affected by bright SEM image effects and distortions. Analysis showed that resist residues resulted in an average deviation of 31.2 nm from the ideal values, suggesting that measurement inaccuracies could be in the order of 10 nm with an additional constant offset. This discrepancy could be attributed to blurring at image edges, which is filtered out during threshold analysis. Despite these limitations, this method provided a more standardized approach than manual length measurements, although the results should be considered relative rather than absolute representations of pore parameters.

The 13 nm discrepancy in Al_2O_3 thickness produced via ALD at FIRST (Table 3.3) is likely due to inaccuracies in both the measurement method and the process parameters, as noted by previous users. Nonetheless, this variance did not significantly impact the subsequent process optimization.

A comparison of etch depths after BCl_3/Cl_2 and C_4F_8 etching revealed that the marker depth for sample v2 was smaller than for sample v3 (Table 3.3), even though sample v2 underwent a longer etching duration on the same wafer. The only variable between the two samples was the CSAR development, suggesting that the 1-minute development for sample v2 may have been incomplete, affecting the overall etch depth.

The layer stacks of Wafers 02 and 03 (Table 3.3) had a CSAR to Al_2O_3 thickness ratio of 6.4:1, as measured. Coupled with an etch selectivity of 7.3:1 (Table 4.3), these results indicate that Al_2O_3 mask might already be lost after BCl_3/Cl_2 etch. For the etch time of 195 seconds, CSAR with a thickness of 288 nm is fully removed after approximately 157 seconds, and in the remaining 38 seconds, 9.5 nm of Al_2O_3 is etched away, as indicated by etch rates in Table 3.4. Despite this, a sufficient Al_2O_3 mask should remain for etching 2.716 µm of SiO_2, and SEM images confirmed appropriate x-y patterning of the Al_2O_3 layer.

Nevertheless, the pores were not accurately transferred into the SiO_2 layer, as observed in SEM images. For longer etching times of sample s3 compared to s4 (Table 3.5), the pore walls appeared to thicken while pore diameters decreased.

Additionally, the lowering of patterns relative to their surroundings indicates that the etching protocol did not meet the desired criteria. This outcome likely results from the faster removal of the Al_2O_3 mask on thinner pore walls compared to the broader surrounding patterns, explaining the observed height differences. Without sufficient masking, continuous SiO_2 etching may have caused further widening of the walls.

For the process in silicon, CHF_3/Ar RIE for 30 minutes followed by Bosch DRIE for 25 cycles proved effective for producing pores with a minimum depth of 1.5 µm and diameters as small as 150 nm. However, pore walls with thicknesses of 50 nm or less were partially broken at DRIE scallops, and those with thicknesses of 30 nm or less were completely broken. Consequently, the minimal achievable wall thickness was determined to be 40 nm. A difference in etch depth between different pore diameters was also not avoided. However, going deeper than the desired minimum of 1.5 µm is expected to be rather beneficial, but not limiting for cell experiments.

In Fig. 4.18D and E, increased wall break-through was observed near the pattern edge for a mask spacing (Δ_M) of 25 nm. This effect could be attributed to the development with AR 600-546, which left fewer residues and consequently produced thinner structures towards the edge. This observation may also explain why wall breakage at the pattern center for $\Delta_M = 25$ nm occurred only with the more precise development using Ethyl L-Lactate.

Finally, the HBr ICP etch produced pillars at the points between three pores. It is likely, that ICP process etched the thinner parts of the walls in between only two pores faster leading towards almost spike like structures with peaks at sites of highest wall thickness. Translating this effect to the ICP etches for the SiO_2 stack might explain the predicted fast ablation of Al_2O_3 at the thin walls.
Additionally, the HBr ICP etch resulted in the formation of pillar-like structures at points between three pores. It is likely that the ICP process etched the thinner sections of walls between only two pores more quickly, leading to spike-like structures where the wall thickness was greatest. This effect might also explain the rapid ablation of Al_2O_3 at thinner walls observed in the ICP etching of the SiO_2 stack.
In total, a protocol for etching at aspect ratios of almost 10:1 (pore depth/diameter) was established and silicon substrates of desired pore geometries produced. This successful fabrication of silicon substrates with controlled pore geometries can pave the way for future studies on the effects of pore size, distance, and density on T cell activation, providing valuable insights for biomedical applications.

4.2 Optimization of Substrate Plasma Coating

After successfully developing a production method for geometry defined nanopores in silicon, we looked at functionalizing substrate surfaces for ideal T cell activation. Therefore different plasma treatments were compared and the stability in vacuum tested.

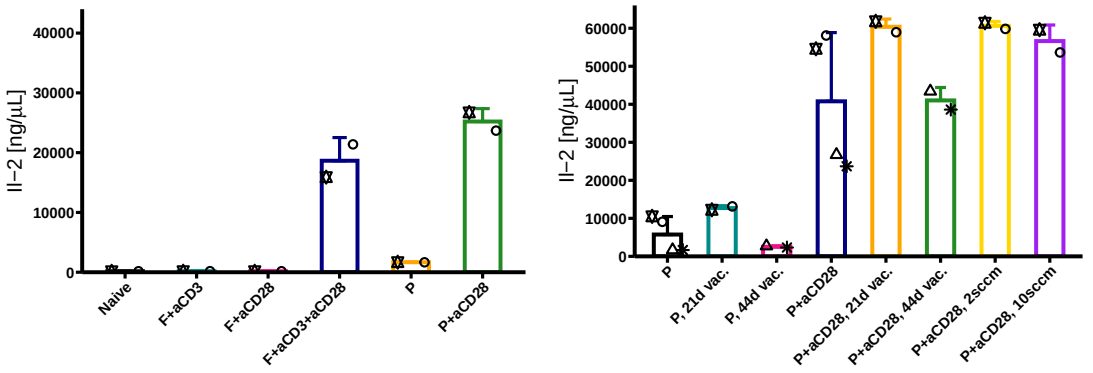

(a) Various coating conditions

(b) Porous conditions

Figure 4.26: IL-2 activation signal of primary pan T cells in ng µL^{-1} for different plasma treatment conditions. The bar shows the average value and the errorbar the standard deviation. Black symbols represent the individual measurements. Data for (a) is from Optimization 01 only, in (b) data of Optimization 01 and 02 is combined. Remark: P = Porous substrate, F = Flat substrate. One donor was used.

Readouts were done with fluorescence based plate readouts of IL-2. IL-2 is a cytokine secreted after T cell activation. AAO substrates were used for these experiments, as they were conducted in parallel to silicon pore process development.

4.2.1 IL-2 Secretion

Throughout this section, P and F are short for seeded on porous or flat substrates respectively. The air plasma of 2 sccm, 4 sccm and 10 sccm corresponded to pressures of 0.20 mbar, 0.25 mbar and 0.37 mbar respectively. Standard IL-2 curves in S21a and S21b were used for respective experimental runs, to determine IL-2 concentrations from fluorescence intensities.

With the conversions set, different conditions were compared. Naive (untreated) and Flat+aCD3+aCD28 treated conditions were used as controls, while different treatment conditions were mainly investigated for porous substrates. First, different coatings and then different plasma gas flows and plate vacuumation times were compared. Fig. 4.26a shows the IL-2 values obtained for various coating conditions with combinations of anti-CD3 (aCD3) and anti-CD28 (aCD28) on flat (F) and porous (P) substrates together with the negative control (naive). Data from two experiments (Optimization 01 and 02) is presented in this plot. The positive control of Flat+aCD3+aCD28 showed the expected activation behavior. However, treatment with P+aCD28 was resulting in even higher IL-2 levels.

In Fig. 4.26b, a comparison of IL-2 concentration for all 260 nm pores is shown. The values for P+aCD28 in Optimization 01 were however almost twice as high, as those in Optimization 02. The highest signals were achieved for samples vacuumed after plasma

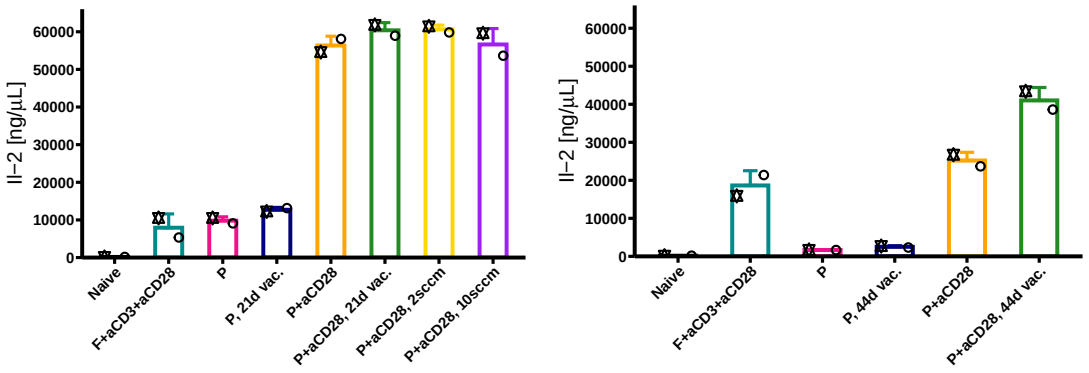

(a) Optimization 01 (b) Optimization 02

Figure 4.27: IL-2 activation signal of primary pan T cells in ng µL^{-1} for different plasma treatment conditions. The bar shows the average value and the errorbar the standard deviation. Black symbols represent the individual measurements. Remark: P = Porous substrate, F = Flat substrate. One donor was used.

treatment for 21 days and plasma at 2 sccm. Note, that due to the high variability in between experiments, this conclusion is not significant.
The two experiments showed quite different absolute IL-2 levels, making comparisons based on Fig. 4.26b, where combined data is presented hard. Therefore, Fig. 4.27a and Fig. 4.27b show the same conditions as Fig. 4.26b for Optimization 01 and Optimization 02 individually. Additionally, positive and negative controls are plotted. Different plasma treatments show comparable results and even enhanced activation after 44 day vacuumation.

Finally, different pore sizes were compared, where small corresponds to 130 nm and big to 350 nm pore diameter, while remaining conditions were treated on 260 nm pores. Fig. 4.28a shows IL-2 concentrations for different pore sizes in Optimization 02 and Fig. 4.28b shows plasma pressure data for Optimization 01.

4.2.2 Discussion

For the substrate optimization, the systematic errors are too big and the statistic too low, to make statements about statistical relevance of differences. However, some trends were found. Leaving the plates in vacuum after plasma treatment for 21 or 44 days did not reduce the activation effectiveness of the substrates, as one might expect due to possible air leakage. This enables time-wise independent substrate preparation and transportation. The activation of anti-CD28 coated substrates is the strongest, but the plasma pressure does not play a major role for the activation effectiveness. The activation on 130 nm (small) AAO pores was reduced compared to 260 nm and 350 nm (big) pores.

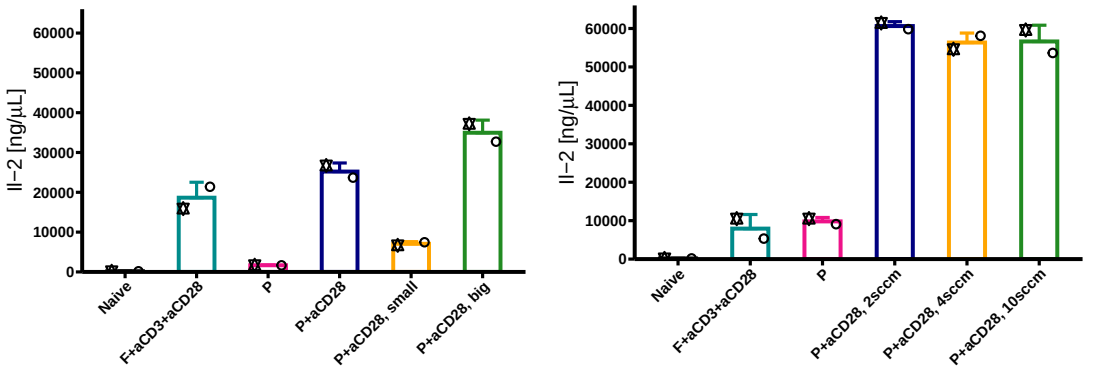

(a) Optimization 01 (b) Optimization 02

Figure 4.28: IL-2 activation signal of primary pan T cells in ng µL^{-1} for different plasma treatment conditions. The bar shows the average value and the errorbar the standard deviation. Black symbols represent the individual measurements. For (a) data is from Optimization 02 and for (b) from Optimization 01. Remark: P = Porous substrate, F = Flat substrate. One donor was used.

4.3 Calcium Signaling of Mechanically Activated T Cells

The role of calcium signaling in pore-induced activation of T cells was investigated. Therefore different protocols were compared and the one showing highest contrasts for activated cells compared to untreated cells selected for measurements of calcium levels for several donors. The results for protocol optimization are described first in the following subsection.

4.3.1 Establishment of Calcium Staining Flow Cytometry Protocol

The fluorescence background of unloaded T cells was minimal, approaching zero (Fig. S22), indicating a low level of autofluorescence. During protocol optimization, several key findings were noted:

1. **Loading Time:** The absolute fluorescence signal increased with loading time, but the rate of increase plateaued between 60 and 160 minutes (Fig. S23). Therefore, a loading time of 60 minutes was selected to achieve a high fluorescence signal while minimizing the loading duration.

2. **Buffer Conditions:** Using HBSS in both the loading and resting steps resulted in the highest fluorescence signal (Fig. S24). The MFI of the calcium stain, normalized to a naive population treated identically except for the substrate, was used as the signal.

3. **Calcium Indicators:** Both Fluo-4 and Fluo-8 calcium indicators produced similar fluorescence signals, although Fluo-8 showed a slightly higher intensity (Fig. S24a).

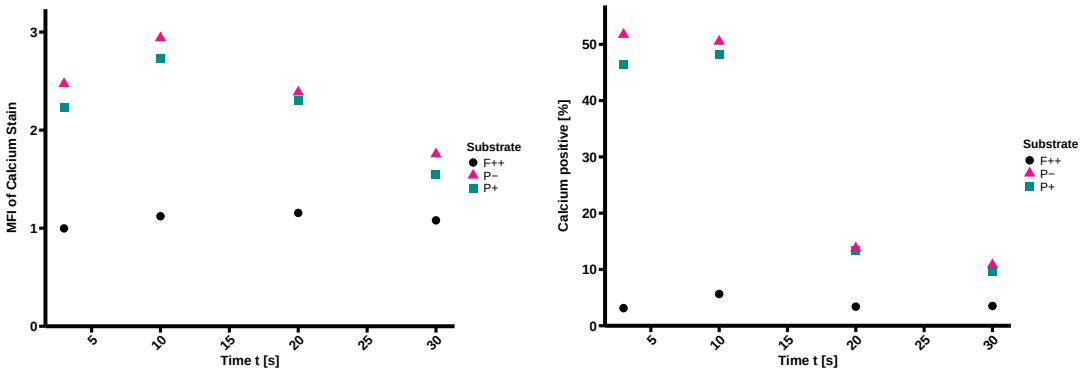

(a) MFI

(b) Percentage of Calcium+ cells

Figure 4.29: (a) Normalized MFI of calcium stain and (b) percentage of calcium positive gated cells for primary naive pan T cells over various activation times and for different substrate conditions. Remark: F++ = Flat+aCD3+aCD28 substrate. P- = Porous substrate, P+ = Porous+aCD28 substrate. One donor was used and mean values of duplicates are plotted.

4. **Temperature Effects:** Resting cells on ice had a minor impact on the activation signal, resulting in a slight reduction (Figs. S24a and S24b).

5. **Fixation Artifacts:** Fixation caused the lymphocyte population to split into two distinct populations with different calcium signals (Fig. S25).

6. **Cell Suspension Ratio:** The highest tested ratio of 2:1 cell suspension to buffer volume ratio provided the highest cell density, reducing the readout time per tube to as low as 30 seconds. This was beneficial, as both normalized and absolute MFI were found to decay measurably over 10 minutes.

7. **Washing Step:** Introducing a washing step with T cell medium for the pores increased the percentage of live-gated lymphocytes in the flow cytometry from 13.2% to 77.0% for naive cells treated with HBSS in both loading and resting step.

4.3.2 Pore-Induced Calcium Signal

First the effect of the activation time on calcium influx was analyzed. The comparison of activation times between two different types of data analysis (MFI and gating for calcium positive cells) revealed a peak in activation at 10 minutes (Fig. 4.29). However, for porous substrates, the two methods exhibited different maxima, with the calcium-positive population peaking after just 3 minutes of activation.

We next investigated calcium signals after 10 minutes of activation time under different treatment conditions. Fig. 4.30 presents calcium signals for different substrate conditions and coatings. For readouts based on calcium-positive cell populations, a discernible

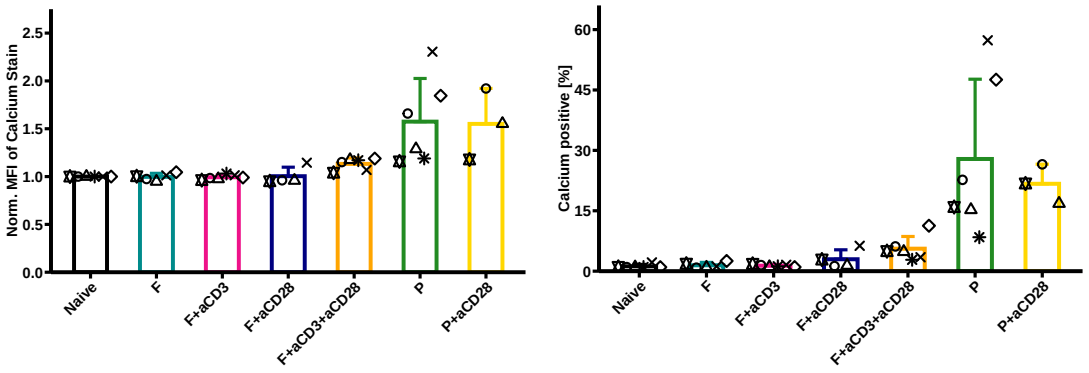

(a) MFI of calcium stain

(b) Percentage of calcium+ cells

Figure 4.30: (a) Normalized MFI of calcium stain and (b) percentage of calcium positive gated cells for primary naive pan T cells. Comparison of all coating conditions. The bar shows the average value and the errorbar the standard deviation. Black symbols represent the mean of individual experiments of duplicates. Remark: P = Porous substrate, F = Flat substrate. Four different donors were used.

calcium signal was observed for Flat+aCD3+aCD28 conditions, which was less apparent in normalized MFI values. Porous substrates produced a clear calcium signal, potentially stronger without anti-CD28.

We then compared the influx of calcium of the same experimental and substrate conditons as for Fig. 4.30 with a condition treated with a calcium ionophore. A calcium ionophore facilitates the transport of calcium ions (Ca^{2+}) across biological membranes, thereby increasing intracellular calcium levels. As expected, ionophore treatment induced high intracellular calcium levels (Fig. S26). We next treated the cells with GsMTx4 (Fig. 4.31). GsMTx4 is a peptide that selectively inhibits mechanosensitive ion channels, such as Piezo1, by blocking their response to mechanical stimuli, thereby reducing calcium influx into cells. Supringsingly, treatment of activated cells with GsMTx4 did not lead to a reduction in cellular calcium levels. Here, "activated" refers to conditions with calcium levels above those of naive cells. Other laboratory experiments using aliquots from the same batch of GsMTx4 indicated diminished functionality, suggesting potential degradation or defects in this lot. Unfortunately, a new batch of the compound arrived only after the results section of this thesis was completed.

To investigate whether calcium chelation affects pore-induced calcium influx, EDTA was added to the T cell culture during activation (Fig. 4.32). The results confirmed that EDTA effectively reduced cellular calcium levels when activated in particular on porous substrates.

In a next experiment we checked the influnce of Yoda1. Yoda1 is a chemical compound that specifically activates Piezo1 ion channels, leading to increased calcium influx into cells in response to mechanical stimuli. As expected, the treatment with Yoda1 increased the influx of calcium on all substrate conditions (Fig. 4.33). The observed

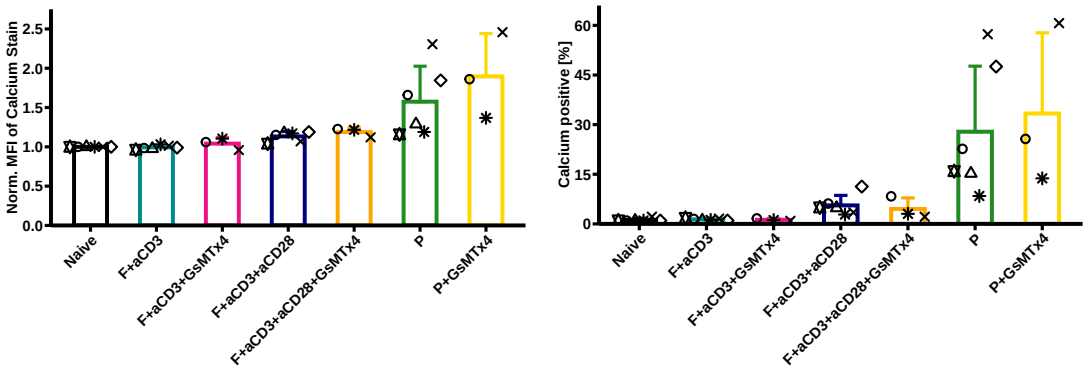

(a) MFI of calcium stain (b) Percentage of calcium+ cells

Figure 4.31: (a) Normalized MFI of calcium stain and (b) percentage of calcium positive gated cells for primary naive pan T cells. Comparison of conditions with and without GsMTx4. The bar shows the average value and the errorbar the standard deviation. Black symbols represent the mean of individual experiments of duplicates. Remark: P = Porous substrate, F = Flat substrate. Two different donors were used for data with GsMTx4 and four different donors were used in general.

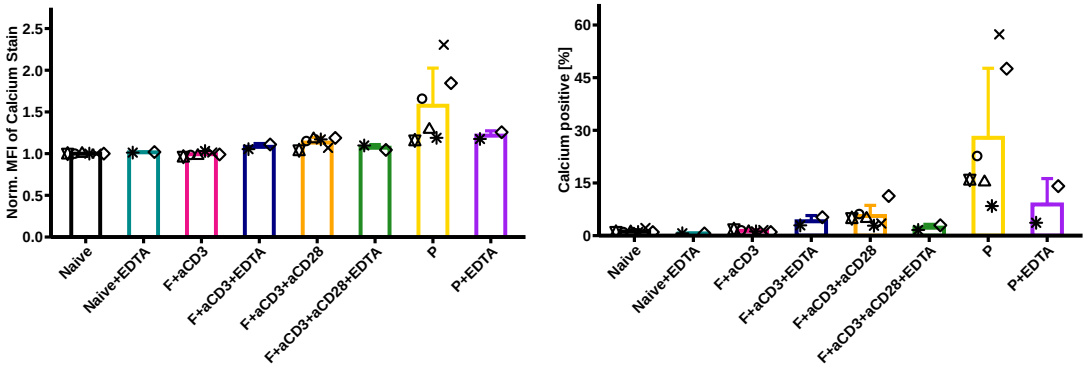

(a) MFI of calcium stain (b) Percentage of calcium+ cells

Figure 4.32: (a) Normalized MFI of calcium stain and (b) percentage of calcium positive gated cells for primary naive pan T cells. Comparison of conditions with and without EDTA. The bar shows the average value and the errorbar the standard deviation. Black symbols represent the mean of individual experiments of duplicates. Remark: P = Porous substrate, F = Flat substrate. Two different donors were used for data with EDTA and four different donors were used in general.

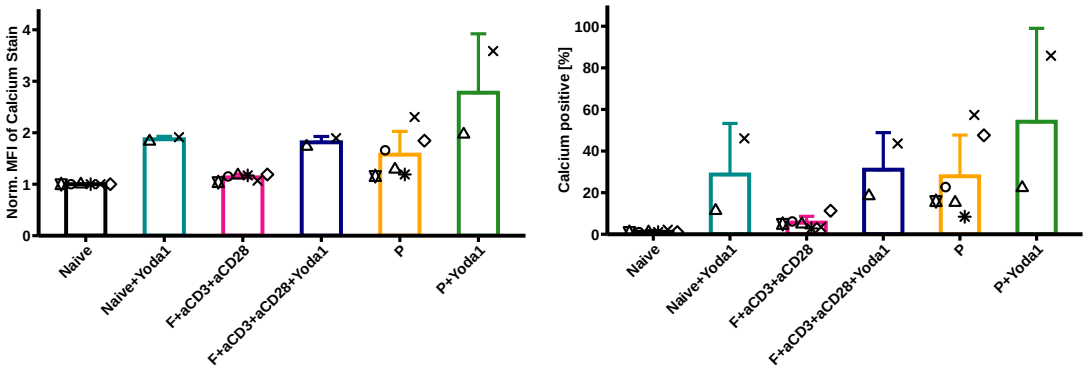

(a) MFI of calcium stain

(b) Percentage of calcium+ cells

Figure 4.33: (a) Normalized MFI of calcium stain and (b) percentage of calcium positive gated cells for primary naive pan T cells. Comparison of conditions with and without Yoda1. The bar shows the average value and the errorbar the standard deviation. Black symbols represent the mean of individual experiments of duplicates. Remark: P = Porous substrate, F = Flat substrate. Two different donors were used for data with Yoda1 and four different donors were used in general.

increase in calcium levels with Yoda1 treatment on porous substrates suggests that additional mechanisms beyond Piezo1 activation may further enhance pore-induced T cell activation.

4.3.3 Discussion

The successful implementation of calcium staining and flow cytometry readout for pan T cells demonstrated distinct calcium signals between negative controls (naive treatment) and positive controls (Ionophore treatment). The rapid onset of calcium influx, observed within just 10 minutes of cell seeding, underscores the effectiveness of this approach for detecting early calcium signaling events.

The relatively high calcium levels observed in cells seeded on porous substrates suggest a strong role for calcium signaling in T cell activation in these conditions. The reduction of calcium signals upon EDTA treatment supports the conclusion that the observed signal results from calcium influx during the experiment, as EDTA likely chelates available extracellular calcium before it can enter the cells through open calcium channels.

The lack of reduction in calcium levels in GsMTx4-treated conditions indicates that Piezo1 channels may not be the primary mediators of the observed calcium influx. If Piezo1 were responsible, its inhibition by GsMTx4 would have led to a decrease in calcium levels. However, this result might be due to a defective GsMTx4 variant,

potentially caused by expiration or other damage.

In contrast, the expected increase in calcium levels following Yoda1 treatment, which opens Piezo1 channels, was observed. The additional increase in calcium levels for cells on porous substrates treated with Yoda1 could suggest that not all Piezo1 channels are fully activated by Yoda1 alone. The difference between naive and porous substrate treatments in Yoda1-treated conditions further suggests that another calcium transport mechanism, beyond Piezo1 activation, may contribute to the calcium influx in cells on porous substrates, assuming that Yoda1 concentration is not a limiting factor.

Overall, these findings highlight the complex interplay of calcium signaling pathways in mechanically activated T cells and underscore the potential importance of substrate geometry in modulating T cell activation. Future studies should further elucidate the roles of different ion channels and signaling pathways in this context.

5 Conclusion

The results of this thesis successfully provided a foundation for detailed analysis of pore-induced T cell activation. Several pore production protocols were compared and one successful candidate was selected for production of pore arrays for T cell seeding. The respective protocol consists of patterning 288 nm thick CSAR positive EB resist at a dosage of 280 µC/cm^2. Thereafter, structures are transferred into a 300 nm thick SiO_2 layer with CHF_3/Ar RIE. The final structures are produced with a 25 cycle DRIE Bosch process. With this process, pore distances as small as 40 nm have been achieved as critical dimension for resolution. For 150 nm small pores, an approximate etch depth of 1.5 µm was reached. Given the small pore size and the therefore small gas exchange volume, this corresponds to an aspect ratio of as high as 10:1.

In the second aim, we showed, that vacuumation of plasma treated substrates keeps substrate functionalization in tact. This enables easier handling of pre-treated substrates.

Finally, a calcium readout with flow cytometry was established using HBSS buffer for cell suspensions in loading (60 minutes) and resting (30 minutes steps). This readout was successfully applied to mechanically activated T cells, revealing highest calcium levels around 10 minutes after activation. Calcium signaling was found to play an important role in pore-induced T cell activation. Findings after treatment with Piezo1 agonist Yoda1 indicated that other calcium transport mechanisms beyond Piezo1 could be involved in mechanic T cell activation.

Based on these findings, further steps can be taken. Cell experiments on precisely defined porous nanostructures reamain to be conducted and can potentially reveal critical connections to pore geometries. Further investigation of available calcium transport mechanisms and signaling pathways based on the developed readout method can elucidate the cellular mechanisms for TCR agonist independent T cell activation in future experiments.

Contributions

Sira Bielefeldt contributed to this thesis by carrying out development and etch steps for the fist three samples (v1-v3, Table 3.5) and aiding in the etching of sample v4 (Table 3.5), before my own approval to use the BRNC clean room. Ute Drechsler carried out the DRIE etch steps in my presence and provided ready-deposited wafers. The BRNC staff and mainly Antonis Olziersky executed EB exposures for resist patterning described in this thesis. Tamara Zünd aided me in carrying out the first run of the final calcium readout, where different experimental runs did overlap.

Acknowledgments

First and foremost, I want to express my gratitude to my advisors Tamara Zünd, Sebastian Lickert, Sira Bielefeldt and Viola Vogel.
Tamara Zünd was always available for questions and supported my work a lot, particularly in connection with cell culture and immune biology. Sebastian Lickert was my first contact to the lab and introduced me to the environment and all other advisors. He was always open to help, even after leaving ETH and provided valuable support in writing this report. Both Tamara and Sebastian also actively supported my personal career development over the duration of this thesis.
Sira Bielefeldt shared her valuable experience on microstructuring with me and initially accompanied and aided me in the foreign clean room environment. She also supported me until the end with valuable feedback and advice.
I would like to thank Viola Vogel for enabling this work by giving me the opportunity to work in her laboratory of Applied Mechanobiology. I also want to thank Enrico Klotzsch from Humboldt University Berlin for his advice and collaboration in this research. I am also glad for the advice on calcium staining by Willi Weber (HU Berlin).
I am very grateful to Ute Drechsler from BRNC, who has extensive knowledge about all sorts of clean room processes and readily shared that knowledge with me and aided me and everyone in the BRNC clean room. I also want to thank Antonis Olziersky, Michael Stiefel and all of the BRNC staff for their work and support of research like this.
Likewise, I would like to acknowledge the opportunities for easy access research I had at FIRST and ScopeM of ETH Zürich.
I also want to thank Rafael Saxer for helping me out with biology related questions from time to time.
Finally, I want to thank the entire Vogel lab for the nice lunch conversations and atmosphere and everyone who supported me in writing this report.

Bibliography

[1] Yoshihisa Kuwana, Yoshihiro Asakura, Naoko Utsunomiya, Mamoru Nakanishi, Yohji Arata, Seiga Itoh, Fumihiko Nagase, and Yoshikazu Kurosawa. Expression of chimeric receptor composed of immunoglobulin-derived v resions and t-cell receptor-derived c regions. *Biochemical and Biophysical Research Communications*, 149(3):960–968, 1987.

[2] Aroshi Mitra, Amrita Barua, Luping Huang, Siddhartha Ganguly, Qin Feng, and Bin He. From bench to bedside: the history and progress of CAR t cell therapy. *Frontiers in Immunology*, 14, 2023-05-15.

[3] Inmaculada Hernandez, Vinay Prasad, and Walid F. Gellad. Total costs of chimeric antigen receptor t-cell immunotherapy. *JAMA Oncology*, 4(7):994–996, 2018.

[4] Prakash Satwani, Karen Chao, Maria Lopez-Garcia, Matt Hall, Zhezhen Jin, Lena E Winestone, Danielle Novetsky Friedman, Rachel Phelan, Christina Baggott, Samuel John, Holly L. Pacenta, Theodore W. Laetsch, Christine L Phillips, Michael R Verneris, Vanessa A. Fabrizio, Amy Keating, Julie-An Talano, Amy Moskop, Susanne H.C. Baumeister, Muna Qayed, Doug Douglas Myers, Erin Marie Hall, Snehit Prabhu, Khanh Nguyen, Casey A Carr, Crystal L. Mackall, John K Lin, Jeremy Goldhaber-Fiebert, and Liora Michal Schultz. Establishing costs for commercial chimeric antigen receptor t-cell (tisagenlecleucel; kymriah) in children and young adult b-cell acute lymphoblastic leukemia; a merged analysis from the prwcc and PHIS. *Blood*, 142(Supplement 1):6912, 2023.

[5] David K. Y. Zhang, Alexander S. Cheung, and David J. Mooney. Activation and expansion of human t cells using artificial antigen-presenting cell scaffolds. *Nature Protocols*, 15(3):773–798, 2020.

[6] Michael C. Milone and Una O'Doherty. Clinical use of lentiviral vectors. *Leukemia*, 32(7):1529–1541, 2018.

[7] Hao Xu, Na Wang, Wenyue Cao, Liang Huang, Jianfeng Zhou, and Lingshuang Sheng. Influence of various medium environment to in vitro human t cell culture. *In Vitro Cellular & Developmental Biology - Animal*, 54(8):559–566, 2018.

[8] Hosein Rostamian, Keyvan Fallah-Mehrjardi, Mohammad Khakpoor-Koosheh, John M. Pawelek, Jamshid Hadjati, Christine E. Brown, and Hamid R. Mirzaei. A metabolic switch to memory CAR t cells: Implications for cancer treatment. *Cancer Letters*, 500:107–118, 2021.

[9] Sanjay Rathod. Chapter 4 - phenotyping of CAR t cells. In Sheila Spada and Lorenzo Galluzzi, editors, *Methods in Cell Biology*, volume 167 of *CAR T cells: development, characterization and applications*, pages 71–80. Academic Press, 2022.

[10] Morteza Aramesh, Diana Stoycheva, Lion Raaz, and Enrico Klotzsch. Engineering t-cell activation for immunotherapy by mechanical forces. *Current Opinion in Biomedical Engineering*, 10:134–141, 2019.

[11] Morteza Aramesh, Diana Stoycheva, Ioana Sandu, Stephan J. Ihle, Tamara Zünd, Jau-Ye Shiu, Csaba Forró, Mohammad Asghari, Margherita Bernero, Sebastian Lickert, Annette Oxenius, Viola Vogel, and Enrico Klotzsch. Nanoconfinement of microvilli alters gene expression and boosts t cell activation. *Proceedings of the National Academy of Sciences of the United States of America*, 118(40), 2021.

[12] Tamara Zünd, Sebastian Lickert, Anja Strebel, Marcia Murner, Tido Willms, Hasan Simsek, Weijie Du, Dimitrios Laurin Wagner, Viola Vogel, and Enrico Klotzsch. Nanoporous substrates to advance CAR-t cell production for advanced cell therapies. *Blood*, 142(Supplement 1):6787, 2023.

[13] Alaba Araoyinbo, Fazly Mohd, Srimala Sreekantan, and A Aziz. Voltage effect on electrochemical anodization of aluminum at ambient temperature. *International Journal of Mechanical and Materials Engineering*, 5, 2010.

[14] Shuiyuan Wang, Xiaoxian Liu, and Peng Zhou. The road for 2d semiconductors in the silicon age. *Advanced Materials*, 34(48):2106886, 2022.

[15] Rohit K. Ramakrishnan, Aravinth Balaji Ravichandran, Arpita Mishra, Archana Kaushalram, Gopalkrishna Hegde, Srinivas Talabattula, and Peter P. Rohde. Integrated photonic platforms for quantum technology: a review. *ISSS Journal of Micro and Smart Systems*, 12(2):83–104, 2023.

[16] Yuelong Yu, Xinjie Bai, Shaoyuan Li, Jianghao Shi, Lei Wang, Fengshuo Xi, Wenhui Ma, and Rong Deng. Review of silicon recovery in the photovoltaic industry. *Current Opinion in Green and Sustainable Chemistry*, 44:100870, 2023.

[17] S. R. Wenham and M. A. Green. Silicon solar cells. *Progress in Photovoltaics: Research and Applications*, 4(1):3–33, 1996.

[18] Nezih Pala and Mustafa Karabiyik. Electron beam lithography (EBL). In Bharat Bhushan, editor, *Encyclopedia of Nanotechnology*, pages 1033–1057. Springer Netherlands, 2016.

[19] B. P. Van Der Gaag and A. Scherer. Microfabrication below 10 nm. *Applied Physics Letters*, 56(5):481–483, 1990.

[20] M. Schirmer, Bastian Büttner, F. Syrowatka, G. Schmidt, T. Köpnick, and Christian Kaiser. Chemical semi-amplified positive e-beam resist CSAR 62 for highest resolution. *Proc SPIE*, 8886, 2013.

[21] Chen-Kuei Chung. Plasma etching. In Dongqing Li, editor, *Encyclopedia of Microfluidics and Nanofluidics*, pages 2766–2781. Springer, 2015.

[22] Franz Laermer, Sami Franssila, Lauri Sainiemi, and Kai Kolari. Deep reactive ion etching. In *Handbook of Silicon Based MEMS Materials and Technologies*, pages 417–446. Elsevier, 2020.

[23] Martin J. Walker. Comparison of bosch and cryogenic processes for patterning high-aspect-ratio features in silicon. In *MEMS Design, Fabrication, Characterization, and Packaging*, volume 4407, pages 89–99. SPIE, 2001.

[24] Pietro Ridone, Massimo Vassalli, and Boris Martinac. Piezo1 mechanosensitive channels: what are they and why are they important. *Biophysical Reviews*, 11(5):795–805, 2019.

[25] Chinky Shiu Chen Liu, Deblina Raychaudhuri, Barnali Paul, Yogaditya Chakrabarty, Amrit Raj Ghosh, Oindrila Rahaman, Arindam Talukdar, and Dipyaman Ganguly. Cutting edge: Piezo1 mechanosensors optimize human t cell activation. *The Journal of Immunology*, 200(4):1255–1260, 2018.

[26] Jason Wu, Amanda H. Lewis, and Jörg Grandl. Touch, tension, and transduction - the function and regulation of piezo ion channels. *Trends in Biochemical Sciences*, 42(1):57–71, 2017.

[27] Mohamed Trebak and Jean-Pierre Kinet. Calcium signalling in t cells. *Nature Reviews Immunology*, 19(3):154–169, 2019. Publisher: Nature Publishing Group.

[28] Alexander Babich and Janis K. Burkhardt. Coordinate control of cytoskeletal remodeling and calcium mobilization during t-cell activation. *Immunological Reviews*, 256(1):80–94, 2013.

[29] Kinjal Shah, Amr Al-Haidari, Jianmin Sun, and Julhash U. Kazi. T cell receptor (TCR) signaling in health and disease. *Signal Transduction and Targeted Therapy*, 6(1):412, 2021.

[30] Fernando Macian. NFAT proteins: key regulators of t-cell development and function. *Nature Reviews Immunology*, 5(6):472–484, 2005.

[31] Kenneth Murphy and Casey Weaver. *Janeway's Immunobiology*. Garland Science, New York, NY, 9th edition, 2016.

[32] Danay Cibrián and Francisco Sánchez-Madrid. CD69: from activation marker to metabolic gatekeeper. *European Journal of Immunology*, 47(6):946–953, 2017.

[33] Yijing Zhao, Chao Niu, and Jiuwei Cui. Gamma-delta ($\gamma\delta$) t cells: friend or foe in cancer development? *Journal of Translational Medicine*, 16(1):3, 2018.

[34] Sudhir Gupta, Makoto Shimizu, Kiyoshi Ohira, and Bharathi Vayuvegula. T cell activation via the t cell receptor: A comparison between wt31 (defining tcr)-induced and anti-cd3-induced activation of human t lymphocytes. *Cellular Immunology*, 132(1):26–44, 1991.

[35] Fan Xia, Cheng-Rui Qian, Zhou Xun, Yannick Hamon, Anne-Marie Sartre, Anthony Formisano, Sébastien Mailfert, Marie-Claire Phelipot, Cyrille Billaudeau, Sébastien Jaeger, Jacques A. Nunès, Xiao-Jun Guo, and Hai-Tao He. TCR and CD28 concomitant stimulation elicits a distinctive calcium response in naive t cells. *Frontiers in Immunology*, 9:2864, 2018.

[36] Youg Raj Thaker, Helga Schneider, and Christopher E. Rudd. TCR and CD28 activate the transcription factor NF-kappab in t-cells via distinct adaptor signaling complexes. *Immunology Letters*, 163(1):113–119, 2015.

[37] M. L. Schmitz and D. Krappmann. Controlling NF-kappaB activation in t cells by costimulatory receptors. *Cell Death and Differentiation*, 13(5):834–842, 2006.

[38] Zhitian Shi, Konstantins Jefimovs, Marco Stampanoni, and Lucia Romano. High aspect ratio arrays of si nano-pillars using displacement talbot lithography and gas-MacEtch. *Materials Science in Semiconductor Processing*, 157:107311, 2023.

[39] Hailiang Li, Tianchun Ye, Lina Shi, and Changqing Xie. Fabrication of ultra-high aspect ratio (>160:1) silicon nanostructures by using au metal assisted chemical etching. *Journal of Micromechanics and Microengineering*, 27(12):124002, 2017-12-01.

[40] Zhitian Shi, Konstantins Jefimovs, Lucia Romano, and Marco Stampanoni. Towards the fabrication of high-aspect-ratio silicon gratings by deep reactive ion etching. *Micromachines*, 11(9):864, 2020.

[41] Yemin Tang, Amin Sandoughsaz, and Khalil Najafi. Ultra high aspect-ratio and thick deep silicon etching (UDRIE). In *2017 IEEE 30th International Conference on Micro Electro Mechanical Systems (MEMS)*, pages 700–703, 2017.

[42] Michael S. Gerlt, Nino F. Läubli, Michel Manser, Bradley J. Nelson, and Jürg Dual. Reduced etch lag and high aspect ratios by deep reactive ion etching (drie). *Micromachines*, 12(5), 2021.

[43] Melissa J. Goodwin, Cornelis A. M. Harteveld, Meint J. de Boer, and Willem L. Vos. Deep reactive ion etching of cylindrical nanopores in silicon for photonic crystals. *Nanotechnology*, 34(22):225301, 2023.

[44] Leon Alexis Woldering. Fabrication of photonic crystals and nanocavities. 2008.

[45] C. C. Welch, A. L. Goodyear, T. Wahlbrink, M. C. Lemme, and T. Mollenhauer. Silicon etch process options for micro- and nanotechnology using inductively coupled plasmas. *Microelectronic Engineering*, 83(4):1170–1173, 2006.

[46] T. Trifonov, A. Rodríguez, F. Servera, L. F. Marsal, J. Pallarès, and R. Alcubilla. High-aspect-ratio silicon dioxide pillars. *Physica Status Solidi (a)*, 202(8):1634–1638, 2005.

[47] Tusar K. Acharya, Ankit Tiwari, Rakesh K. Majhi, and Chandan Goswami. TRPM8 channel augments t-cell activation and proliferation. *Cell Biology International*, 45(1):198–210, 2021.

[48] Marieke Meijer, Hester S. Hendriks, Harm J. Heusinkveld, Wendy T. Langeveld, and Remco H. S. Westerink. Comparison of plate reader-based methods with fluorescence microscopy for measurements of intracellular calcium levels for the assessment of *in vitro* neurotoxicity. *NeuroToxicology*, 45:31–37, 2014.

[49] Alice Vines, Gethin J. McBean, and Alfonso Blanco-Fernández. A flow-cytometric method for continuous measurement of intracellular Ca^{2+} concentration. *Cytometry Part A*, 77A(11):1091–1097, 2010.

Supplementary Figures and Tables

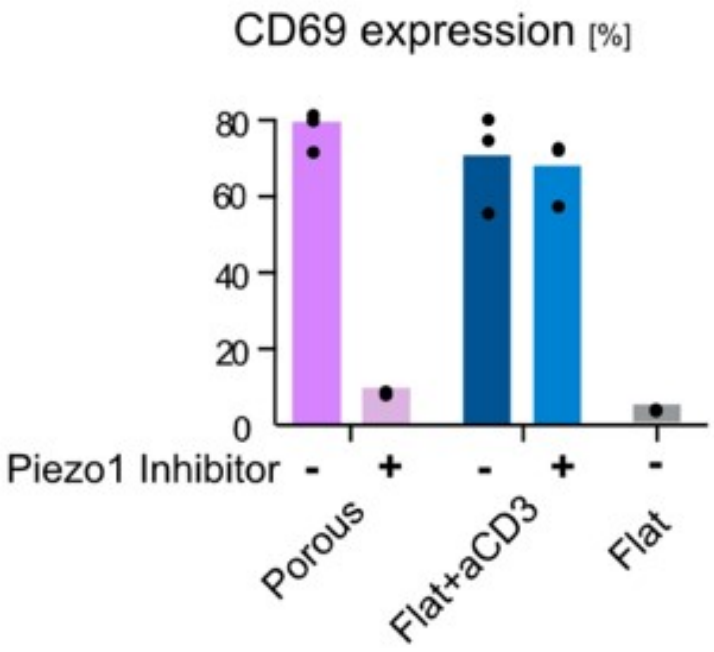

Figure S1: Amount of CD69 positive cells for different treatment conditions in percent of total cell number for respective condition. The flat surfaces are made of aluminium and aCD3 is short for anti-CD3. The figure is based on preliminary data by Tamara Zünd.

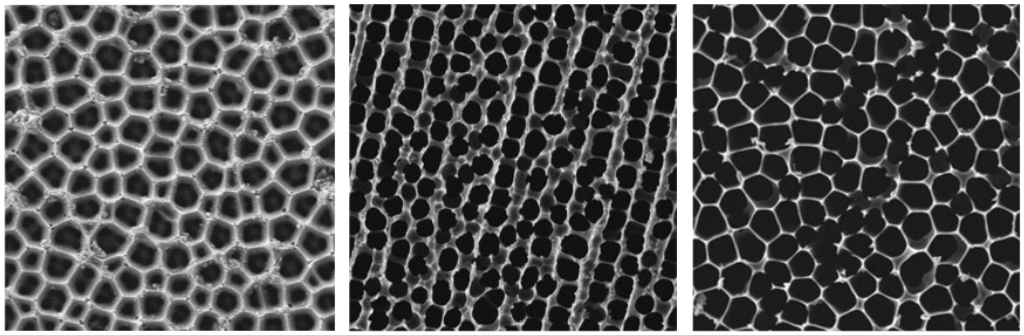

(a) 130 nm (b) 260 nm (c) 350 nm

Figure S2: SEM images of AAO surfaces with different pore sizes. The listed pore sizes are values provided by the manufacturer SmartMembranes.

Table S1: Pore diameters (PD) and minimal pore distances (MD) for $d_M = 150\,\text{nm}$ and $\Delta_M = 25\,\text{nm}$ and different EB dosages in sample s3 (Table 3.7) of CSAR resist after development. Differences from the ideal value $d_M - d$ and circularities of the pores are also listed. The values are obtained from SEM images in Figures Fig. 4.6 and 4.7 for different levels of contrast value proximity correction (CPC).

EB dosage D in $\mu C/cm^2$	CPC	Position in pattern	d in nm	MD Δ in nm	Difference $d_M - d$ in nm	Circularity C
280	80%	Center	138.5	36.5	11.5	0.89
280	80%	Edge	140.6	34.4	9.4	0.86
280	100%	Center	125.8	50.2	25.2	0.68
300	80%	Center	124.2	50.8	25.8	0.72

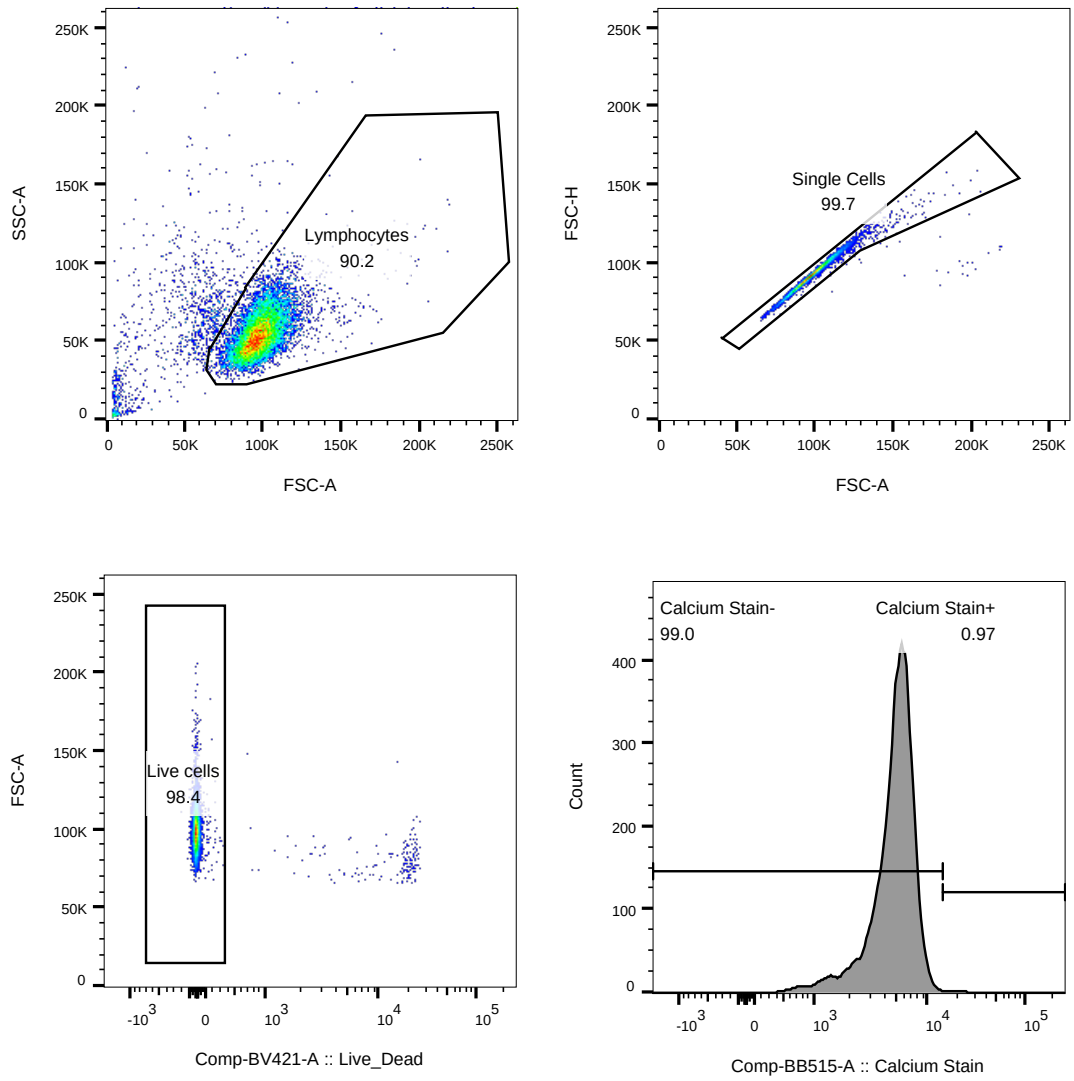

Figure S3: Calcium Staining gating into Lymphocytes (top left), thereof single cells (top right), thereof live cells (bottom left) and thereof Calcium positive or negative cells. Images generated with FlowJo for one exemplary donor at naive cell condition.

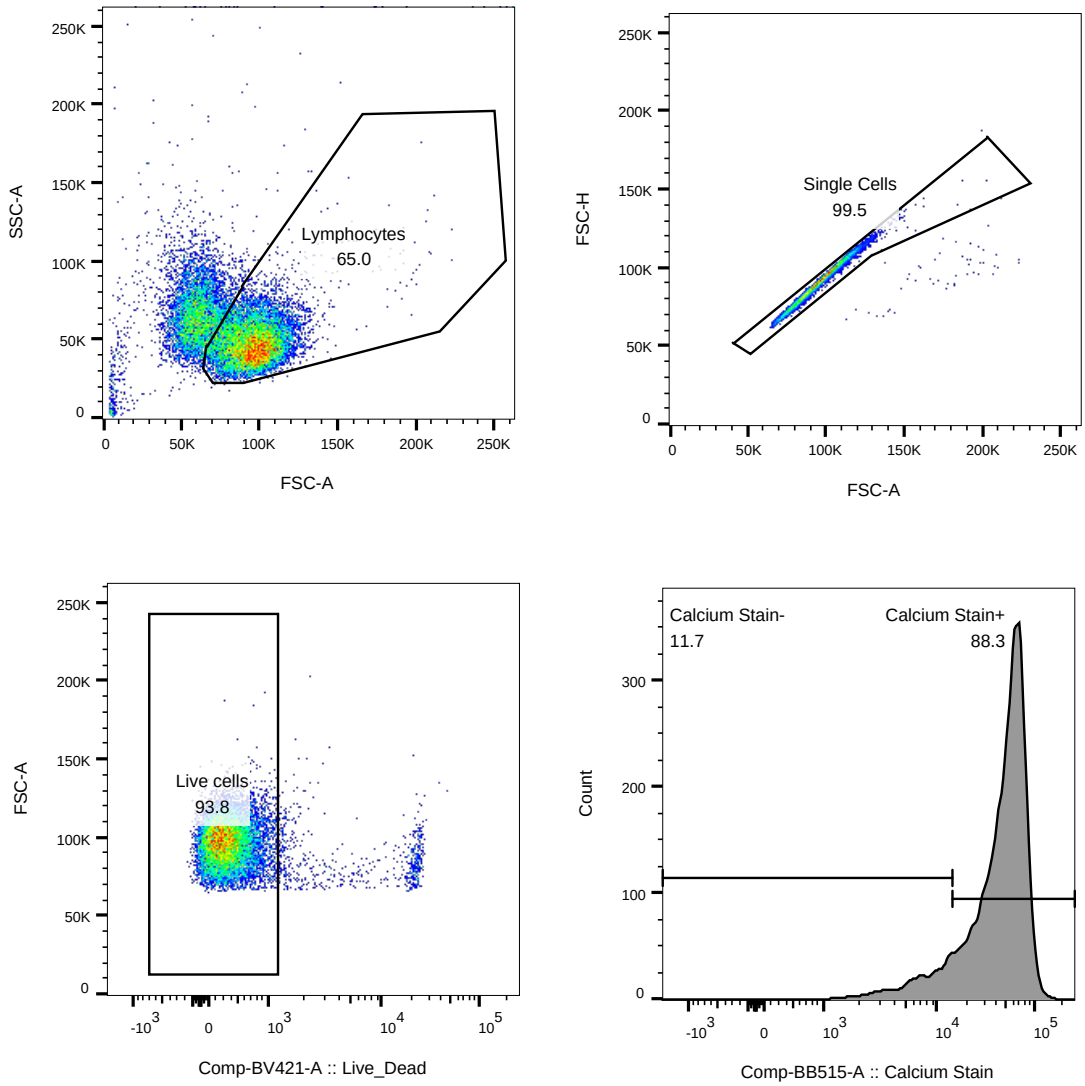

Figure S4: Calcium Staining gating into Lymphocytes (top left), thereof single cells (top right), thereof live cells (bottom left) and thereof Calcium positive or negative cells. Images generated with FlowJo for one exemplary donor at naive condition treated with Ionophore A23187.

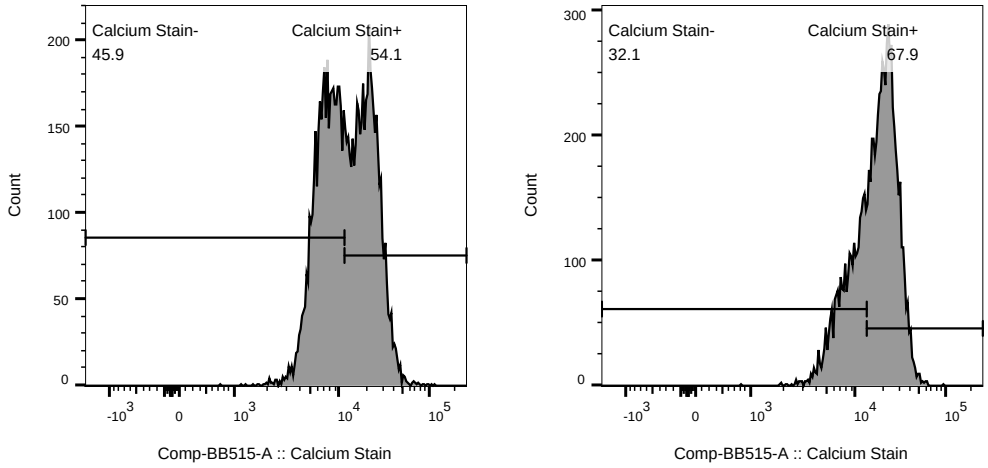

Figure S5: Calcium population distribution for two exemplary readouts and one donor. Images generated with FlowJo for T cells activated on Porous substrates.

Table S2: Height differences between EBL structured patterns of different pore specifications (lower) and surroundings (higher). Measurements are taken for sample v3 of Table 3.5 after BCl_3/Cl_2 and C_4F_8 etch and for samples with an EB dosage of $D = 230\,\mu C/cm^2$.

Mask PD d_M in nm	Mask MD Δ_M in nm	SiO_2 deposition method	Measurement height in nm
150	25	PECVD	535
150	25	thermal	715
150	100	PECVD	66
150	100	thermal	210
300	25	PECVD	339
300	25	thermal	506
300	100	PECVD	102
300	100	thermal	210
450	25	PECVD	270
450	25	thermal	396
450	50	PECVD	196
450	50	thermal	317
450	100	PECVD	90
450	100	thermal	180

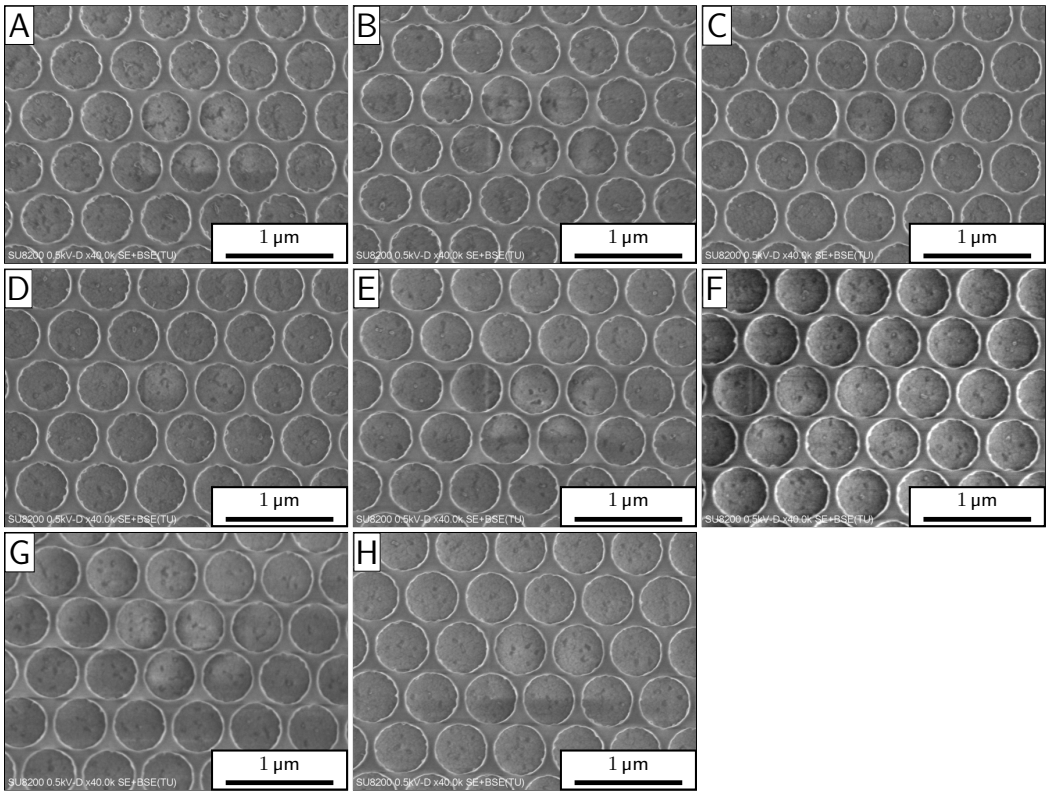

Figure S6: SEM images of CSAR resist on sample v3 (Table 3.5) after development with AR-600 546 for 3 min. All sub-figures show images of fields with minimal pore distance $\Delta_M = 100\,\mathrm{nm}$ and pore diameter $d_M = 450\,\mathrm{nm}$ according to the mask. Sub-figures show different EB dosages D. **A**: $D = 225\,\mu\mathrm{C/cm^2}$; **B**: $D = 230\,\mu\mathrm{C/cm^2}$; **C**: $D = 240\,\mu\mathrm{C/cm^2}$; **D**: $D = 245\,\mu\mathrm{C/cm^2}$; **E**: $D = 250\,\mu\mathrm{C/cm^2}$; **F**: $D = 255\,\mu\mathrm{C/cm^2}$; **G**: $D = 260\,\mu\mathrm{C/cm^2}$; **H**: $D = 265\,\mu\mathrm{C/cm^2}$

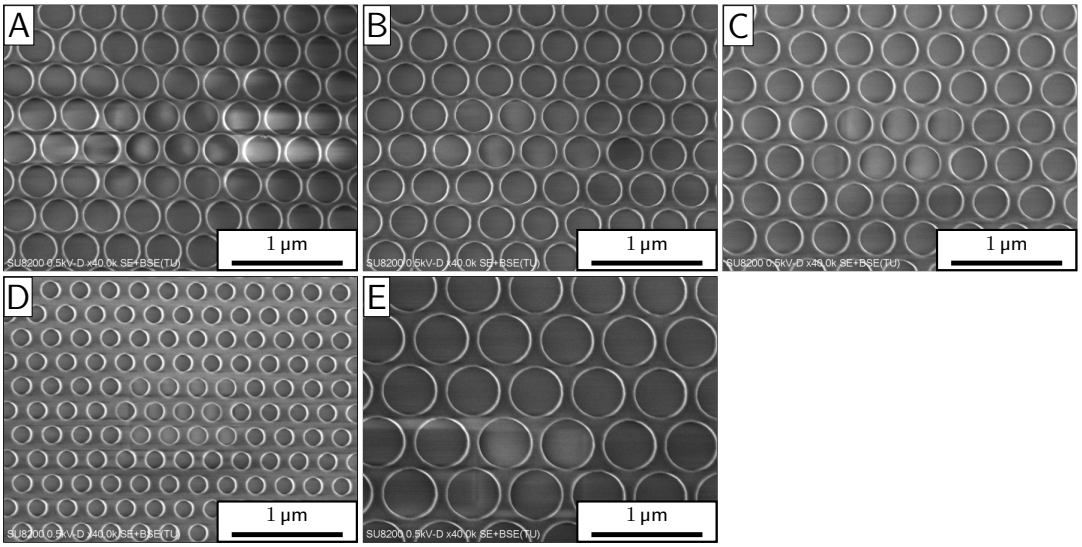

Figure S7: SEM images of CSAR resist on sample s4 (Table 3.7) after development with Ethyl L-lactate for 1 min. Sub-figures show images for different pore diameters d_M and minimal pore distances Δ_M as specified by the mask. **A**: $d_M = 300\,\text{nm}$, $\Delta_M = 70\,\text{nm}$; **B**: $d_M = 300\,\text{nm}$, $\Delta_M = 90\,\text{nm}$; **C**: $d_M = 450\,\text{nm}$, $\Delta_M = 25\,\text{nm}$; **D**: $d_M = 300\,\text{nm}$, $\Delta_M = 110\,\text{nm}$; **E**: $d_M = 150\,\text{nm}$, $\Delta_M = 110\,\text{nm}$; **F**: $d_M = 450\,\text{nm}$, $\Delta_M = 110\,\text{nm}$

Table S3: Pore diameters (PD) and minimal pore distances (MD) for different mask layouts in sample v4 (Table 3.5) for different deposition methods after BCl_3/Cl_2 and C_4F_8 etch. EB dosage for the patterning of the chips was $D = 230\,\mu\text{C/cm}^2$ for all table entries. Differences from the ideal value $d_M - d$ and circularities of the pores are also listed. The values are obtained from SEM images in Fig. 4.12.

Mask PD d_M in nm	Mask MD Δ_M in nm	SiO_2 deposition method	PD d in nm	MD Δ in nm	Difference $d_M - d$ in nm	Circularity C
150	100	PECVD	69.2	180.8	80.8	0.72
150	100	thermal	117.3	132.7	32.7	0.84
450	100	PECVD	299.3	250.7	150.7	0.84
450	100	thermal	334.8	215.2	115.2	0.90

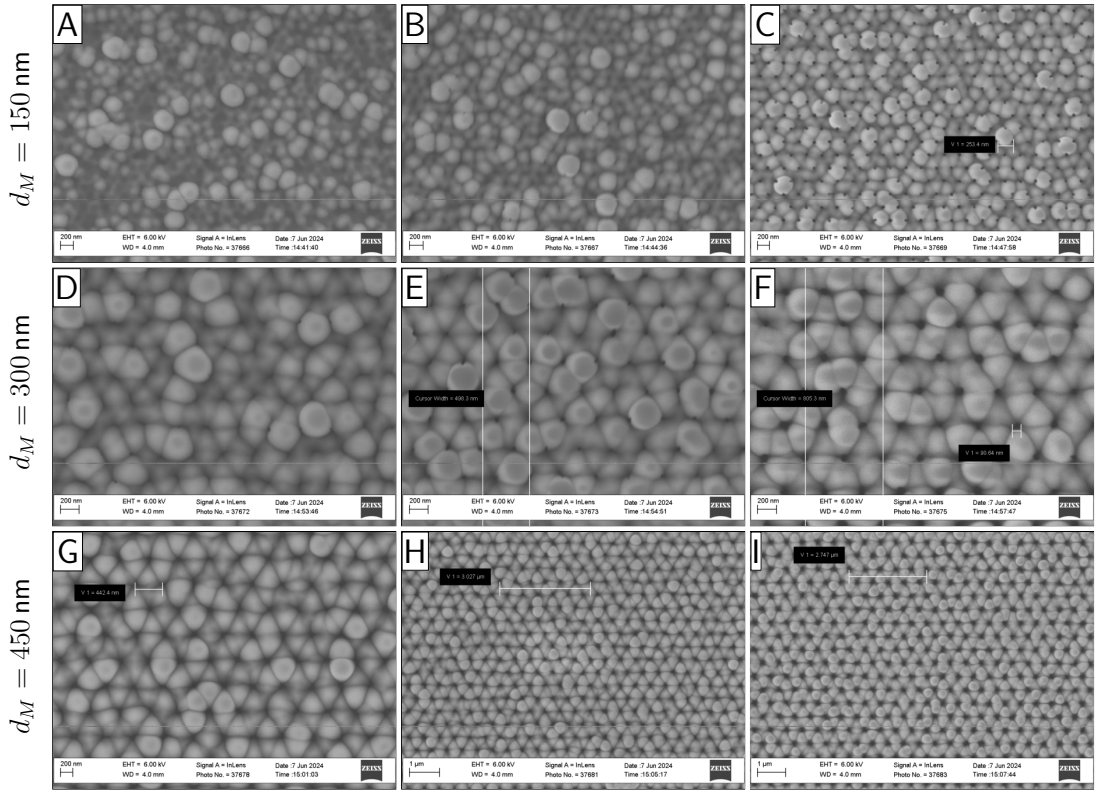

Figure S8: SEM images of sample v2 (Table 3.5) after BCl_3/Cl_2 and C_4F_8 etch. EB dosage used for resist patterning was $225\,\mu C/cm^2$. Images were taken at FIRST with Zeiss ULTRA 55 plus. Sub-figures show different mask specifications for pore diameters d_M and pore distances Δ_M. **A**: $d_M = 150\,\mathrm{nm}$, $\Delta_M = 25\,\mathrm{nm}$; **B**: $d_M = 150\,\mathrm{nm}$, $\Delta_M = 50\,\mathrm{nm}$; **C**: $d_M = 150\,\mathrm{nm}$, $\Delta_M = 100\,\mathrm{nm}$; **D**: $d_M = 300\,\mathrm{nm}$, $\Delta_M = 25\,\mathrm{nm}$; **E**: $d_M = 300\,\mathrm{nm}$, $\Delta_M = 50\,\mathrm{nm}$; **F**: $d_M = 300\,\mathrm{nm}$, $\Delta_M = 100\,\mathrm{nm}$; **G**: $d_M = 450\,\mathrm{nm}$, $\Delta_M = 25\,\mathrm{nm}$; **H**: $d_M = 450\,\mathrm{nm}$, $\Delta_M = 50\,\mathrm{nm}$; **I**: $d_M = 450\,\mathrm{nm}$, $\Delta_M = 100\,\mathrm{nm}$

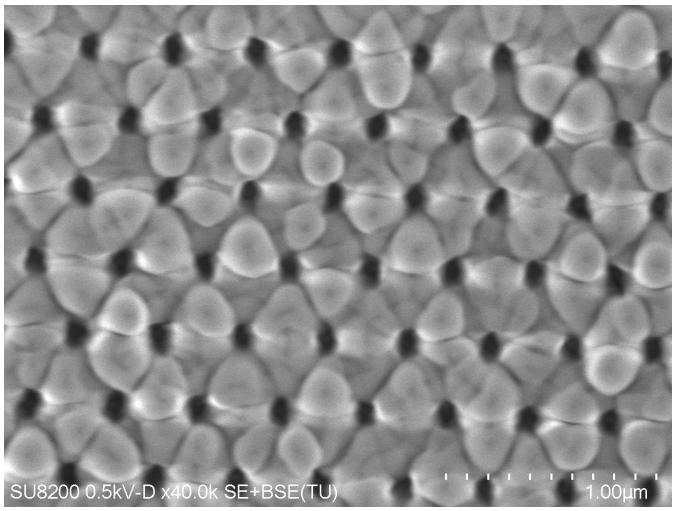

Figure S9: SEM image of sample v3 (Table 3.5) after BCl_3/Cl_2 and C_4F_8 etch. EB dosage used for resist patterning was $230\,\mu C/cm^2$. Pore diameter according to the mask is $d_M = 300\,nm$ and minimal pore distance $\Delta_M = 100\,nm$.

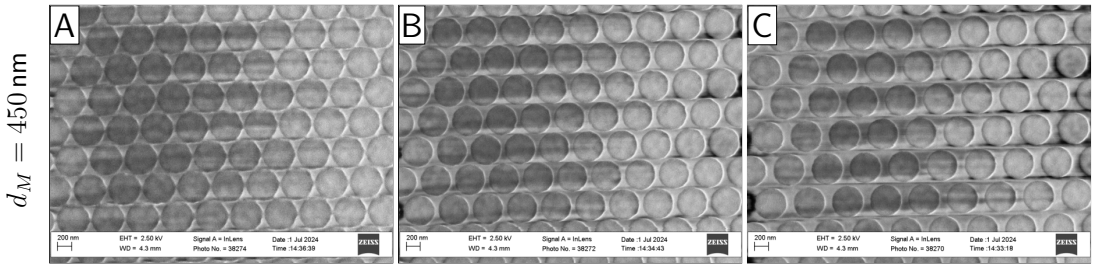

Figure S10: SEM images of sample v3 (Table 3.5) after BCl_3/Cl_2 etch. EB dosage used for resist patterning was $230\,\mu C/cm^2$. Images were taken at FIRST with Zeiss ULTRA 55 plus. All sub-figures show images of fields with pore diameter $d_M = 450\,nm$ according to the mask. Sub-figures show different mask specifications for pore distances Δ_M. **A**: $\Delta_M = 25\,nm$; **B**: $\Delta_M = 50\,nm$; **C**: $\Delta_M = 100\,nm$

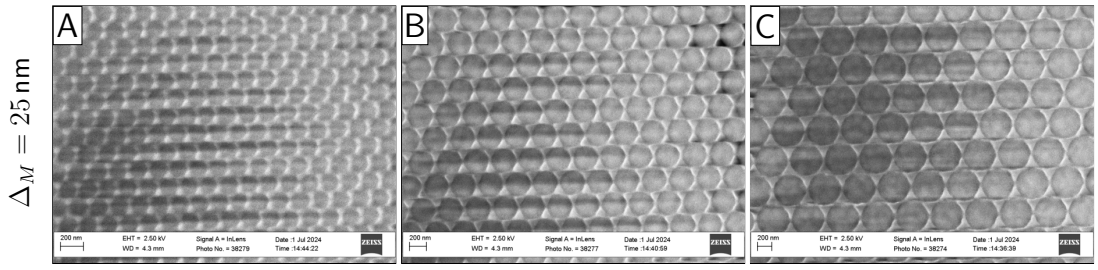

Figure S11: SEM images of sample v3 (Table 3.5) after BCl_3/Cl_2 etch. EB dosage used for resist patterning was $230\,\mu C/cm^2$. Images were taken at FIRST with Zeiss ULTRA 55 plus. All sub-figures show images of fields with minimal pore distance $\Delta_M = 25\,nm$ according to the mask. Sub-figures show different mask pore diameters d_M. **A**: $d_M = 150\,nm$; **B**: $d_M = 300\,nm$; **C**: $d_M = 450\,nm$

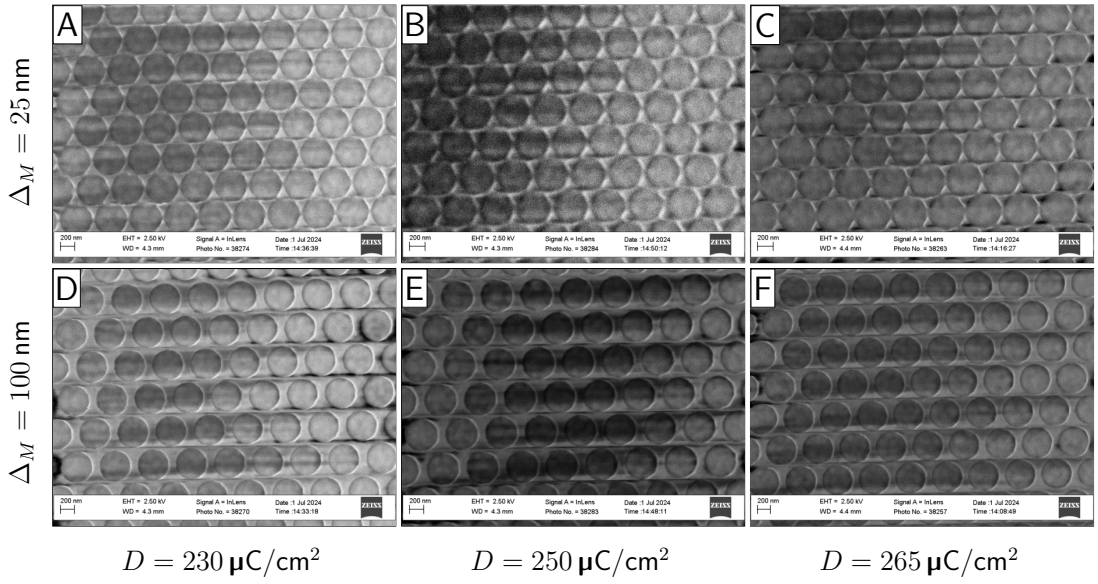

Figure S12: SEM images of sample v3 (Table 3.5) after BCl_3/Cl_2 etch. Images were taken at FIRST with Zeiss ULTRA 55 plus. All sub-figures show images of fields with minimal pore distance $\Delta_M = 25\,nm$ according to the mask. Sub-figures show different EB dosages D and mask pore diameters d_M. **A**: $d_M = 150\,nm$, $D = 230\,\mu C/cm^2$; **B**: $d_M = 150\,nm$, $D = 250\,\mu C/cm^2$; **C**: $d_M = 150\,nm$, $D = 265\,\mu C/cm^2$; **D**: $d_M = 450\,nm$, $D = 230\,\mu C/cm^2$; **E**: $d_M = 450\,nm$, $D = 250\,\mu C/cm^2$; **F**: $d_M = 450\,nm$, $D = 265\,\mu C/cm^2$

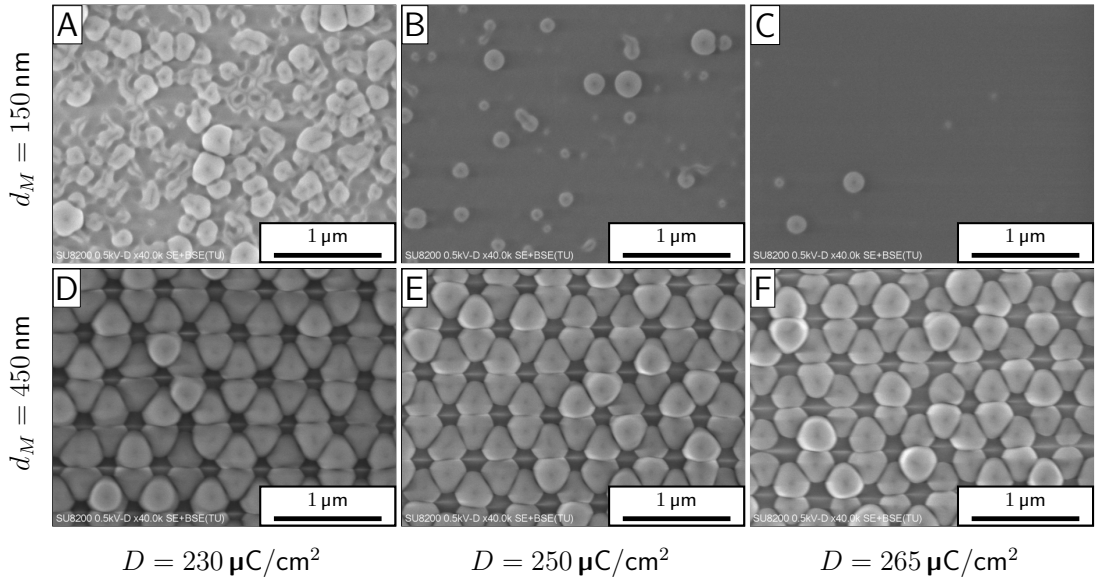

Figure S13: SEM images of sample v3 (Table 3.5) after BCl_3/Cl_2 and C_4F_8 etch. All sub-figures show images of fields with minimal pore distance $\Delta_M = 25\,\mathrm{nm}$ according to the mask. Sub-figures show different EB dosages D and mask pore diameters d_M. **A**: $d_M = 150\,\mathrm{nm}$, $D = 230\,\mu\mathrm{C/cm^2}$; **B**: $d_M = 150\,\mathrm{nm}$, $D = 250\,\mu\mathrm{C/cm^2}$; **C**: $d_M = 150\,\mathrm{nm}$, $D = 265\,\mu\mathrm{C/cm^2}$; **D**: $d_M = 450\,\mathrm{nm}$, $D = 230\,\mu\mathrm{C/cm^2}$; **E**: $d_M = 450\,\mathrm{nm}$, $D = 250\,\mu\mathrm{C/cm^2}$; **F**: $d_M = 450\,\mathrm{nm}$, $D = 265\,\mu\mathrm{C/cm^2}$

Table S4: Pore diameters (PD) and minimal pore distances (MD) for different mask layouts and EB dosages in sample s3 (Table 3.7) after RIE etch and 20 DRIE cycles. Differences from the ideal value $d_M - d$ and circularities of the pores are also listed. The values are obtained from SEM images in Fig. S17 for 80% contrast value proximity correction (CPC).

Mask PD d_M in nm	Mask MD Δ_M in nm	EB dosage D in $\mu\mathrm{C/cm^2}$	PD d in nm	MD Δ in nm	Difference $d_M - d$ in nm	Circularity C
150	50	280	134.0	66.0	16.0	0.90
150	50	300	139.8	60.2	10.2	0.89
150	50	320	139.2	60.8	10.8	0.89
300	50	280	263.4	86.6	36.6	0.87
300	50	300	269.6	80.4	30.4	0.85
300	50	320	269.2	80.8	30.8	0.86

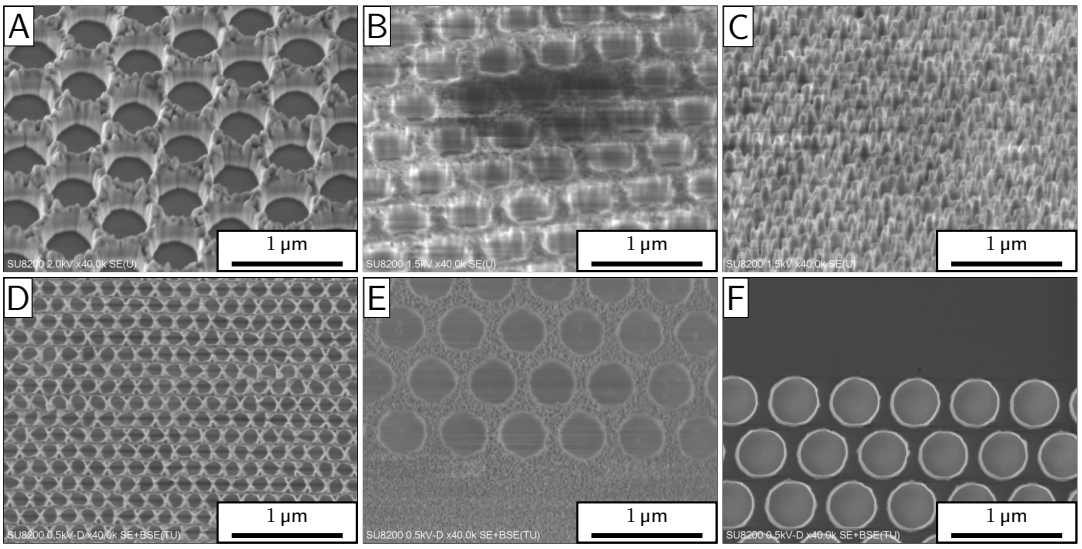

Figure S14: SEM images of sample s1 (Table 3.7) (A) and sample s2 (Table 3.7) (B-F) after RIE etch. Sub-figures show different mask specifications for pore diameters d_M and pore distances Δ_M for different tilt angles. **A**: $d_M = 450\,\text{nm}$, $\Delta_M = 100\,\text{nm}$, 45° tilt, 48.5 min etch time; **B**: $d_M = 450\,\text{nm}$, $\Delta_M = 100\,\text{nm}$, 45° tilt, 28 min etch time; **C**: $d_M = 150\,\text{nm}$, $\Delta_M = 25\,\text{nm}$, 45° tilt, 28 min etch time; **D**: $d_M = 150\,\text{nm}$, $\Delta_M = 25\,\text{nm}$, no tilt, 28 min etch time + CSAR removed; **E**: $d_M = 450\,\text{nm}$, $\Delta_M = 100\,\text{nm}$, no tilt, 15 min etch time, image taken at pattern edge; **F**: $d_M = 450\,\text{nm}$, $\Delta_M = 100\,\text{nm}$, no tilt, 28 min etch time + CSAR removed, image taken at pattern edge

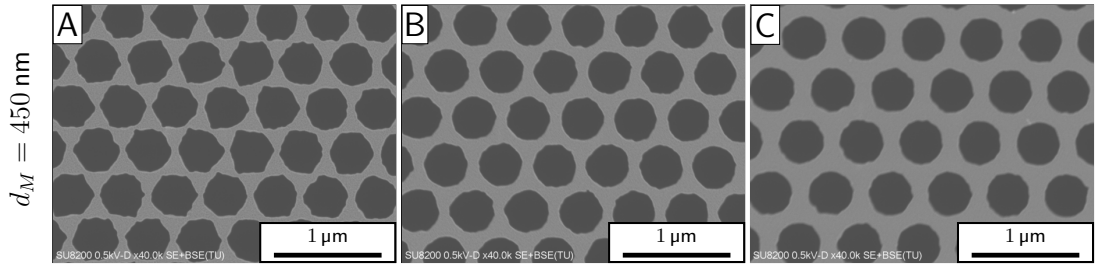

Figure S15: SEM images of sample s2 (Table 3.7) after RIE and DRIE. All sub-figures show images of fields with pore diameter $d_M = 450\,\text{nm}$ according to the mask. Sub-figures show different mask pore distances Δ_M. **A**: $\Delta_M = 25\,\text{nm}$; **B**: $\Delta_M = 50\,\text{nm}$; **C**: $\Delta_M = 100\,\text{nm}$

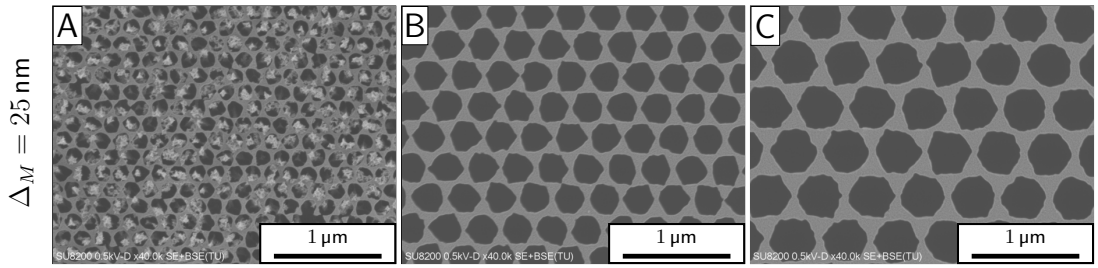

Figure S16: SEM images of sample s2 (Table 3.7) after RIE and DRIE. All sub-figures show images of fields with minimal pore distance $\Delta_M = 25\,\mathrm{nm}$ according to the mask. Sub-figures show different mask pore diameters d_M. **A**: $d_M = 150\,\mathrm{nm}$; **B**: $d_M = 300\,\mathrm{nm}$; **C**: $d_M = 450\,\mathrm{nm}$

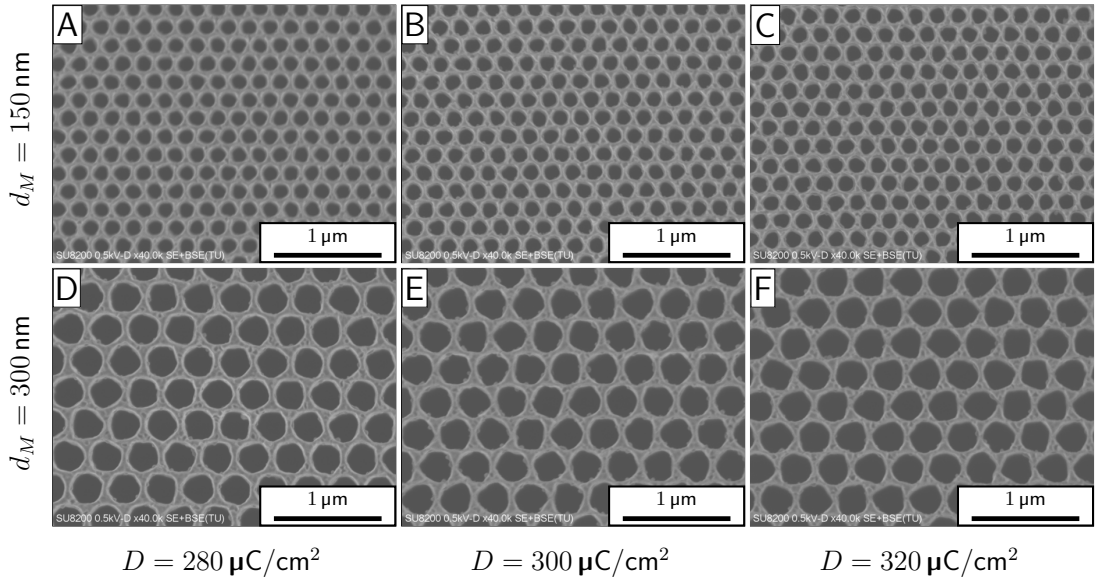

Figure S17: SEM images of sample s3 (Table 3.7) after RIE and DRIE. All sub-figures show images of fields with minimal pore distance $\Delta_M = 50\,\mathrm{nm}$ according to the mask. Contrast value proximity correction (CPC) level is 80%. Sub-figures show different EB dosages D and mask pore diameters d_M. **A**: $d_M = 150\,\mathrm{nm}$, $D = 280\,\mu\mathrm{C/cm^2}$; **B**: $d_M = 150\,\mathrm{nm}$, $D = 300\,\mu\mathrm{C/cm^2}$; **C**: $d_M = 150\,\mathrm{nm}$, $D = 320\,\mu\mathrm{C/cm^2}$; **D**: $d_M = 300\,\mathrm{nm}$, $D = 280\,\mu\mathrm{C/cm^2}$; **E**: $d_M = 300\,\mathrm{nm}$, $D = 300\,\mu\mathrm{C/cm^2}$; **F**: $d_M = 300\,\mathrm{nm}$, $D = 320\,\mu\mathrm{C/cm^2}$

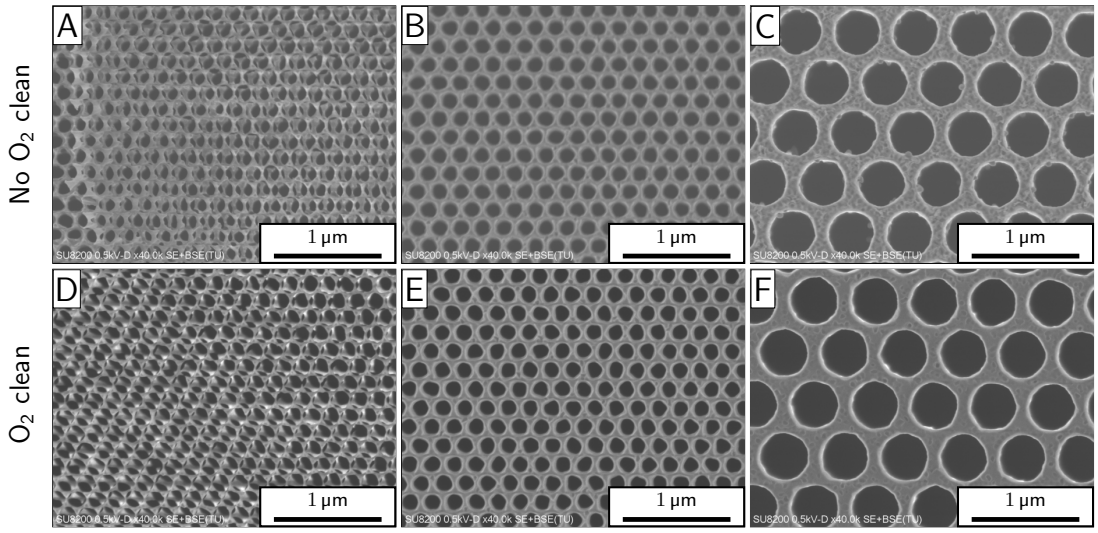

Figure S18: SEM images of sample s3 (Table 3.7) after RIE, DRIE and DMSO CSAR removal. The figures in the bottom row show the same patterns as above after an additional O_2 plasma cleaning step. EB dosage used for resist patterning was $280\,\mu C/cm^2$. Sub-figures show different mask specifications for pore diameters d_M and pore distances Δ_M. **A**: $d_M = 150\,\mathrm{nm}$, $\Delta_M = 25\,\mathrm{nm}$, no O_2 clean; **B**: $d_M = 150\,\mathrm{nm}$, $\Delta_M = 50\,\mathrm{nm}$, no O_2 clean; **C**: $d_M = 450\,\mathrm{nm}$, $\Delta_M = 100\,\mathrm{nm}$, no O_2 clean; **D**: $d_M = 150\,\mathrm{nm}$, $\Delta_M = 25\,\mathrm{nm}$, O_2 clean; **E**: $d_M = 150\,\mathrm{nm}$, $\Delta_M = 50\,\mathrm{nm}$, O_2 clean; **F**: $d_M = 450\,\mathrm{nm}$, $\Delta_M = 100\,\mathrm{nm}$, O_2 clean

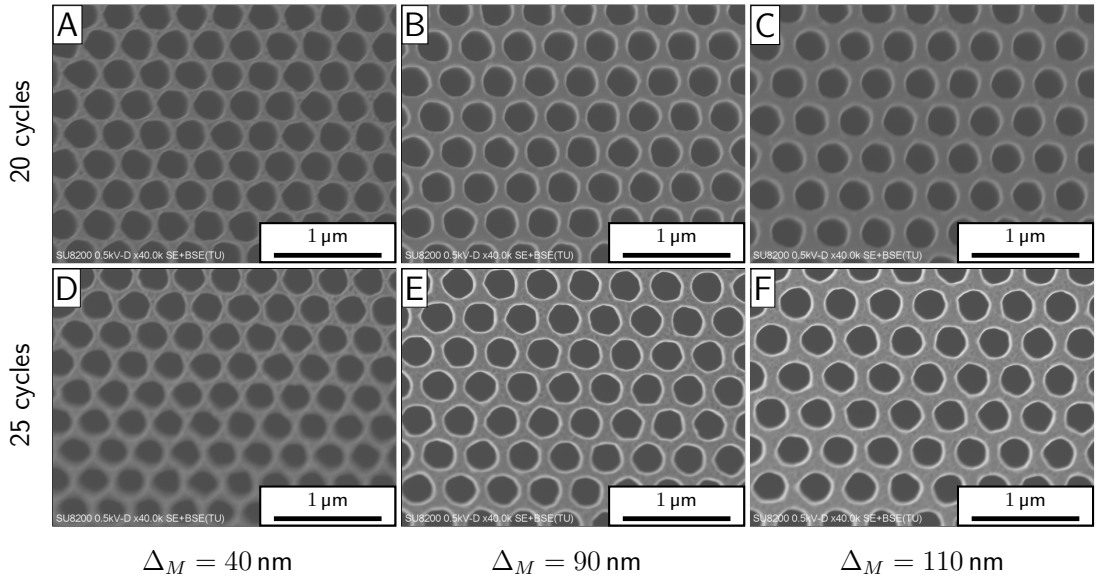

Figure S19: SEM images of sample s4 (Table 3.7) after RIE and 20 or 25 DRIE cycles in comparison. All sub-figures show images of fields with pore diameter $d_M = 300\,\mathrm{nm}$ according to the mask. Sub-figures show different mask specifications for minimal pore distances Δ_M. **A**: $\Delta_M = 40\,\mathrm{nm}$, 20 DRIE cycles; **B**: $\Delta_M = 90\,\mathrm{nm}$, 20 DRIE cycles; **C**: $\Delta_M = 110\,\mathrm{nm}$, 20 DRIE cycles; **D**: $\Delta_M = 40\,\mathrm{nm}$, 25 DRIE cycles; **E**: $\Delta_M = 90\,\mathrm{nm}$, 25 DRIE cycles; **F**: $\Delta_M = 110\,\mathrm{nm}$, 25 DRIE cycles

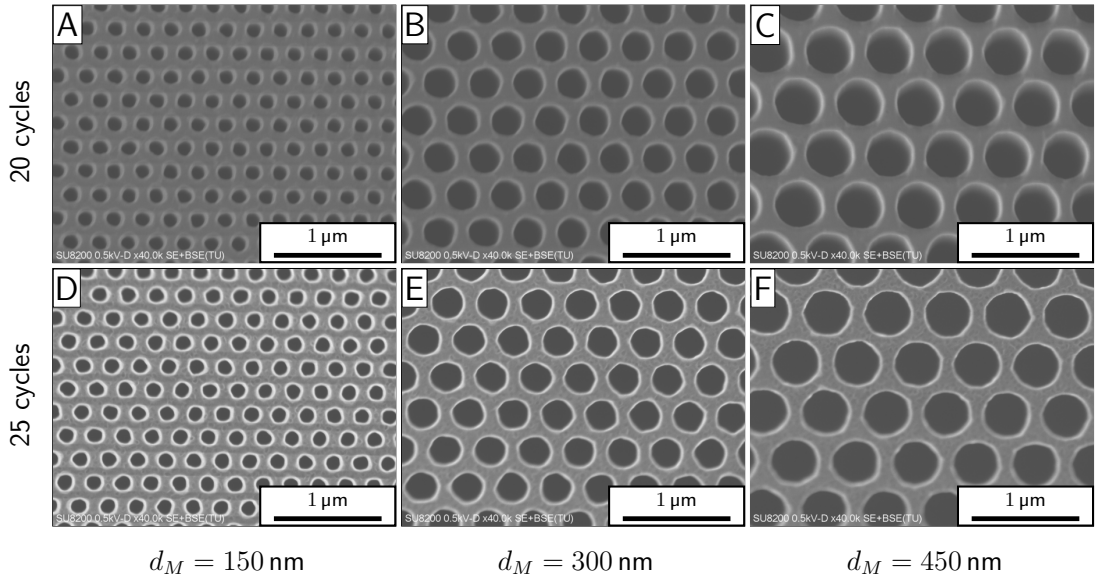

Figure S20: SEM images of sample s4 (Table 3.7) after RIE and 20 or 25 DRIE cycles in comparison. All sub-figures show images of fields with minimal pore distance $\Delta_M = 110\,\mathrm{nm}$ according to the mask. Sub-figures show different mask specifications for pore diameters d_M. **A**: $d_M = 150\,\mathrm{nm}$, 20 DRIE cycles; **B**: $d_M = 300\,\mathrm{nm}$, 20 DRIE cycles; **C**: $d_M = 450\,\mathrm{nm}$, 20 DRIE cycles; **D**: $d_M = 150\,\mathrm{nm}$, 25 DRIE cycles; **E**: $d_M = 300\,\mathrm{nm}$, 25 DRIE cycles; **F**: $d_M = 450\,\mathrm{nm}$, 25 DRIE cycles

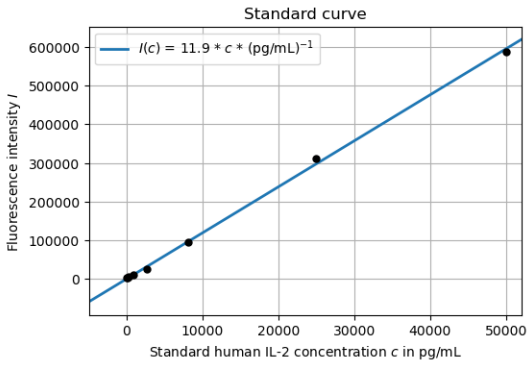

(a) Optimization 01, Fit 1

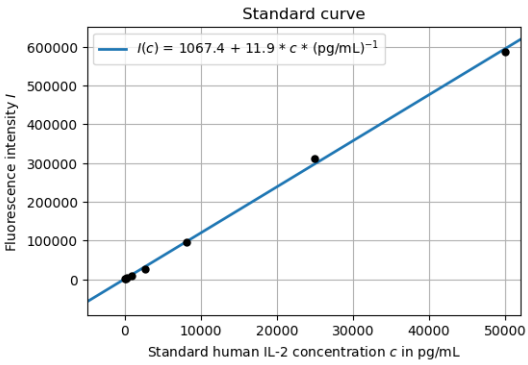

(b) Optimization 01, Fit 2

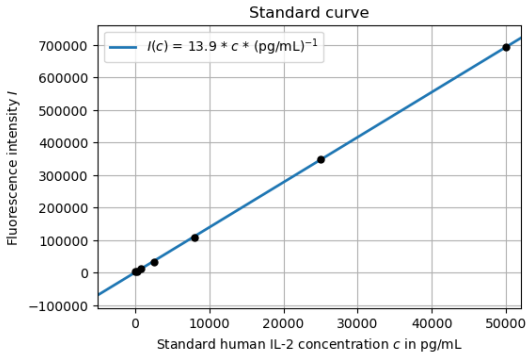

(c) Optimization 02, Fit 1

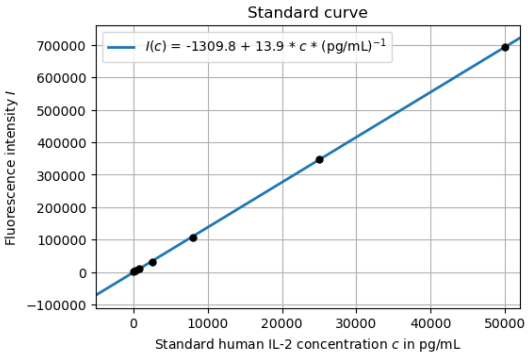

(d) Optimization 02, Fit 2

Figure S21: Fluorescence intensity I for standard human IL-2 at different concentrations c. For each of the two optimization experiments, fits for two different formulae are shown. Plots were generated with Python, Matplotlib.

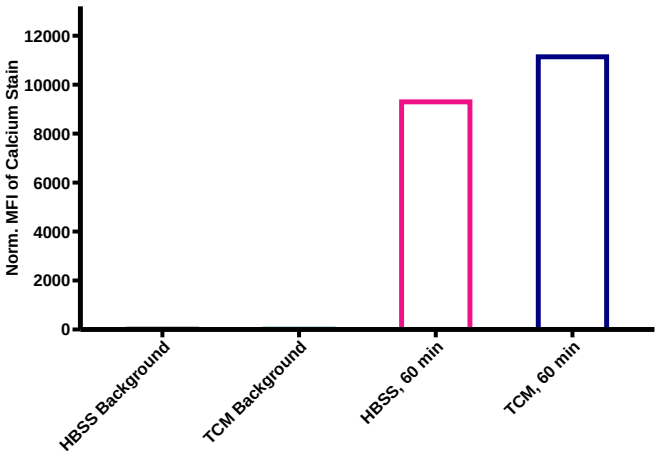

Figure S22: MFI of calcium stain (Fluo-4) for T cells measured immediately after loading for 60 min compared to the background without any loading. Remark: P = Porous substrate, F = Flat substrate. One donor was used.

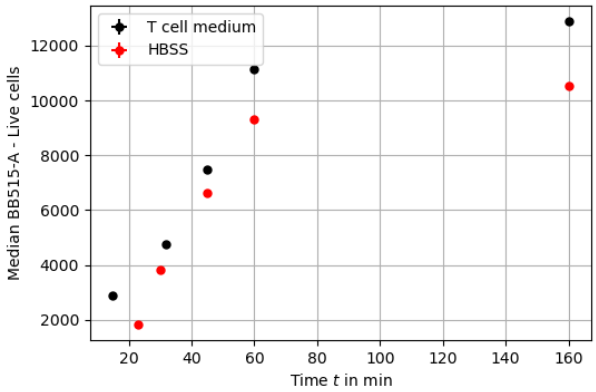

Figure S23: MFI of calcium stain (BB515-A) for T cells measured immediately after loading with Fluo-4 for time t in HBSS or TCM. The plot was generated with Python, Matplotlib. Remark: P = Porous substrate, F = Flat substrate. One donor was used.

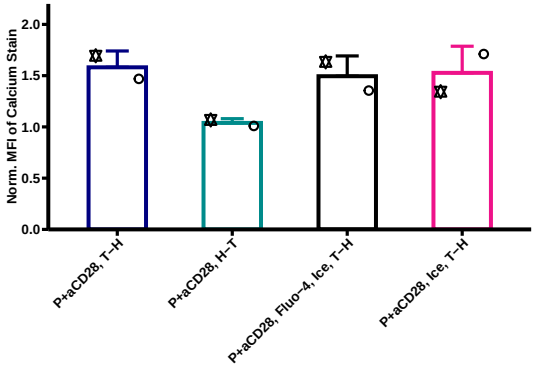

(a) Experiment 01

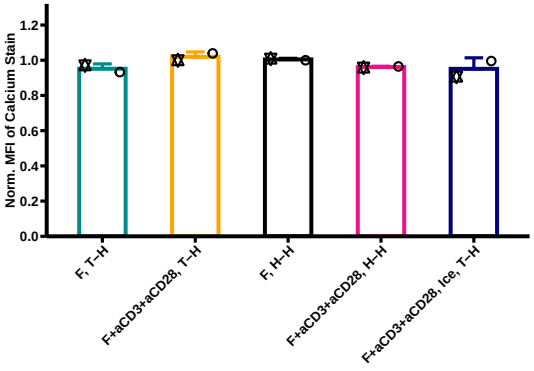

(b) Experiment 02

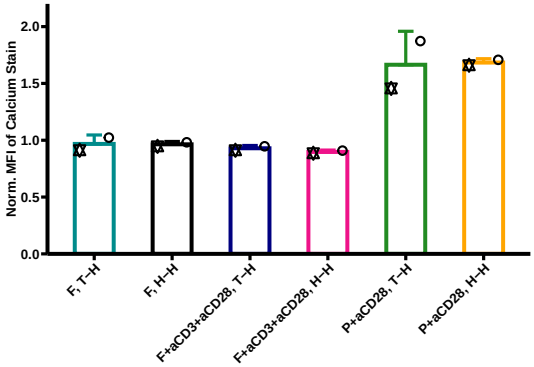

(c) Experiment 03

Figure S24: MFI of calcium stain for T cells. Whenever some parameter is not labeled explicitly, the default protocol was used. Comparison with cells suspended in a-b with a representing the loading step and b the resting step. HBSS (H) and TCM (T) were used. Remark: P = Porous substrate, F = Flat substrate. One donor was used per experiment.

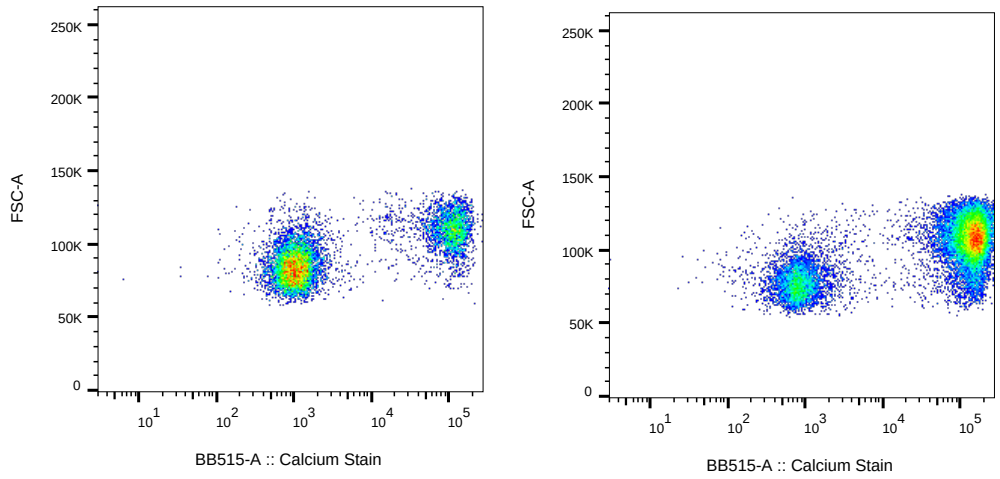

Figure S25: Lymphocyte population distribution over calcium stain for two exemplary readouts after fixation with ROTI® Histofix of one donor. Images generated with FlowJo for untreated T cells on the right and treated with Ionophore A23187 on the left.

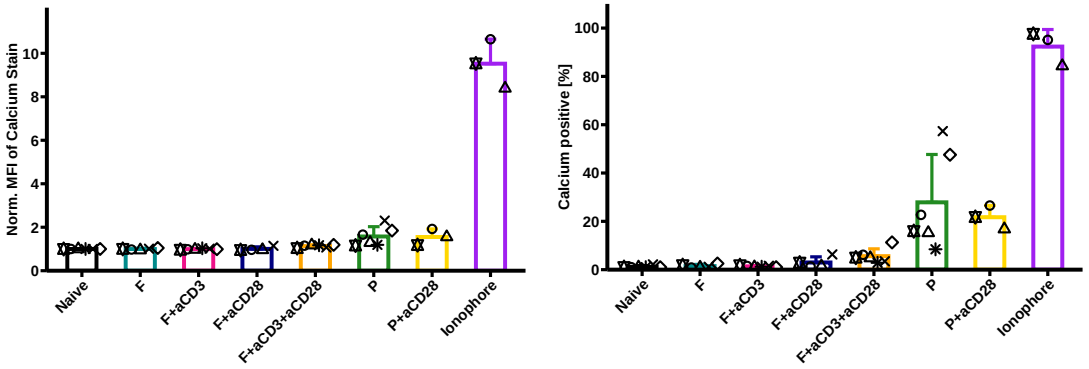

(a) MFI of calcium stain

(b) Percentage of calcium+ cells

Figure S26: (a) Normalized MFI of calcium stain and (b) percentage of calcium positive gated cells for primary naive pan T cells. Comparison of all coating conditions plus Ionophore. The bar shows the average value and the errorbar the standard deviation. Black symbols represent the mean of individual experiments of duplicates. Remark: P = Porous substrate, F = Flat substrate. Four different donors were used.

Eidgenössische Technische Hochschule Zürich
Swiss Federal Institute of Technology Zurich

Declaration of originality

The signed declaration of originality is a component of every written paper or thesis authored during the course of studies. In consultation with the supervisor, one of the following three options must be selected:

○ I confirm that I authored the work in question independently and in my own words, i.e. that no one helped me to author it. Suggestions from the supervisor regarding language and content are excepted. I used no generative artificial intelligence technologies[1].

◉ I confirm that I authored the work in question independently and in my own words, i.e. that no one helped me to author it. Suggestions from the supervisor regarding language and content are excepted. I used and cited generative artificial intelligence technologies[2].

○ I confirm that I authored the work in question independently and in my own words, i.e. that no one helped me to author it. Suggestions from the supervisor regarding language and content are excepted. I used generative artificial intelligence technologies[3]. In consultation with the supervisor, I did not cite them.

Title of paper or thesis:

Engineering nanoporous substrates to fine-tune T cell activation

Authored by:
If the work was compiled in a group, the names of all authors are required.

Last name(s):	**First name(s):**
Wenk	Marius

With my signature I confirm the following:
- I have adhered to the rules set out in the Citation Guide.
- I have documented all methods, data and processes truthfully and fully.
- I have mentioned all persons who were significant facilitators of the work.

I am aware that the work may be screened electronically for originality.

Place, date	**Signature(s)**
Zürich, 08.09.2024	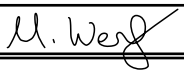

If the work was compiled in a group, the names of all authors are required. Through their signatures they vouch jointly for the entire content of the written work.

[1] E.g. ChatGPT, DALL E 2, Google Bard
[2] E.g. ChatGPT, DALL E 2, Google Bard
[3] E.g. ChatGPT, DALL E 2, Google Bard

Micro- and Nanosystems

Extension of the ETH Declaration of originality

The signed extension of the ETH declaration of originality is mandatory for every written thesis or semester project conducted at the Micro- and Nanosystems Group. All of the following aspects of good scientific practice must be confirmed by the student:

If I have used generative artificial intelligence technologies:

▣ I confirm that I have read any generated output carefully and checked it for accuracy and correctness using publicly available sources. I therefore understand that I am solely responsible for the correctness of my report.

▣ I confirm that I have read and understood each of the sources I cite.

▣ I confirm that I have not used any generated content in my report. If I have used AI-tools in writing, I have only done so to improve language and grammar.

▣ I have declared all use of AI-tools in the table below, including the name and version of the AI-tool, the use case and the scope.

AI-based Tool	Use case	Scope	Remarks
~~*e.g. ChatGPT4.0*~~	~~*Help in generating code for data visualization*~~	~~*Chapter 3, Fig. 12-18*~~	~~*Matlab*~~
ChatGPT 4.0	Help in generating code for data visualization	Fig. 4.26-4.33, S22,S24,S26	R
ChatGPT 4.0	Formating bibliography file (no content, only format), shortening figure titles, alphabetic sorting	Bibliography, Figure short titles, acronyms	Latex
ChatGPT 4.0	Language - Formulations	Abstract, Aims, 4.1.5, 4.3	Language

Research Data and Use Agreement

Prior to leaving the research group (student's name), Marius Wenk hands over all research data and/or materials (samples and products of any kind, collected or created during research work in tangible and intangible form) that have been acquired or collected within his / her activities at ETH Zurich, Micro and Nanosystems Group, to the thesis / project supervisor, namely Tamara Zünd. All relevant research data must be archived on the dedicated data server. I herewith confirm execution.

Title of thesis	
Engineering nanoporous substrates to fine-tune T cell activation	
Last name:	**First name:**
Wenk	Marius
Place, date	**Signature**
Zürich, 08.09.2024	M. Wenk

(voluntary agreement)

In addition, I also confirm that the above-mentioned data are allowed to be used by the members of the Micro and Nanosystems Group for further analysis and research. If these data become part of publications, the origin of the data will be acknowledged following the rules of good scientific conduct.

Signature Student	Signature Supervisor
M. Wenk	